DEPARTMENT OF PHYSICS AND ASTRONOMY
UNIVERSITY OF HEIDELBERG

Master Thesis in Physics
submitted by

HANNES RIECHERT

born in Oldenburg

2020

CONSTRUCTING U(1) GAUGE SYMMETRY IN ELECTRONIC CIRCUITS

This Master Thesis has been carried out by

HANNES RIECHERT

at the

KIRCHHOFF-INSTITUTE FOR PHYSICS

under the supervision of

JUN.-PROF. DR. FRED JENDRZEJEWSKI
Kirchhoff-Institute for Physics

ABSTRACT

Classical electronic circuits have proven powerful to study topological lattice structures. At the same time quantum simulators reach for increasingly complex lattice gauge theories with the goal of simulating processes in high energy physics. This work aims to connect these two fields by building a classical electronic circuit that approximates a U(1) gauge symmetric Hamiltonian. The circuit is constructed as an extention of the one-dimensional, topological Su-Schrieffer-Heeger model and we measure the time evolution in small system realizations with lattice sizes of up to three sites. The measurements qualitatively match theoretical expectations and agree with quantitative predictions where available. We develop a measure for the violation of local conserved quantities associated with gauge symmetry as benchmark for simulator quality. Since electronic circuits are fast in prototyping and of low cost, this platform provides a pathway to the classical regimes of non-abelian theories possibly faster than quantum simulators.

ZUSAMMENFASSUNG

Klassische elektronische Schaltkreise haben sich zur Untersuchung von topologischen Gitterstrukturen als nützlich erwiesen. Gleichzeitig werden in Quantensimulatoren immer komplexere Gittereichtheorien umgesetzt mit dem Ziel, Prozesse aus der Hochenergiephysik zu studieren. Diese Arbeit hat als Ziel diese beiden Forschungsbereiche durch die Entwicklung eines elektronischen Schaltkreises als klassischen Simulator, der eine U(1) Eichsymmetrie besitzt, zu verbinden. Der Schaltkreis ist eine Erweiterung des eindimensionalen Su-Schrieffer-Heeger-Modells, das topologische Eigenschaften aufweist. Wir messen die Zeitentwicklung in kleinen Ausführungen des Schaltkreises mit Gittergrößen von bis zu drei Gitterpunkten. Die Messungen passen qualitativ zu theoretischen Vorhersagen und stimmen mit einfach formulierbaren quantitativen Aussagen überein. Wir entwickeln ein experimentelles Maß für die Verletzung der lokalen Erhaltungsgrößen, die mit der Gittereichtheorie einhergehen, und als mögliches Qualitätsmerkmale für die Qualität der analogen Simulation dient. Da elektronische Schaltkreise sich schnell und mit geringen Kosten entwickeln lassen, bieten sie sich als Plattform für klassische Simulationen nicht abelscher Gruppen an.

CONTENTS

1

INTRODUCTION

There is a set of computational problems that are not efficiently solved on classical processors but on quantum architectures. They include—according to current knowledge—problems that are not natively quantum, for example prime factorization. Moreover, quantum machines can provide more insight into problems that are quantum in nature, for example Hubbard models [1]. Quantum simulators are specialized architectures for smaller subsets of these problems and are being implemented in various platforms, i. a. neutral / ultracold atoms, trapped ions, and superconducting circuits. On the way to simulations of phenomena from high energy physics, experiments implement increasingly complex lattice gauge theories [2]. Among them are proposals for lattice quantum electrodynamics, to be implemented in quantum simulators using ultracold atoms [3, 4]. As a first step, a building block for a U(1) gauge theory in ultracold atoms was experimentally realized [5]. Ultracold atoms experiments have already been used for $\mathbb{Z}_2$ lattice gauge theories [6, 7], while trapped ion experiments have progressed to realizations of the Schwinger model [8, 9].

Quantum electrodynamics is an abelian gauge theory, where 'abelian' refers to the commutativity of the group formed by the symmetry transformations. With the progress in simulators for abelian lattice gauge theories, the more complicated non-abelian theories come into reach, but current work remains on paper as the languages of high energy physics and the quantum simulation community are still converging [10].

Field theories from high energy physics are discretized onto lattices for classical simulations of these theories but also for quantum computations. In quantum simulators these lattices often correspond to actual lattice structures in the quantum hardware, e. g. ions or atom clouds. In the same vein will the lattice structure be reflected in the electronic circuit.

The ease of use and low cost of electronic circuits compared to quantum experiments motivate their use for faster testing of experimental protocols and theoretical ideas relating to lattice gauge theories. Classical electronic circuits have proven powerful to study several topological lattice structures [11, 12]. The careful arrangement of basic electronic components allows the construction of topological insulators and multidimensional metamaterials [13]. Since these electronic circuits are classical, they are not able to provide the computational advantage of quantum simulators. Due to the similar architecture, the circuit developed in this thesis lends itself in particular to adaption in superconducting circuits to regain the quantum features.

This thesis aims to connect current research in quantum simulation for lattice gauge theories with the methods developed for topological electronic circuits. As gauge theories are a concept of both classical and quantum mechanics, their impact and physical intuition—especially local conservation laws—are present in both quantum and classical setups, such that insights can be transferred between these worlds.

Verification of results becomes important, when quantum simulators become powerful enough that classical computations cannot follow up, which happens by definition at about the same point where the quantum advantage becomes useful. This is not true for every quantum computation, because for example prime factorization has a unique result that is easily checked. The outcome of quantum simulations, on the other hand, inevitably degrades due to experimental imperfections. For meaningful results, at least an estimation of the error is necessary. As local conservation laws are the hallmark feature of gauge theories, in this work we try to define a measure for the violation of local conserved quantities as a proxy for the quality of the simulator.

The structure of the thesis is as follows:

- Section 2 traces steps from Lee et al. [13] in the implementation of the Su-Schrieffer-Heeger model in electronic circuits and measuring topological properties. Considerations regarding topology are included only in so far, as to point out the significance of measurement results for this circuit.
- In section 3 the construction of a simple U(1) model by inserting a variant of minimal coupling is described. Methods developed for topological circuit are applied in order to find a differential equation describing a circuit that approximates this U(1) model. We explore its expected behavior in an exactly solvable special case and by numerical simulation of the full system.
- Section 4 discusses the implementation of the circuit and details concerning electronic components. Measurement results are presented and a quantitative measure for the violation of local conservation laws is developed.

The thesis closes in section 5, drawing final conclusions and presenting options for further research.

2

SU-SCHRIEFFER-HEEGER MODEL

The Su-Schrieffer-Heeger model (SSH model) [14] is the simplest system with topological properties and has been realized in both the quantum regime, e. g. by Atala et al. [15], and classical electronic circuits, see Lee et al. [13] or Kotwal et al. [16].

The Hamiltonian characteristic of the SSH model is formulated for a single electron in the tight-binding approximation. It is made up from unit cells of two sites with intra-cell hopping v and inter-cell hopping w as illustrated in figure 1. The Hamiltonian for a chain of N unit cells is written as

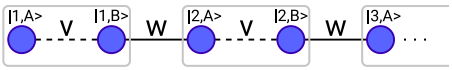

Figure 1: Structure of the SSH chain with localized states $|n, A/B\rangle$ and alternating coupling v, w. Every two sites form one unit cell.

$$\hat{H} = v \sum_{n=1}^{N} |n, A\rangle \langle n, B| + w \sum_{n=1}^{N-1} |n, B\rangle \langle n+1, A| + \text{H. c.}. \tag{1}$$

The bulk of the chain, found for example by taking periodic boundary conditions, exhibits two bands. The band structure is formulated in reciprocal space, reached via spatial Fourier transformation, where the eigenvalues of $\hat{H}$ are

$$E(k) = \pm\sqrt{v^2 + w^2 + 2vw\cos(k)}, \quad k \in (-\pi, \pi) \tag{2}$$

as depicted in figure 2. The band gap disappears for $v = w$, where the chain is electronically conducting. In the other extreme case, $w = 0$, each unit cell is isolated with flat band structure.

Topological features emerge in the case $w > v$, where two new eigenstates that are localized at the boundary of the chain appear. Their amplitude decays exponentially inside the bulk. The qualitative change of features at the boundary is accompanied by the change of a discrete topological invariant which is defined over the eigenstates of the bulk. It is zero for $w < v$ and jumps to a nonzero value for $w > v$ when crossing the electronically conducting configuration $v = w$. The correspondence between bulk and boundary properties is a hallmark feature of topology. In the following sections we will have a detailed look at the band structure and appearance of edge states within the classical equations of motion.

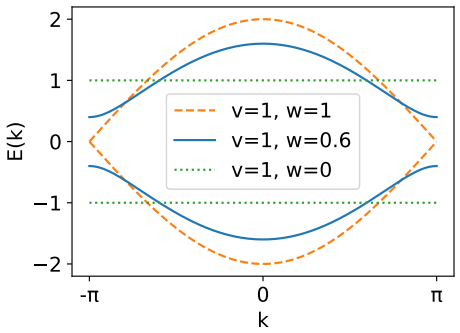

Figure 2: Bulk band structure according to equation (2). Note that $E(k)$ is symmetric under exchange of v and w.

Publications on the SSH model, that are using quantum systems, derive band structure and topological properties from the Hamiltonian above [15, 17], while publications on classical topological materials [12, 13] use equations of motions themselves to run formally the same calculations and obtain comparable results. Since the classical and quantum behavior are analogous, we should be able to close this gap and derive a classical Hamiltonian that reflects these properties. It is even possible to formulate it in a way formally equivalent to the language of second quantization by using classical complex variables.

The circuit that we are working with in the following sections is based on the experiment by Lee et al. as presented in ref. [13], which presents the construction of the circuit Laplacian quite comprehensibly.

2.1 EQUATIONS OF MOTION

The equations of motion for electronic circuits can be derived from the circuit schematic using two frameworks [18]. One is the *mesh analysis* using Kirchhoff's voltage law, stating that the sum of voltages along any loop through the circuit has to be zero as a result of Faraday's law of induction. The other is *nodal analysis* using Kirchhoff's current law (KCL), stating that the sum of currents at each node of the circuit has to be zero due to charge conservation. They are related via the duality of electromagnetism reflected in the fact that electronic circuits have dual counterparts with analogous equations of motion. We choose to use nodal analysis, because it will be easier to describe external driving at circuit nodes in this framework.

The SSH circuit has the convenient property (as the U(1) circuit will have), that all nodes are connected to ground directly via inductors and therefore no spanning tree, nor a distinction between active and passive nodes is needed [19]. Also the circuits in this thesis are running at frequencies between 1 kHz to 1 MHz, the low to ultra low frequency radio bands, with wavelengths above 300 m, which is well above circuit dimensions. This allows the lumped element approximation, that electric and magnetic fields are constrained inside the circuit elements and the physical circuit layout

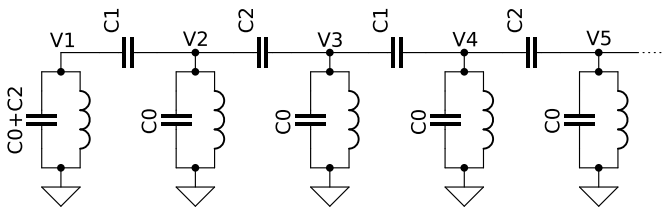

Figure 3: Circuit schematic of SSH model. Parallel LC resonators form sites and are connected by alternating coupling capacitors C_1, C_2. All inductors have the same value L.

has negligible effect. It also means that inductor coils should be only very inefficient antennas and not radiate energy away.

The current-voltage relationship for the circuit elements form terms in the KCL with current I through the element and voltage V across its pins. For capacitors with capacitance C we have

$$I(t) = \dot{Q}(t) = C\,\dot{V}(t), \tag{3}$$

where Q is the stored charge. The over-dot denotes a total time derivative. Inductors follow

$$V(t) = \dot{\Phi}(t) = L\,\dot{I}(t) \tag{4}$$

with inductance L and the magnetic flux Φ stored in the magnetic field. All voltages are referenced to one potential, called ground with $V = 0$. The arbitrary choice of potential and ground node is analogous to the gauge freedom of electromagnetic field theory [19], and allows the elimination of the ground node from the dynamics. Now we can write down the KCL for all nodes in figure 3:

$$\begin{aligned}
\dot{I}_1 &= \frac{1}{L}V_1 + C_0\ddot{V}_1 + C_2\ddot{V}_1 + C_1(\ddot{V}_1 - \ddot{V}_2) \\
\dot{I}_2 &= \frac{1}{L}V_2 + C_0\ddot{V}_2 + C_1(\ddot{V}_2 - \ddot{V}_1) + C_2(\ddot{V}_2 - \ddot{V}_3) \\
\dot{I}_3 &= \frac{1}{L}V_3 + C_0\ddot{V}_3 + C_2(\ddot{V}_3 - \ddot{V}_2) + C_1(\ddot{V}_3 - \ddot{V}_4) \\
&\dots
\end{aligned} \tag{5}$$

The currents on the left-hand side are external currents and are set to zero if the node is not connected to any external driving.

The solution to this second-order linear differential equation is neatly formulated in Fourier space where the equations of motion become the algebraic expression $\tilde{I}(\omega) = J(\omega)\cdot\tilde{V}(\omega)$:

$$\tilde{I}(\omega) = \begin{pmatrix}
\frac{1}{i\omega L} + i\omega C_\Sigma & -i\omega C_1 & & & \\
-i\omega C_1 & \frac{1}{i\omega L} + i\omega C_\Sigma & -i\omega C_2 & & \\
 & -i\omega C_2 & \frac{1}{i\omega L} + i\omega C_\Sigma & -i\omega C_1 & \\
 & & & & \ddots
\end{pmatrix} \cdot \tilde{V}(\omega) \tag{6}$$

with $C_\Sigma = C_0 + C_1 + C_2$. Here I and V are vectors along the chain and the tilde denotes Fourier transformed quantities using

$$\tilde{x}(\omega) = \mathcal{F}[x] = \int_{-\infty}^{\infty} x(t)\, e^{-i\omega t}\,\mathrm{d}t\,. \tag{7}$$

There is a slightly more rigorous solution using the Laplace transformation, common in signal processing, instead of the Fourier transformation. It gives

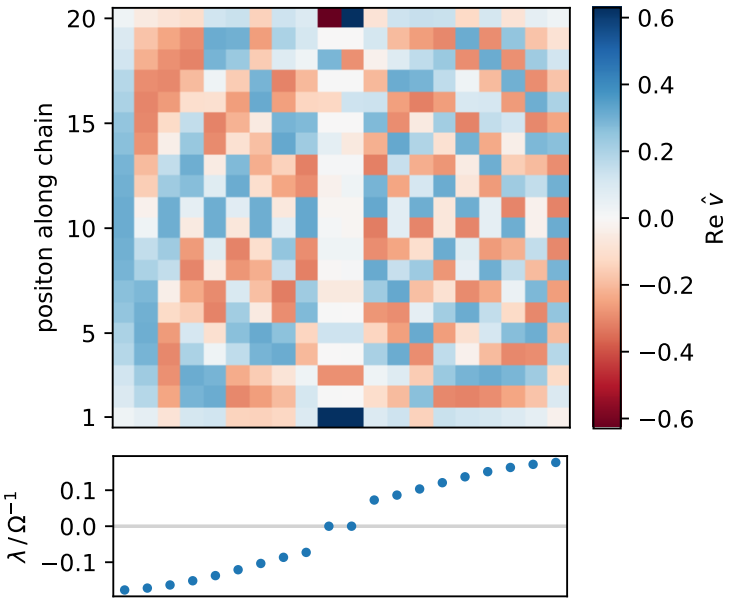

Figure 4: Set of eigenvalues λ and above their associated eigenvectors $\hat{v}$ of $J(\omega)$ at the resonance frequency $\omega = \omega_0$ and $t = 2.2$. Pairs of eigenvalues and -vectors are sorted ascending along abscissa. Note how larger eigenvalues correspond to higher spatial modes. The two columns in the middle show the hybridized edge states with near zero eigenvalues.

its name to the matrix $J(\omega)$, which is also called the *circuit Laplacian*. The inverse $G(\omega) = J^{-1}(\omega)$ is the system's Green's function, providing the solution $\tilde{V} = G\,\tilde{I}$ for any external driving $\tilde{I}$.

2.2 APPEARANCE OF EDGE STATES

A band structure is usually the set of eigenvalues of a Hamiltonian labeled by some parameter, e. g. k as above in eq. (2). The band structure of the SSH Hamiltonian is also hiding in the eigenvalues of the circuit Laplacian $J(\omega)$. The eigendecomposition $J = P\Lambda P^{-1}$, with Λ being the diagonal matrix of eigenvalues of J, allows writing

$$\tilde{V} = G\,\tilde{I} = P\,\Lambda^{-1}\,P^{-1}\,\tilde{I}. \tag{8}$$

This shows that eigenvectors of J, which are column vectors of P, are normal modes of the circuit. Zero eigenvalues of J cause poles in the Green's function G, measured as resonances.

When setting periodic boundary conditions, a Fourier transformation along unit cells block diagonalizes J and allows analytic access to the eigenvalues.

We will execute this explicitly for the Hamiltonian later on and for now just write them down:

$$\lambda_{\pm}(k) = i\omega C_{\Sigma}\left(1 - \frac{1}{\omega^2 L C_{\Sigma}} \pm \frac{C_1}{C_{\Sigma}}\sqrt{1 + t^2 + 2t\cos(k)}\right) \tag{9}$$

with $t = C_2/C_1$ and $k = 2\pi y/N$, where $y = 1 \dots N$ is indexing spatial modes along the chain. The capacitors C_1 and C_2 correspond directly to the coupling strengths v and w in the quantum model of eq. (1) and $t = C_2/C_1 = w/v$. By scanning ω, it is possible to let each eigenvalue cross zero, thereby producing a resonance. We will use this effect to uncover the band structure in measurements. At the uncoupled resonance frequency $\omega_0 = 1/\sqrt{LC_{\Sigma}}$ the offset vanishes and the eigenvalues reproduce the spectrum of the quantum model.

Without periodic boundary conditions, it is possible for edge states to appear. Figure 4 plots the eigenspectrum and associated eigenvectors of $J(\omega_0)$ with $t = 2.2$, which is a topologically non-trivial case on resonance. The normal modes are harmonics and larger eigenvalues correspond to higher spatial harmonics. Each left and right edge state have zero eigenvalues and decay exponentially inside the bulk, but due to the exponential tail they hybridize into a symmetric and an antisymmetric mode with eigenvalues slightly different from zero.

When moving to $t < 1$ the edge states disappear by becoming part of the continuous band structure. This happens at the conducting configuration $t = 1$, or equivalently $v = w$, where also the bulk eigenvalues at $k = \pm\pi$ become zero (see figure 2). We will continue the discussion about topology after having introduced the Hamiltonian and complex variables.

2.3 HAMILTONIAN FORMULATION

2.3.1 *Lagrange function*

The first step towards writing the Hamiltonian is to choose appropriate variables and write down the Lagrange function. The generalized flux Φ, sometimes called flux linkage, is the integral over voltage ($V = \dot{\Phi}$) and is associated to a node in the circuit, not a loop.[1] We choose this variable as generalized coordinate for the Lagrangian, because it is a common choice in quantum electromagnetic circuits and also will be a good choice for the U(1) model. In addition, it eliminates the derivative from the external currents. The equations of motion in the new generalized coordinates read

$$\begin{aligned} I_1 &= \frac{1}{L}\Phi_1 + C_0\ddot{\Phi}_1 + C_2\ddot{\Phi}_1 + C_1(\ddot{\Phi}_1 - \ddot{\Phi}_2) \\ I_2 &= \frac{1}{L}\Phi_2 + C_0\ddot{\Phi}_2 + C_1(\ddot{\Phi}_2 - \ddot{\Phi}_1) + C_2(\ddot{\Phi}_2 - \ddot{\Phi}_3) \\ I_3 &= \frac{1}{L}\Phi_3 + C_0\ddot{\Phi}_3 + C_2(\ddot{\Phi}_3 - \ddot{\Phi}_2) + C_1(\ddot{\Phi}_3 - \ddot{\Phi}_4) \\ &\dots \end{aligned} \tag{10}$$

The Lagrange function $\mathcal{L}(\Phi, \dot{\Phi})$ that results in these equations of motions via the Euler-Lagrange equations is

$$\mathcal{L}(\Phi, \dot{\Phi}) = \sum_{x=1}^{l} \left(\frac{C_\Sigma}{2}\dot{\Phi}_x^2 - \frac{1}{2L}\Phi_x^2 \right) - \sum_{x=1}^{l-1} C_x\, \dot{\Phi}_x\, \dot{\Phi}_{x+1} \tag{11}$$

for a chain of l sites and $C_x = C_1$ if x odd or $C_x = C_2$ if x even. External currents I_x were set to zero. Equivalently we could have reached this result by summing over all energies $\mathcal{E}_L$ and $\mathcal{E}_C$ stored in inductors and capacitors, namely

$$\mathcal{E}_L = \frac{1}{2L}\,\Phi^2 \quad \text{and} \quad \mathcal{E}_c = \frac{1}{2}\,C\dot{\Phi}^2. \tag{12}$$

The Lagrange function may be written more concisely using matrices C for capacitances and W for inverse inductances:

$$\mathcal{L}(\Phi, \dot{\Phi}) = \tfrac{1}{2}\dot{\Phi}^\intercal C\,\dot{\Phi} - \tfrac{1}{2}\Phi^\intercal\, W\,\Phi. \tag{13}$$

While the matrix W is diagonal, C has a structure resembling the circuit Laplacian $J(\omega)$ containing the alternating coupling.

1 Flux linkage is simply defined as integral over the voltage and does not always correspond to an actual flux. In the SSH model it is equal to the flux of the corresponding inductors.

The next step for obtaining the Hamiltonian is to calculate the conjugate momentum. For the flux it turns out to be the sum of charges stored in capacitors connected to each node:

$$\begin{aligned} Q &= \frac{\partial \mathcal{L}}{\partial \dot{\Phi}} = C\,\dot{\Phi} \quad \text{or} \\ Q_x &= C_\Sigma \dot{\Phi}_x - C_{x-1}\dot{\Phi}_{x-1} + C_x \dot{\Phi}_{x+1}. \end{aligned} \tag{14}$$

To perform the Legendre transformation we need the inverse of this relation, $\dot{\Phi} = C^{-1}Q$, but the off-diagonal elements cause the inverse C^{-1} to be rather unpleasant. Note that using the dual circuit ends up with the same problem of having the coupling in the momentum term. There are three options for handling this:

1. Hold fast and stick with it through the Legendre transformation. However the resulting Hamiltonian is all over the place and distinct features of the system are buried in superfluous terms. We will not choose this path.

2. Use the eigendecomposition of $C = P^\dagger \Lambda_C P$ and change variables $\Phi \to \Phi' = P\Phi$, where P is unitary because C is normal. This transformation should be very similar to the one for the circuit Laplacian $J(\omega)$, due to the similar structure. The complexity of the coupling is moved from the momentum terms to the potential terms:

$$\mathcal{L}(\Phi', \dot{\Phi}') = \tfrac{1}{2}\dot{\Phi}'^{\mathsf{T}} \Lambda_C\, \dot{\Phi}' - \tfrac{1}{2}\Phi'^{\mathsf{T}}\, P\, W\, P^\dagger \Phi'. \tag{15}$$

3. Use the small coupling approximation $C_{1,2} \ll C_\Sigma$ such that

$$Q_x \approx C_\Sigma \dot{\Phi}_x. \tag{16}$$

   What this does, is to neglect the charges on the coupling capacitors and with them the nearest-neighbor dependence. The definition of Q becomes 'local,' similar to the tight-binding model of condensed matter physics, which assumes electron wave functions to be localized close to their atoms.

While the second option easily produces an exact result, it can be only applied for linear LC networks. To get a recipe also applicable for the U(1) model, we will use the small coupling approximation and write:

$$\begin{aligned} H(\Phi, Q) &= Q \cdot \dot{\Phi} - \mathcal{L}(\Phi, \dot{\Phi}) \\ &= \frac{1}{2}\sum_{x=1}^{l} \left(\frac{1}{C_\Sigma} Q_x^2 + \frac{1}{L}\Phi_x^2 \right) - \sum_{x=1}^{l-1} \frac{C_x}{C_\Sigma^2} Q_x Q_{x+1}. \end{aligned} \tag{17}$$

The important coupling term now looks like $Q_x Q_{x+1}$.

2.3.2 *Complex canonical variables*

Before continuing, it is convenient to change to dimensionless variables by dividing out scales set by the voltage V_0 and frequency ω_0:

$$\begin{aligned} \bar{\Phi} &= \Phi/\Phi_0, \qquad \Phi_0 = \sqrt{L\,C_\Sigma}\,V_0 = V_0/\omega_0, \\ \bar{Q} &= Q/Q_0, \qquad Q_0 = C_\Sigma\,V_0. \end{aligned} \tag{18}$$

Upon factoring out $H_0 = Q_0^2/C_\Sigma$ the remaining terms in the Hamiltonian $\bar{H} = H/H_0$ become dimensionless:

$$\bar{H}(\bar{\Phi},\bar{Q}) = \frac{1}{2}\sum_{x=1}^{l}\left(\bar{Q}_x^2 + \bar{\Phi}_x^2\right) - \sum_{x=1}^{l-1}\frac{C_x}{C_\Sigma}\bar{Q}_x\bar{Q}_{x+1}. \tag{19}$$

In this equation it is evident that the coupling strength is set by the ratio C_x/C_Σ. For the equations of motion, also the time needs to be made dimensionless, and it turns out that using the resonance frequency as timescale, $t \to \tau = t\omega_0$, allows Hamilton's equations to appear unchanged:

$$\frac{\mathrm{d}\bar{\Phi}}{\mathrm{d}\tau} = \frac{\partial\bar{H}}{\partial\bar{Q}}, \quad \frac{\mathrm{d}\bar{Q}}{\mathrm{d}\tau} = -\frac{\partial\bar{H}}{\partial\bar{\Phi}}. \tag{20}$$

As promised, we now perform the variable change that brings the expression close to the formulation of second quantization, so that intuition from quantum mechanics becomes easier to apply. Complex classical variables stand in for raising and lowering operators, and as a result e. g. phase shifts can be achieved by multiplying variables with a complex phase instead of rotating (Φ, Q). These complex variables are defined as

$$\begin{aligned} a_x &= \tfrac{1}{\sqrt{2}}(\bar{Q}_x + i\bar{\Phi}_x) \\ a_x^* &= \tfrac{1}{\sqrt{2}}(\bar{Q}_x - i\bar{\Phi}_x), \end{aligned} \tag{21}$$

where a^* and a are treated as independent variables with the additional restriction that the complex conjugate of a is equal to a^* [20]. Unfortunately the variable change $(\bar{\Phi},\bar{Q}) \to (a, a^*)$ is not *restricted* canonical,[2] because the Poisson bracket in terms of the old variables evaluates to

$$\{a_x, a_y^*\}_{\bar{\Phi},\bar{Q}} = \sum_j\left(\frac{\partial a_x}{\partial\bar{\Phi}_j}\frac{\partial a_y^*}{\partial\bar{Q}_j} - \frac{\partial a_x}{\partial\bar{Q}_j}\frac{\partial a_y^*}{\partial\bar{\Phi}_j}\right) = i\delta_{xy} \tag{22}$$

instead of unity.

2 Restricted canonical transformations do not allow prefactors in the equations of motion that could be removed by absorbing into the variable change, as extended canonical transformations would allow. Here we deliberately choose an extended transformation to reach complex variables. Terminology regarding classical mechanics follows Goldstein's *Classical Mechanics* [21]. Furthermore, the same definition of the Poisson brackets (eq. 22) is used for real and complex variables.

Thus after replacing the variables in the Hamiltonian,

$$H(a,a^*) = \sum_{x=1}^{l} a_x^* a_x - \sum_{x=1}^{l-1} 2\frac{C_x}{C_\Sigma}(a_x + a_x^*)(a_{x+1} + a_{x+1}^*), \tag{23}$$

we also have to adapt the equations of motion to

$$-i\dot{a} = \frac{\partial H(a,a^*)}{\partial a^*}, \quad i\dot{a}^* = \frac{\partial H(a,a^*)}{\partial a} \tag{24}$$

to preserve the physical description. Note that in general, the derivative by a complex conjugate is not well-defined but here we treat a^* as independent variable. One of the two Hamilton equations are now redundant, because they are required to be conjugate, while original variables have become real and imaginary parts.

2.3.3 *Rotating wave approximation*

There is one more step in order to reach a beautiful form: the elimination of some cross-terms in the coupling via rotating wave approximation. In quantum mechanics the rotating wave approximation is done in the interaction picture, where states or operators—depending on picture—absorb the uncoupled time evolution, such that only the interaction remains. Our uncoupled Hamiltonian is

$$H_0(a,a^*) = \sum_{x=1}^{l} a_x^* a_x. \tag{25}$$

with solution $a_x(\tau) = a'_x\, e^{i\tau}$. There is no explicit frequency variable here, because the resonance frequency was absorbed into the time definition when choosing dimensionless quantities. The interaction picture uses this solution after exchanging the prefactor a'_x for the new time dependent variable $b_x(\tau)$. The change to this new set of variables is

$$\begin{aligned} a &\to b = e^{-i\tau}\, a, \\ a^* &\to b^* = e^{i\tau}\, a^*. \end{aligned} \tag{26}$$

It is a canonical transformation but the Hamiltonian changes form, because the transformation is time-dependent. Just as in the interaction picture of quantum mechanics, H_0 is removed, leaving

$$H(b,b^*) = -\sum_{x=1}^{l-1} 2\frac{C_x}{C_\Sigma}\left(e^{2i\tau} b_x b_{x+1} + b_x^* b_{x+1} + \text{H. c.}\right). \tag{27}$$

We separate the dynamics at the typical timescale chosen before and drop terms oscillating twice as fast. What remains is

$$H(b, b^*) = -\sum_{x=1}^{l-1} 2\frac{C_x}{C_\Sigma}(b_x^* b_{x+1} + b_{x+1}^* b_x). \tag{28}$$

When interpreting b and b^* as annihilation and creation operators, the Hamiltonian is formally the same as the quantum version in eq. (1). The coupling term represents the same nearest-neighbor hopping with alternating coupling. As pointed out by Imhof et al. [12], the variables in classical mechanics commute as bosonic operators do (as opposed to anticommuting fermionic creation and annihilation operators). This changes the degrees of freedom and may affect symmetries.

2.3.4 *Matrix formalism*

After all these gymnastics we also have arrived at a form that can be expressed using a matrix with a structure similar to the circuit Laplacian $J(\omega)$:

$$H(b, b^*) = b^\dagger \begin{pmatrix} 0 & -\gamma & & & \\ -\gamma & 0 & -\gamma t & & \\ & -\gamma t & 0 & -\gamma & \\ & & -\gamma & 0 & \\ & & & & \ddots \end{pmatrix} b = b^\dagger \hat{H} b \tag{29}$$

where $\gamma = 2C_1/C_\Sigma$ and as before $t = C_2/C_1$. The vector of all b_x is called b, and $b^\dagger$ is the row-vector of all b_x^*. We will call the matrix $\hat{H}$. It is Hermitian, from which follows that all of its eigenvalues are real. This ensures that the Hamiltonian will be real for any (b, b^*).

Note how with this matrix formalism in complex variables, Hamilton's equations are formally equivalent to the Schrödinger equation:

$$-i\dot{b} = \frac{\partial H}{\partial b^*} = \hat{H} b, \tag{30}$$

give or take the sign.[3] Using the eigendecomposition $\hat{H} = P^\dagger \Lambda P$, where Λ is a diagonal matrix of eigenvalues of $\hat{H}$ and P a unitary matrix,[4] the solution to the equations of motion is

$$b(t) = U^\dagger e^{i\Lambda\tau} U b_0 \tag{31}$$

for initial value b_0.

3 The sign of Hamilton's equations could be inverted by swapping Φ and Q in the definition of the complex variables.

4 Assuming that $\hat{H}$ is diagonalizable, which it is in our case.

Furthermore, the time evolution of any quantity $G(b, b^*)$ derived from the canonical variables is given by the Poisson brackets [21]. If this quantity can be written as $G = b^\dagger \hat{G} b$ with some matrix $\hat{G}$, the Poisson brackets reduce to the commutator:

$$-i\,\dot{G} = \{G, H\} = b^\dagger\,[\hat{G}, \hat{H}]\,b, \tag{32}$$

where we have taken H to be time independent for now. $\hat{G}$ is a symmetry if and only if it commutes with $\hat{H}$. The similarity to the quantum world is not surprising considering the construction of quantum mechanics via canonical quantization [22].

2.4 SYMMETRY & TOPOLOGY

2.4.1 *Lattice momentum*

In the previous sections, the band structure already showed up. Now we use the Hamiltonian to explicitly execute the spatial Fourier transformation for reciprocal space. As mentioned before, the band structure is formulated for the bulk Hamiltonian by imposing periodic boundary conditions, so that the Hamiltonian attains translational symmetry. Translations form a discrete, periodic group and are associated to the discrete, periodic lattice momentum k, which is conserved. For an infinitely long chain, $N \to \infty$, also called the thermodynamic limit, lattice momentum becomes continuous as the symmetry group becomes infinite. We will follow the arguments as made by Asbóth et al. [23].

The spatial Fourier transformation $b \to \tilde{b}$ is performed on the left and right sites separately along the unit cells, so we change indexing from every site x to unit cell based $(n, A/B)$ with $n = 1 \dots N$ where $N = l/2$. Left and right sublattices are denoted by A and B. The Fourier series is

$$b_{n,A/B} = \frac{1}{\sqrt{N}} \sum_k \tilde{b}_{k,A/B}\, e^{ikn}, \tag{33}$$

where k takes on the values $k = \frac{2\pi y}{N}$ with $y = 1 \dots N$. This transformation is a canonical variable change. After executing it for left and right sites of the unit cells the Hamiltonian becomes block diagonal:

$$H(b, b^*) = b^\dagger \begin{pmatrix} \tilde{H}(k=0) & & \\ & \tilde{H}(k = 2\pi\frac{1}{N}) & \\ & & \ddots \end{pmatrix} b. \tag{34}$$

Each block represents one of N subsectors in phase space which have independent solutions. They are labeled by the momentum k:

$$\tilde{H}(k) = \begin{pmatrix} 0 & -\gamma(1 + te^{-ik}) \\ -\gamma(1 + te^{ik}) & 0 \end{pmatrix}. \tag{35}$$

The eigenvalues of $\tilde{H}(k)$ are

$$\lambda_{\pm}(k) = \pm\gamma\sqrt{1 + t^2 + 2t\cos(k)}. \tag{36}$$

and provide—up to prefactors—the same result as the circuit Laplacian's eigenvalues (eq. 9). Each eigenvalue has a counterpart of opposite sign. The reason for this is chiral symmetry.

2.4.2 *Chiral symmetry*

The chiral symmetry operator on $\tilde{H}(k)$ is

$$\sigma_z = \begin{pmatrix} 1 & 0 \\ 0 & -1 \end{pmatrix}, \tag{37}$$

which switches the sign on the right sublattice. For the full Hamiltonian, the direct sum $\Gamma = \oplus_k \sigma_z$ is used. The symmetry group has two elements ($\mathbb{1}$ and Γ) and the SSH Hamiltonian fulfills

$$\Gamma\,\hat{H}\,\Gamma = -\hat{H}. \tag{38}$$

Note the additional minus sign: in the quantum mechanical language symmetries usually have to commute with the Hamiltonian, but chiral symmetry is defined via anticommutation. Chiral symmetry requires each state to have a chiral counterpart with negative energy eigenvalue:

$$\hat{H}\,b = \lambda b \quad \Rightarrow \quad \hat{H}\,\Gamma\,b = -\Gamma\,\hat{H}\,b = -\lambda\,\Gamma\,b. \tag{39}$$

Only zero-energy states are their own chiral counterpart. When crossing from the topologically trivial case $t < 1$ over $t = 1$, the band gap closes at $k = \pm\pi$. There the states from the lower and upper band meet at zero energy and form zero-energy eigenstates, that stay at zero energy for $t > 1$.

The SSH model has a $\mathbb{Z}_2$ symmetry, $a_x \to -a_x$, which is a local, discrete, and finite symmetry group. In quantum mechanics, discrete symmetries are related to selection rules, e. g. for parity. In this classical case it is not clear whether there is a related concept for this symmetry.

2.4.3 *Calculation of edge states*

The interesting property of edge states in the field of topological insulators is, that they have zero energy, which is usually chosen to correspond to the Fermi energy. In that way they support electronic conduction. We may use the zero-energy condition $H(b, b^\dagger) = 0$ to derive the left and right edge states. It follows that either $b = 0$ or

$$t\, b_{y+1,A} = -b_{yA} \quad \text{and} \quad b_{y+1,B} = -t\, b_{y,B} \tag{40}$$

with $0 = b_{1B}$ and $0 = b_{NA}$ at the boundaries. These are separate solutions for sublattices A and B with one side of the boundary fixed. When disregarding the boundary conditions, the solutions are exponentials:

$$\begin{aligned} b_{yA} &= b_{1A}(-t)^{-(y-1)}, \\ b_{yB} &= b_{NB}(-t)^{y-N}. \end{aligned} \tag{41}$$

For $t < 1$, the exponential is rising to the side where the boundary condition holds, thereby suppressing this state. But for $t > 1$, the boundary conditions constrain only the last element in the exponential tail. In the thermodynamic limit, $N \to \infty$, or even long enough chains, this allows approximate solutions that are non-zero.

For the numerically calculated eigenvectors of the circuit Laplacian (figure 4) we have already seen that these two solutions on sublattice A and B hybridize to a symmetric and an antisymmetric state. They have slightly non-zero energies determined by the overlap of the exponential tails. Thus the splitting between them is exponentially small in the system size [23].

2.5 TRANSMISSION & TWO-POINT IMPEDANCE

Measurements should probe the Green's function $G(\omega)$ derived before. A common way of measuring its properties is via transmission measurements, but for the edge states we will use a resistance measurement as presented by Lee et al. [13]. The expected structure of the Green's function is shown in figure 5 for both with and without edge states. In the former case, the isolating property is nicely discernible in the way the amplitude decays away from the diagonal terms, i. e. driving at one site does not propagate far.

The two hybridized energy states are not exactly at ω_0, but slightly above and below. At the lower frequency one, G has the shape as in figure 5b. Due to the hybridization, when exciting one end of the chain, the opposite end should show a significant signal.

Transmission specifies the amount of signal that passed between two points in the system. The setup for a transmission measurement is to connect a

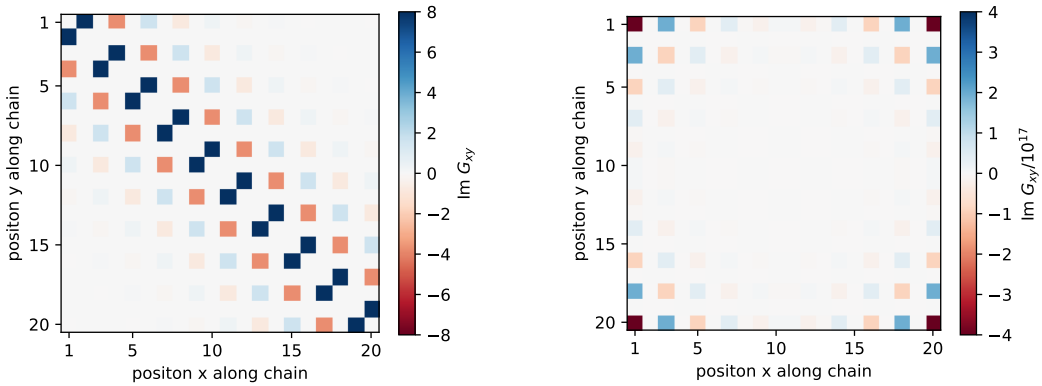

(a) Isolating configuration $t = 1/2.2$. Frequency at $f_0 = \omega_0/2\pi$ in the middle of the band gap.

(b) Edge state, $t = 2.20$. Frequency at the resonance of the lower hybridized edge state.

Figure 5: Components of $G(\omega)$ for different configurations showing isolating properties and edge states. Calculated for $l = 20$ sites or $N = 10$ unit cells respectively. Note that $G(\omega)$ is purely imaginary, i. e. $\operatorname{Re} G = 0$.

current driver at one site x (w. r. t. ground), so the external currents are $I_i = I_0\delta_{ix}$ with amplitude I_0. Then compare the voltage of the driven site x to another site y:

$$T_{x,y} = \frac{V_y}{V_x} = \frac{G_{yi}I_i}{G_{xj}I_j} = \frac{G_{yx}}{G_{xx}}, \tag{42}$$

all at the frequency of the current driver. The problem with this measurement is that the divergence associated with an edge state in component G_{xy} or G_{xx} may be covered by a zero or divergence of the other component.

To solve this, the two-point impedance is used. By driving an alternating current I_0 at a frequency ω into site x of the chain and out of site y, the external currents are set to $I_i = I_0(\delta_{ix} - \delta_{iy})$. The measured voltage across these sites divided by the current gives the two-point impedance

$$Z_{xy} = \frac{V_y - V_x}{I_0} = \frac{G_{yi}I_i - G_{xj}I_j}{I_0} = G_{yx} + G_{xy} - G_{xx} - G_{yy}. \tag{43}$$

Poles in at least one of the components of $G(\omega)$ above should be evident as peaks of $Z_{xy}(\omega)$. One might intuitively expect, that large impedance / resistance would be the opposite of a resonance of the circuit, but since the external current has constant amplitude, a diverging impedance implies very large voltage amplitudes.

2.6 EXPERIMENT

The circuit was reproduced with the same dimensioning as presented by Lee et al. [13]. It is different from the one we have been studying until now,

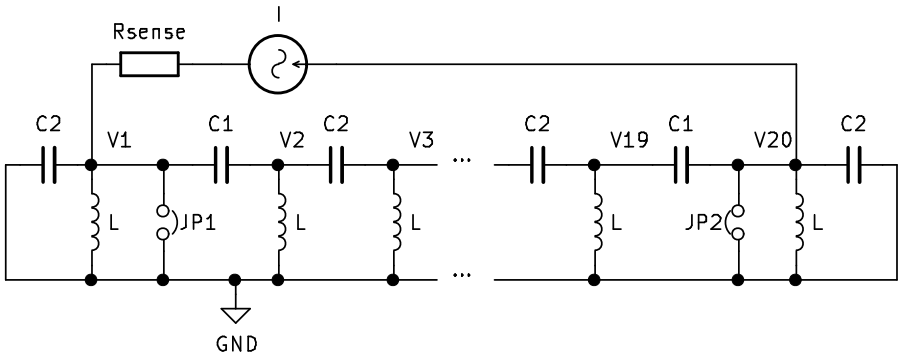

Figure 6: Schematic of circuit as built. Jumpers JP1 and JP2 allow switching configurations. Capacitors values are $C_1 = 100\,\mathrm{nF}$ and $C_2 = 220\,\mathrm{nF}$ and all inductors are the same $L = 10\,\mu\mathrm{H}$. Also shown is the setup for the two-point impedance measurement for $Z_{1,20}$ with series resistor $R_{\mathrm{sense}} = 33\,\Omega$.

because the on-site capacitor C_0 is omitted. This is equivalent to $C_0 \to 0$ and $C_\Sigma = C_1 + C_2$. Ningyuan et al. [11] point out, that this limit is desirable to reduce the sensitivity to disorder. They state, that this corresponds to changing from the tight-binding limit to a scale-invariant regime where the particular capacitor and inductance values impact only the overall energy scale of the band structure.

The schematic is shown in figure 6 together with the current driver connections for an impedance measurement. See appendix B.1 for a list of all parts. The finished board is shown in figure 7.

For measurements we use a Red Pitaya (STEM 125-14 v1.0), a multipurpose *system on a chip* (i. e. FPGA + CPU). It has two fast analog input channels and two RF output channels, the latter with 50 Ω impedance, all digitized at 14 bits with a bandwidth of 50 MHz. Outputs have a sample rate of 125 Msps and inputs can be set to predefined values up to 125 Msps. Measurement scripts are compiled and run on the Debian Linux system directly on chip.[5] In the scripts, the sample rate for the inputs are chosen to be the smallest sample rate that still ensures at least 20 samples per period of the expected signal. When lowering the sample rate, the digital-to-analog converter still runs at 125 Msps and averages the signal for the lower sample rate.

For scanning the frequency, the analog output is set to one frequency and then activated. The analog input buffers, which can hold $n = 16384$ samples, are filled and read out. Then the process is repeated for the next frequency step. For each step the resulting wave forms are demodulated by the measurement script running on the Red Pitaya using quadrature amplitude demodulation.[6] This speeds up the process, because instead of the full wave form, only its amplitude and phase need to be transmitted and stored on the computer.

5 Measurement scripts available at https://github.com/tychon/redpitaya-measurements

6 This demodulation method basically calculates a single summand of the Fourier series of the result at the desired frequency.

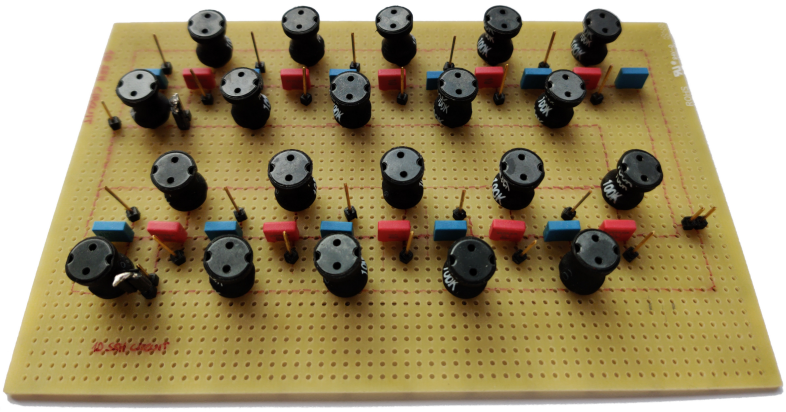

Figure 7: Picture of SSH model setup. Conveniently, capacitors have distinct colors (blue for 220 nF, red for 100 nF). Black cylinders are inductors. Wiring on the bottom of the prototyping board is indicated by red lines. Topological phases can be switched by jumpers.

2.6.1 *Two-point impedance*

The two-point impedance measurement requires a controlled current source. Since it is also used for the U(1) circuit, the design of the current source is described in section 4.1.7 together with other circuits of the U(1) model. The current driver takes one of the analog voltage outputs of the Red Pitaya and converts it to a current, which in turn is connected to one of the sites, x, via a series resistor R_{sense}. Since the current source is not ideal, R_{sense} is used to measure the actual current.

The ground of the Red Pitaya is not connected to the ground indicated in the schematic, but site y. This leaves the ground of the schematic floating and measured voltages are relative to V_y. One of the fast analog inputs is connected to site x measuring $V_{\text{CH1}} = V_x - V_y$ and the other is connected to the opposite side of the series resistor R_{sense} measuring $V_{\text{CH2}} = V_{\text{sense}} - V_y$. Then the driven current is

$$I = \frac{V_{\text{CH2}} - V_{\text{CH1}}}{R_{\text{sense}}} = \frac{V_{\text{sense}}}{R_{\text{sense}}} \tag{44}$$

and the two-point impedance is

$$Z_{xy} = \frac{-V_{\text{CH1}}}{I} = \frac{V_y - V_x}{I}. \tag{45}$$

The wave forms of interest to calculate I and Z_{xy} are V_{CH1} and $V_{\text{CH12}} = V_{\text{CH2}} - V_{\text{CH1}}$. Figure 8 shows the driving current amplitude calculated according to eq. (44). For an ideal current source it should be flat, but we see a drop-off after about 400 kHz, setting the bandwidth of the current source. The peak just at the bandwidth is typical for feedback stabilized devices with capacitive loads.

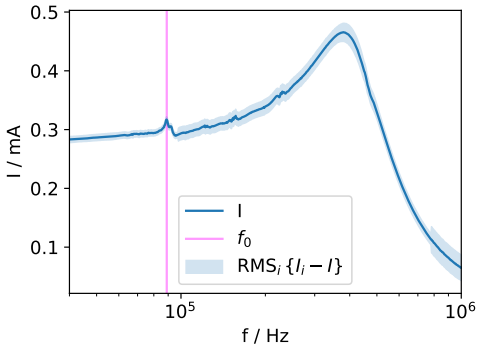

Figure 8: Frequency response of current driver connected to circuit. Output has bandwidth of about 400 kHz and is reasonably robust against resonances of load.

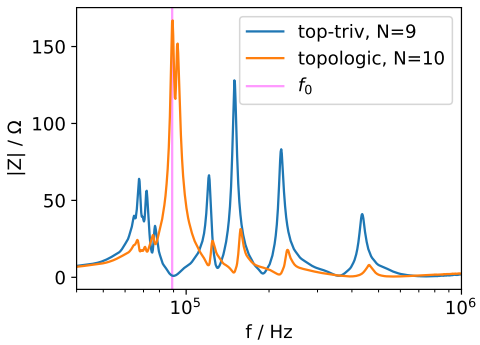

Figure 9: Measurement of two-point impedance across chain in trivial and topological configuration. Edge state appears at expected resonance frequency $f_0 = \omega_0/2\pi$.

The shaded region in figure 8 indicates the demodulation error, which we define here to be the root-mean-square of the difference between the waveform and the demodulated signal. This corresponds to the scatter of the instantaneous signal around the idealized harmonic model. Under the assumption, that the noise of the signal is normal distributed around the harmonic signal at the driving frequency, the error of the recovered signal amplitude is $\sqrt{n} = 128$ times smaller than the demodulation error (with $n = 16384$ the number of samples). The assumption is supported by the fact that averaging over consecutive samples reduces the error, manifesting in lower noise for lower sample rates. This effect is visible as two jumps of the error in figure 8, where the sample rate jumps to the next larger preset and one sample in the buffer is a result of less analog-digital conversions. The assumption would be violated by signal components that are not harmonic or at a different frequency.

The two-point impedance across the whole chain is plotted in figure 9, which shows the expressive result where the edge states can be turned on and off by changing the system's configuration between $t < 1$ and $t > 1$. The two configurations are:

1. The topologically trivial one: Jumpers are connected so that the outer sites 1 and 20 are removed (see schematic in figure 6), resulting in a chain of 9 unit cells with $t = 1/2.2$. Then the two-point impedance $Z_{2,19}$ is measured.

2. The topologically interesting one: With the jumpers open, the full chain has 10 unit cells and the two-point impedance $Z_{1,20}$ is measured.

Both configurations reveal the surrounding band structure according to equation (9). At the frequency $f_0 = \omega_0/2\pi = 89$ kHz the first configuration shows a band gap, while the second configuration has prominent edge states. The splitting of about 4 kHz in the edge states may be attributed to the hybridization, however it is an order of magnitude larger than expected from

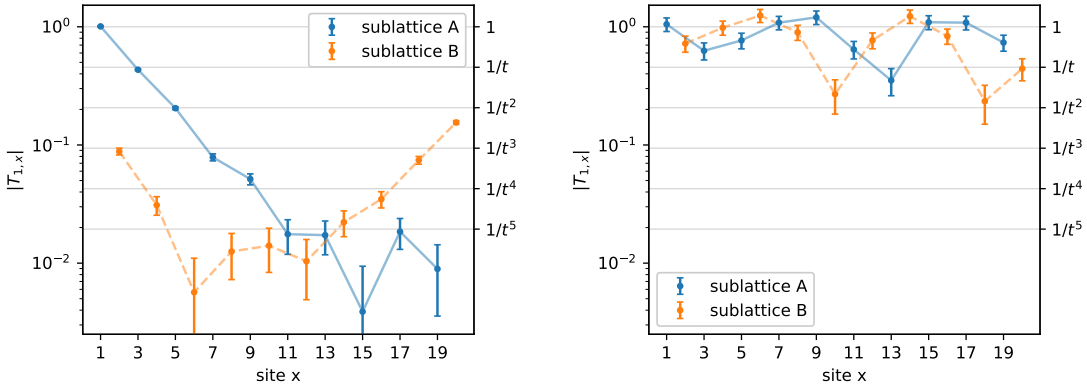

(a) $f = 90\,\mathrm{kHz}$, edge state.

(b) $f = 125\,\mathrm{kHz}$.

Figure 10: Transmission along chain showing the exponential decay of edge states (left), and the more or less harmonic mode of the state corresponding to first resonance above the edge state (right). Error bars indicate demodulation error.

numerical calculation. This effect may be attributed to disorder in the circuit due to tolerances on component values [13].

The demodulation error propagated to the two-point impedance amounts to typically $1\,\Omega$. It is larger at the resonances but stays below $5\,\Omega$. Only at frequencies higher than 800 kHz, the demodulation error becomes larger due to shorter sample averaging.

2.6.2 *Transmission*

A transmission measurement is suitable to check the exponential decay of the edge state into the bulk. The jumpers are opened to get the configuration with $t = 2.2 > 1$ and again with the Howland current pump site 1 is driven. One analog input measures the voltage V_{CH1} at the driven site and the other V_{CH2} at another site x. This time, all referenced to the ground of the circuit. The transmission is then $T_{1,x} = V_{\mathrm{CH2}}/V_{\mathrm{CH1}}$.

Figure 10a shows the absolute value of the transmission from site 1 to the rest of the chain at one of the hybridized edge states. The first few sites show a clear exponential drop-off according to the parameter t as calculated in section 2.4.3. On the other side, the right edge state with the same exponential drop-off is discernible, albeit at a lower amplitude due to dissipation along the chain. Similarly the right eigenstate does not approach zero on the left side of the chain, probably due to dissipation and disorder.

The error bars show the propagated demodulation error, i. e. the noise around the demodulated signal. Note that also here the error on the recovered signal amplitude and similarly $|T|$, is $\sqrt{n}$ times smaller. The deviation from the

expected signal at small values of $|T|$ is thus larger than the noise level and may again be caused by disorder due to manufacturer tolerances for the electronic components.

For comparison, the transmission along the chain was also measured at one of the other resonances, namely the first one above the edge states at 125 kHz. Driving the circuit at this frequency shifts this eigenvalue near zero and the corresponding mode becomes resonant. Figure 10b shows how the signal then propagates along the chain.

2.7 SUMMARY

The construction of a classical circuit, whose circuit Laplacian mimics a quantum Hamiltonian, was presented. For the circuit a classical Hamiltonian could be found that retains the crucial structure—band structure and edge states—under some approximations. While the Hamiltonian describes the system without external forces, the circuit Laplacian has an additional parameter for external driving, as it is formulated for the inhomogeneous equations of motion.

Using an implementation of the circuit, measurements could reproduce results from Lee et al. [13], thereby exploring options on verifying the implementation of the circuit Laplacian. By simply (un)plugging jumpers to interchange intra- and intercell coupling, the edge states could be turned on and off. By omitting C_0 the verification of the Hamiltonian was somewhat obstructed, because the derivation relied on the small-coupling limit. For the U(1) model the implementation will stay within the small-coupling regime.

3

U(1) MODEL: THEORY

For motivating the choice of Hamiltonian for our circuit, let us first look at electromagnetism in quantum mechanics to see how building a U(1) gauge symmetry works. Following ref. [24] we take the Schrödinger equation and a free particle in a potential:

$$i\hbar\dot{\psi} = H\psi, \qquad H = \frac{\boldsymbol{p}^2}{2m} + V(\boldsymbol{x}), \tag{46}$$

and try out a phase transformation on the wave function that is both local and time dependent: $\psi \to \tilde{\psi} = U\psi = e^{i\varphi(\boldsymbol{x},t)}\psi$. Applying the transformation to the wave function is equivalent w. r. t the Schrödinger equation to transforming the Hamiltonian as

$$\begin{aligned} H \to \tilde{H} &= UHU^\dagger + i\hbar\dot{U}U^\dagger \\ &= \frac{1}{2m}\big(\boldsymbol{p} - \hbar\nabla\varphi(\boldsymbol{x},t)\big)^2 + V(\boldsymbol{x}) - \hbar\dot{\varphi}(\boldsymbol{x},t). \end{aligned} \tag{47}$$

Defining the magnetic vector potential $\boldsymbol{A}(\boldsymbol{x},t) = \frac{\hbar}{e}\nabla\varphi(\boldsymbol{x},t)$ and the electric potential $\Phi(\boldsymbol{x},t) = \frac{1}{e}(V(\boldsymbol{x}) - \hbar\dot{\varphi}(\boldsymbol{x},t))$ brings the Hamiltonian into the form

$$\tilde{H} = \frac{(\boldsymbol{p} - e\boldsymbol{A})^2}{2m} + e\Phi, \tag{48}$$

which describes a charged particle in external magnetic and electric fields. H was not invariant under the transformation but changed to $\tilde{H}$, which is invariant, because $\boldsymbol{A}$ and Φ can absorb any further U(1) gauge transformation. In this way we have constructed a version of *minimal coupling*. Here the quantities $\boldsymbol{A}$ and Φ which hold the gauge freedom do not partake in the dynamics and thus are called *static*. The concept of static gauge fields has been put into action in experiments producing artificial external magnetic fields in optical lattices with the aim to simulate condensed matter phenomena [25].

Giving the gauge field dynamics brings us into the realm of field theory. For example *scalar electrodynamics* [26, 27] has a complex scalar field φ and the gauge field A_α in the Lagrangian

$$\mathcal{L} = -\tfrac{1}{4}F^{\alpha\beta}F_{\alpha\beta} - D^\alpha\varphi^*\, D_\alpha\varphi - m^2|\varphi|^2. \tag{49}$$

The first term with $F_{\alpha\beta} = \partial_\alpha A_\beta - \partial_\beta A_\alpha$ is responsible for the dynamics of the electromagnetic field. The other two terms give φ the dynamics of a Klein-Gordon field and also contain the interaction hidden in the gauge-covariant

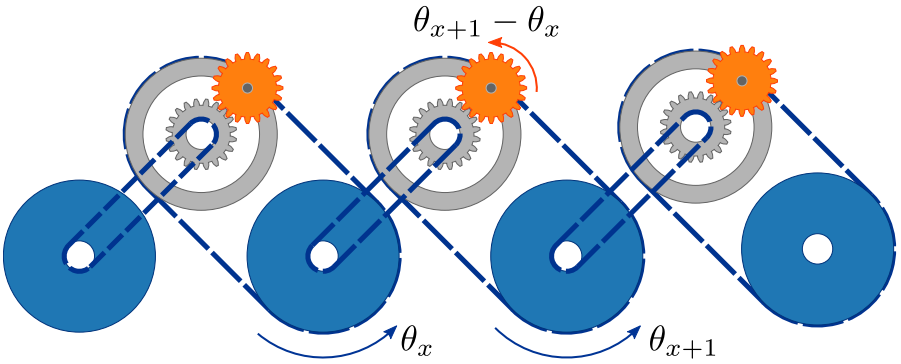

Figure 11: Illustration of the local gauge freedom on a lattice as mechanical gears. The degrees of freedom of these gears match those of the gauge symmetry. Sites (blue wheels) are connected by a coupling (gray and orange) that is designed to absorb their phase (rotation) by a counter rotation (angle of orange wheel).

derivatives $D_\alpha = \partial_\alpha - ieA_\alpha$. In these derivatives the minimal coupling shows up again and when expanded we get non-linear terms like $A^\alpha \varphi^* \partial_\alpha \varphi$.

Turing back to our circuit, we want to incorporate something like minimal coupling to enable a U(1) gauge symmetry. We take the simplified structure of the SSH Hamiltonian (28), keeping only the nearest-neighbor hopping:

$$H(a, a^*) = \lambda \sum_x (a_x^* a_{x+1} + a_{x+1}^* a_x). \tag{50}$$

We check the effect of a local phase transformation $a_x \to e^{i\theta_x} a_x$ and see that terms like $e^{i(\theta_x - \theta_{x+1})}$ are left over. These terms can be absorbed into new canonical variables (b_x, b_x^*):

$$H = \lambda \sum_x (a_x^* b_x^* a_{x+1} + a_{x+1}^* b_x a_x). \tag{51}$$

The newly introduced variables b are called *links*, because they enable the gauge invariant interaction between *sites* a of the one-dimensional lattice. See figure 11 for a hands-on illustration of the gauge freedom. If we take the links to be dynamic, the new interaction has become non-linear, very similar to the interaction between the gauge field and the Klein-Gordon field in scalar electrodynamics. The quantum equivalent of the Hamiltonian with only two sites, reached by interpreting variables as creation and annihilation operators, matches the Jaynes-Cummings model as discussed by Kasper et al. [10].

Note that our Hamiltonian is not the result of discretizing a field theory, and may very well not have a well-defined continuum limit. Furthermore, in contrast to the theories above, our circuit is a one-dimensional lattice and therefore does not support objects comparable to magnetic fields, only electric fields.

We will later see that the gauge transformation is responsible for a local conservation law similar to the Gauss law of electrodynamics. It restricts

the dynamics of the sites and links, such that charges on the sites can move only with the gauge field keeping track of the change.[1] Furthermore, all variables in the classical description are observable, so it is not a gauge theory in the sense that it has unphysical / not observable degrees of freedom. Strictly speaking, that notion arises only in the context of simulating a gauge theory.

The derivation presented in the next sections was set up by heuristically running the calculations of the SSH model in reverse on the desired Hamiltonian we just found. The interaction term turns out to look like $\dot{\Phi}_x \dot{\Phi}'_x \dot{\Phi}_{x+1}$ in the Lagrange function (with the prime denoting the link). It contributes a term to the equations of motion of each site x, $x+1$, and the link in between. The detailed form of the equations of motion was also adjusted for the actual implementation and these considerations will be presented in the section 4.

Starting from that circuit, the following sections present the derivation of the Hamiltonian and its local conservation law. We will then calculate the solution of the Hamiltonian with static gauge field and simulate our way through the non-linear Hamiltonian with dynamic gauge field. The aim is to provide predictions against which the implementation can be benchmarked.

3.1 CIRCUIT HAMILTONIAN

Figure 12 shows a simplified schematic that illustrates the arrangement of the resonators and nodes where the voltages are tapped. Quite similar to the SSH model we have a chain of LC resonators, but here the additional links also have resonators. The interaction is not shown in full detail, but we can already say that it needs to be symmetric under exchange of its connections, because the coupling term $\dot{\Phi}_x \dot{\Phi}'_x \dot{\Phi}_{x+1}$ has this symmetry. Moreover, whatever its circuit may be, all voltages need to be immediately determined by the site and link voltages, because otherwise there would be additional degrees of freedom.

In terms of the Kirchhoff current law, the equations of motion are these:

$$\begin{aligned} \dot{I}_x &= \frac{1}{L_x} V_x + 2C_c \ddot{V}_x - C_c \left(k_{x-1} \frac{\mathrm{d}^2}{\mathrm{d}t^2} V'_{x-1} V_{x-1} + k_x \frac{\mathrm{d}^2}{\mathrm{d}t^2} V'_x V_{x+1} \right), \\ \dot{I}'_x &= \frac{1}{L'_x} V'_x + 2C_c \ddot{V}'_x - C_c k_x \frac{\mathrm{d}^2}{\mathrm{d}t^2} V_x V_{x+1}. \end{aligned} \tag{52}$$

On the left hand side are external currents $I_x^{(\prime)}$ of the Kirchhoff current law. Primed quantities denote the links and the index x runs from 1 to l for site

1 In analogy to the quantum version, the energy in the sites is called 'charge' and link variables are also called 'gauge fields' even if they are just a set of canonical variables along a one-dimensional lattice.

quantities or from 1 to $l-1$ for link quantities. At the ends of the chain, terms with $x < 1$ or $x > l$ are omitted.

There is one equation for each resonator with the first two terms on the right hand side expressing the LC resonator. Terms containing k_x are the interaction, where k_x has the units of an inverse voltage.

Like the SSH model the resonators have no dedicated capacitors but only the coupling capacitors. This eliminates the additional scale of a larger on-site capacitor. However, we will stay within the small coupling regime by choosing k_x small enough.

Intuitively the way the interaction is connected to the capacitors can be understood by looking at the small coupling behavior. It requires the interaction to be small, i. e. close to ground. Then the resonators oscillate mostly as if the capacitors were connected to ground, but a small jiggle is added by the device implementing the interaction.

The next step along the road towards a Hamiltonian is the Lagrange function. We first integrate the equations of motion to cast them in terms of the flux linkage:

$$\begin{aligned} I_x &= \frac{1}{L_x}\Phi_x + 2C_c\ddot{\Phi}_x - C_c\left(k_{x-1}\frac{\mathrm{d}}{\mathrm{d}t}\dot{\Phi}'_{x-1}\dot{\Phi}_{x-1} + k_x\frac{\mathrm{d}}{\mathrm{d}t}\dot{\Phi}'_x\dot{\Phi}_{x+1}\right) \\ I'_x &= \frac{1}{L'_x}\Phi'_x + 2C_c\ddot{\Phi}'_x - C_c k_x\frac{\mathrm{d}}{\mathrm{d}t}\dot{\Phi}_x\dot{\Phi}_{x+1}. \end{aligned} \tag{53}$$

These equations are reconcilable with the Euler-Lagrange equations and upon setting the external currents $I_x^{(\prime)}$ to zero we, obtain the Lagrange function

$$\mathcal{L}(\Phi,\dot{\Phi}) = \frac{1}{2}\sum_{x,x'}\left(C\dot{\Phi}_x^2 - \frac{1}{L_x}\Phi_x^2\right) - \sum_{x=1}^{L-1} C_c k_x\,\dot{\Phi}_x\dot{\Phi}'_x\dot{\Phi}_{x+1}. \tag{54}$$

The sum over (x, x') denotes a sum over the site and link quantities. The capacitance $C = 2C_c$ is the total on-site capacitance. While in the implemen-

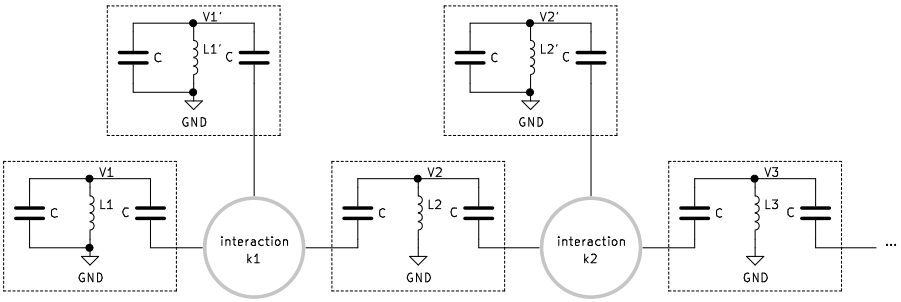

Figure 12: Simplified schematic of the U(1) model. Each box indicates one LC tank circuit associated to one complex variable (a_1, b_1, a_2, b_2, a_3, ...). The interaction is illustrated in the gray circles with only its current carrying outputs shown. Voltages $V_x^{(\prime)}$ are tapped at the non-grounded ports of the inductors. All capacitors have the same value C_c.

tation it is not separate from the coupling capacitors, it is given its own name, so that it becomes assessable what choosing a larger on-site capacitance would entail.

The conjugate momentum needed to transform to the Hamiltonian is

$$\begin{aligned} Q_x &= \frac{\partial \mathcal{L}}{\partial \dot{\Phi}_x} = C\dot{\Phi}_x - C_c k_x \dot{\Phi}_{x-1}\dot{\Phi}'_{x-1} - C_c k_x \dot{\Phi}'_x \dot{\Phi}_{x+1} \\ Q'_x &= \frac{\partial \mathcal{L}}{\partial \dot{\Phi}'_x} = C\dot{\Phi}'_x - C_c k_x \dot{\Phi}_x \dot{\Phi}_{x+1}, \end{aligned} \tag{55}$$

which is non-trivial to invert for $\dot{\Phi}(Q)$. We have addressed this problem for the SSH model and proceed here with the small coupling approximation. For the interaction to be much smaller than the free dynamics, the typical flux change, i. e. the typical voltage V_0, times k_x has to be much smaller than unity ($k_x V_0 \ll 1$). Then

$$\dot{\Phi}_x \approx \frac{1}{C} Q_x \quad \text{and} \quad \dot{\Phi}'_x \approx \frac{1}{C} Q'_x, \tag{56}$$

and the Legendre transformation of $\mathcal{L}$ evaluates to

$$H(\Phi, Q) = \frac{1}{2} \sum_{x,x'} \left(\frac{1}{L_x} \Phi_x^2 + \frac{1}{2C_c} Q_x^2 \right) + \sum_x \frac{k_x C_c}{C^3} Q_x Q'_x Q_{x+1}. \tag{57}$$

At this point we remove dimensions using quantities defined very similarly as before, only the time scale has to be adjusted for the tank circuits in the U(1) chain. Not all resonators have the same frequency and we more or less arbitrarily choose ω_0 as the uncoupled angular frequency averaged along all sites.

$$\begin{aligned} \bar{\Phi} &= \Phi/\Phi_0, \qquad \Phi_0 = V_0/\omega_0, \\ \bar{Q} &= Q/Q_0, \qquad Q_0 = C\,V_0. \end{aligned} \tag{58}$$

In the implementation, the typical voltage amplitude will be set by a power supply, which makes V_0 a very good choice for setting the system's scale. Upon factoring out $H_0 = Q_0^2/C$, the remaining terms in the Hamiltonian $\bar{H} = H/H_0$ become dimensionless:

$$\bar{H}(\bar{\Phi}, \bar{Q}) = \frac{1}{2} \sum_{x,x'} \left(\bar{\omega}_x^2 \bar{\Phi}_x^2 + \bar{Q}_x^2 \right) + \sum_x \frac{C_c}{C} \frac{V_0}{V_{\text{ref}}} \bar{Q}_x \bar{Q}'_x \bar{Q}_{x+1}, \tag{59}$$

where $\bar{\omega}_x = 1/(\omega_0 \sqrt{L_x\, C})$ is the dimensionless angular frequency of the uncoupled resonators. Remember that also the time becomes dimensionless by $t \to \tau = t\omega_0$ to have Hamilton's equations unchanged.

If in the running experiment the voltage amplitudes are close to V_0 for all resonators, all $\bar{Q}_x^{(\prime)}$ have the same magnitude, and according to the Hamiltonian, the magnitude of $\bar{\Phi}_x^{(\prime)}$ is proportional to its relative frequency.

The interaction term has a magnitude given by the ratio of typical voltage over the reference $V_{\text{ref}} = 1/k_x$. This voltage will show up as actual internal voltage reference later in the implementation details.

The explicit appearance of V_0 in the Hamiltonian is an effect of the non-linearity of the system: the dynamics are not independent of the scale anymore and lower voltages reduce the effective coupling strength.

It is time to introduce complex variables. The different resonance frequencies $\bar{\omega}_x$ have to be taken into account to form a variable change that rescales Hamilton's equations in the same way as was shown in equation (24) for the SSH model:

$$\begin{aligned} a_x &= \frac{1}{\sqrt{2\bar{\omega}_x}}(\bar{Q}_x + i\bar{\omega}_x\bar{\Phi}_x), \quad a_x^* = \frac{1}{\sqrt{2\bar{\omega}_x}}(\bar{Q}_x - i\bar{\omega}_x\bar{\Phi}_x), \\ b_x &= \frac{1}{\sqrt{2\bar{\omega}'_x}}(\bar{Q}'_x + i\bar{\omega}'_x\bar{\Phi}'_x), \quad b_x^* = \frac{1}{\sqrt{2\bar{\omega}'_x}}(\bar{Q}'_x - i\bar{\omega}'_x\bar{\Phi}'_x). \end{aligned} \tag{60}$$

This fulfills $\{a_x, a_y^*\}_{\Phi,Q} = i\delta_{xy}$ for site variables and the same for the link variables (b, b^*). We will use (z, z^*) to denote the full set of variables $((a, b), (a^*, b^*))$. The dimensionless Hamiltonian in complex variables is

$$\begin{aligned} H(z, z^*) = &\sum_{x=1}^{l} \bar{\omega}_x\, a_x^*\, a_x + \sum_{x=1}^{l-1} \bar{\omega}'_x\, b_x^*\, b_x \\ &+ \sum_{x=1}^{l-1} \Omega_x (a_x + a_x^*)(b_x + b_x^*)(a_{x+1} + a_{x+1}^*) \end{aligned} \tag{61}$$

with the details of the coupling strength written as

$$\Omega_x = \sqrt{\bar{\omega}_x \bar{\omega}'_x \bar{\omega}_{x+1}/2^3}\ \frac{C_c}{C}\frac{V_0}{V_{\text{ref}}}. \tag{62}$$

Using the solutions to the Hamiltonian without coupling, i. e. $\Omega_x = 0$, the transformation to the interaction picture $(z, z^*) \to (z', z^{*\prime})$ is

$$\begin{aligned} a_x \to a'_x &= e^{-i\bar{\omega}_x \tau}\, a_x \\ b_x \to b'_x &= e^{-i\bar{\omega}'_x \tau}\, b_x, \end{aligned} \tag{63}$$

and the interaction term of the Hamiltonian can be expanded to twelve terms oscillating on various timescales. Which of these terms we retain after separating the timescales depends on the choice of tuning $\bar{\omega}_x^{(\prime)}$. For example the simplest choice would be a ladder-like structure with $\bar{\omega}_x + \bar{\omega}'_x = \bar{\omega}_{x+1}$. Then site frequencies are increasing in one direction along the chain and the approximated Hamiltonian would be

$$H(z', z^{*\prime}) = \sum_{x=1}^{l-1} \Omega_x (a_x^{*\prime} b_x^{*\prime} a'_{x+1} + a_{x+1}^{*\prime} b'_x a'_x). \tag{64}$$

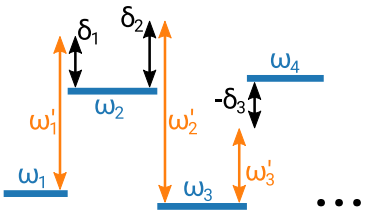

Figure 13: Staggering of frequencies with exaggerated detuning.

However the ever increasing site frequencies along the chain would pose an experimental problem, because our experiment is limited in available resonance frequencies from below and above within one order of magnitude. With a staggered configuration, where site frequencies are alternating as illustrated in figure 13, it is possible to build arbitrarily long chains within this interval of available frequencies. The approximation also allows a detuning δ_x that is small compared to all $\bar{\omega}_x$, so that for the staggered tuning condition we write

$$\begin{aligned} \bar{\omega}_x + \bar{\omega}'_x &= \bar{\omega}_{x+1} + \delta_x \quad \text{for } x \text{ odd}, \\ \bar{\omega}_x - \bar{\omega}'_x &= \bar{\omega}_{x+1} - \delta_x \quad \text{for } x \text{ even}. \end{aligned} \tag{65}$$

The staggering is also reflected in the remaining terms after the approximation, which are

$$H(z', z^{*\prime}) = \sum_{x=1}^{l-1} \Omega_x \begin{cases} e^{-i\delta_x \tau}\, a_x^{*\prime} b_x^{*\prime} a'_{x+1} + \text{H. c.} & \text{for } x \text{ odd}, \\ e^{+i\delta_x \tau}\, a_x^{*\prime} b'_x a'_{x+1} + \text{H. c.} & \text{for } x \text{ even}. \end{cases} \tag{66}$$

There are now the time-dependent prefactors, which we can remove by changing to yet another frame, which follows the detuning δ_x. Upon executing

$$\begin{aligned} a'_x \to a_x &= e^{-i(-1)^x \Delta_x \tau/2}\, a'_x, \\ b'_x \to b_x &= b'_x \quad \text{(unchanged)}, \end{aligned} \tag{67}$$

and requiring the condition $\Delta_{x+1} = 2\delta_x - \Delta_x$, $\Delta_1 = \delta_1$, then the oscillating prefactors vanish. The simplest allowed configuration is all having the same value, $\Delta = \Delta_x = \delta_x$. With the new variables, the Hamiltonian has become

$$\begin{aligned} H(z, z^*) = -\sum_{x=1}^{l} (-1)^x \frac{\Delta_x}{2} a_x^* a_x + \sum_{x \text{ odd}} \Omega_x (a_x^* b_x^* a_{x+1} + \text{H. c.}) \\ + \sum_{x \text{ even}} \Omega_x (a_x^* b_x a_{x+1} + \text{H. c.}). \end{aligned} \tag{68}$$

While some terms are non-quadratic, we may still insist on writing it as matrix $H(z, z^*) = a^\dagger \hat{H}(b, b^*) a$ by allowing the matrix to depend on the link variable:

$$H(z, z^*) = a^\dagger \begin{pmatrix} \frac{\Delta_1}{2} & \Omega_1 b_1^* & & \\ \Omega_1 b_1 & -\frac{\Delta_2}{2} & \Omega_2 b_2 & \\ & \Omega_2 b_2^* & \frac{\Delta_3}{2} & \Omega_3 b_3^* \\ & & \Omega_3 b_3 & -\frac{\Delta_4}{2} \\ & & & \ddots \end{pmatrix} a. \tag{69}$$

Written this way the resemblance to the SSH Hamiltonian in equation (29) is large enough that one would expect solutions to be similar to the SSH model's solutions in some cases.

3.2 CONSERVED QUANTITIES

The Hamiltonian with staggered site frequencies is symmetric under the following local U(1) transformation parameterized by θ_x:

$$\begin{aligned} a_x &\to e^{i\theta_x}\, a_x \\ b_x &\to e^{i(-1)^x(\theta_x - \theta_{x+1})}\, b_x. \end{aligned} \tag{70}$$

As it is a continuous symmetry, a conserved quantity should exist for each θ_x, i. e. at each site. Note that each solution to the equations of motion provides a constant of motion, but in general with an explicit time dependence. Only quantities, that are conserved during time evolution and have no explicit time dependence are called conserved quantities.

In the context of classical mechanics we can use Poisson brackets to build something like generators and charges similar to quantum mechanics [21]. For the symmetries of the SSH model we already saw the time evolution for any quantity $G(z, z^*)$ derived from the canonical variables:

$$-i\frac{\mathrm{d}G}{\mathrm{d}t} = \{G, H\} + \partial_t H. \tag{71}$$

As the Hamiltonian 'generates' the time evolution of the system, we can also use other quantities to generate infinitesimal canonical transformations[2] via

$$-i\,\partial z = \mathrm{d}\theta_x\, \{z, G_x\} \tag{72}$$

where ∂z is the infinitesimal change for the parameter change $\mathrm{d}\theta_x$.

Let us take a look at phase transformations at one site x. It affects the site itself and the two adjacent links. The infinitesimal change is given by the linear term of the exponential expansion:

$$\begin{aligned} \partial b_{x-1} &= -i(-1)^{x-1}\, \mathrm{d}\theta_x\, b_{x-1} \\ \partial a_x &= i\, \mathrm{d}\theta_x\, a_x \\ \partial b_x &= i(-1)^x\, \mathrm{d}\theta_x\, b_x. \end{aligned} \tag{73}$$

When inserting into eq. (72) and integrating, we find the generator

$$G_x = a_x^*\, a_x + (-1)^x\, (b_{x-1}^*\, b_{x-1} + b_x^*\, b_x) + \text{const.} \tag{74}$$

2 The term 'generator' is not to be confused with the *generating functional* of classical mechanics.

At the boundaries, the terms of links outside the chain are zero. G_x not only generates the local phase transformation at x, but is also conserved according to eq. (71). The dimensionful conserved quantity is

$$H_0\, G_x = \frac{\omega_0}{\omega_x} E_x + (-1)^x \left(\frac{\omega_0}{\omega'_{x-1}} E'_{x-1} + \frac{\omega_0}{\omega'_x} E'_x \right) + \text{const.} \tag{75}$$

with oscillator energy $E = \Phi^2/2L + Q^2/2C$. Here the interpretation of the conservation law as Gauss's law becomes apparent: When energy moves from one site to the next it is accompanied by a corresponding change of energy in the link in between. In analogy to quantum mechanics we will call G_x the charge of Gauss's law.

We now also see, that the model does not support *confinement*. Confinement means that the energy of the field connecting two charges increases with the distance of the charges [28]. For one, there is no $b^* b$ term left in the Hamiltonian. More explicitly, when moving energy δE from an odd site to the next odd site, e. g. $x = 1$ to $x = 3$, the change is

$$\begin{aligned} E_1 &\to E_1 - \delta E \\ E'_1 &\to E'_1 - \delta E \\ E_2 &\to E_2 \\ E'_2 &\to E'_2 + \delta E \\ E_3 &\to E_3 + \delta E \end{aligned} \tag{76}$$

and the energy $E'_1 + E'_2$ of the links in between stays the same. Adding an appropriate term quadratic in the link energy to the Hamiltonian could introduce confinement.

Apart from the set of Gauss laws G_x, the Hamiltonian has total energy conservation, because the it is independent of time. Furthermore, connected to the global U(1) symmetry $a_x \to e^{i\vartheta} a_x$, the generator

$$G_{\text{tot}} = \sum_x a_x^* a_x \tag{77}$$

is conserved. In the style of quantum mechanics we will call G_{tot} the total number.

The symmetry group U(1) has discrete subgroups, in particular $\mathbb{Z}_2$. While $\mathbb{Z}_2$ gauge theories are relevant in quantum mechanics and are investigated in ultracold atom experiments [29], there seems to be no notable impact in classical mechanics, as already mentioned for the SSH model. Lutzky [30] writes, that conserved quantities can only be found, if the discrete symmetry transformation connects two inequivalent Lagrangians, i. e. two Lagrangians which differ by more than a total time derivative yet lead to the same equations of motion.

3.3 TWO-LEVEL SYSTEM

Before turning to solutions of the whole system, we can simplify the problem by removing the links from the set of dynamical variables. As mentioned the introduction, the gauge fields are then said to be static as opposed to dynamic. Most importantly, the Hamiltonian becomes linear.

We will limit ourselves to only two sites with frequencies $\bar{\omega}_{1,2}$ where $\bar{\omega}_2 > \bar{\omega}_1$. Driving the link externally means replacing the variable b_1 by the dimensionless expression

$$b_1(\tau) = b\, e^{i\bar{\omega}_1' \tau}. \tag{78}$$

The tuning condition (65) still defines the detuning $\delta = \Delta$ and the Hamiltonian of eq. (68) becomes

$$H(\tilde{a}, \tilde{a}^*) = \tilde{a}^\dagger \hat{H} \tilde{a} = \tilde{a}^\dagger \begin{pmatrix} \frac{\Delta}{2} & \Omega b^* \\ \Omega b & -\frac{\Delta}{2} \end{pmatrix} \tilde{a} \tag{79}$$

with the tilde indicating the rotating frame. This expression is formally equivalent to the prototypical two-level system of quantum mechanics! The system's time evolution is decoupled into normal modes using the eigendecomposition of the Hermitian matrix $\hat{H} = U^\dagger \Lambda U$, where Λ is a diagonal matrix holding eigenvalues $\lambda_{1,2} = \pm\frac{1}{2}\mu$ of $\hat{H}$ and U is the corresponding unitary basis transformation.

$$\Lambda = \begin{pmatrix} \frac{1}{2}\mu & 0 \\ 0 & -\frac{1}{2}\mu \end{pmatrix}, \quad U = \begin{pmatrix} e^{i\beta} \cos\frac{\vartheta}{2} & \sin\frac{\vartheta}{2} \\ -e^{i\beta} \sin\frac{\vartheta}{2} & \cos\frac{\vartheta}{2} \end{pmatrix}, \tag{80}$$

$$\text{where} \quad \mu = \sqrt{\Delta^2 + 4\Omega^2 |b|^2}, \quad \tan\vartheta = \frac{2\Omega|b|}{\Delta}, \quad \beta = \arg b.$$

With initial condition $\tilde{a} = a^{\text{in}}$ at $\tau = 0$, the full solution is

$$\tilde{a}(\tau) = e^{i\hat{H}\tau}\, a^{\text{in}} = U^\dagger\, e^{i\Lambda\tau}\, U\, a^{\text{in}}. \tag{81}$$

To match the measurements, we should also undo the rotating frames defined in (63) and (67) by using $\tilde{a} \to a = T(\tau)\tilde{a}$ with

$$T(\tau) = \begin{pmatrix} e^{i(\bar{\omega}_1 - \Delta/2)\tau} & 0 \\ 0 & e^{i(\bar{\omega}_2 + \Delta/2)\tau} \end{pmatrix}. \tag{82}$$

The solution may be written in a way that clearly shows the two frequency components for each site:

$$a(\tau) = \begin{pmatrix} c_{11}e^{i(\bar{\omega}_1+(\mu-\Delta)/2)\tau} + c_{12}e^{i(\bar{\omega}_1-(\mu+\Delta)/2)\tau} \\ c_{21}e^{i(\bar{\omega}_2+(\mu+\Delta)/2)\tau} + c_{22}e^{i(\bar{\omega}_2-(\mu-\Delta)/2)\tau} \end{pmatrix}, \qquad c_{ij} = U^\dagger_{ij} \sum_k U_{jk} a^{\text{in}}_k. \tag{83}$$

In the spectrum (the temporal Fourier transformation of the signal), the two frequency components show up, and by scanning the driving frequency of the link, the detuning Δ can be set. Figure 14 shows their behavior, which is almost the same as for the usual two-level system, but tilted, because the driven Hamiltonian (79) is formulated in a rotating frame depending on Δ.

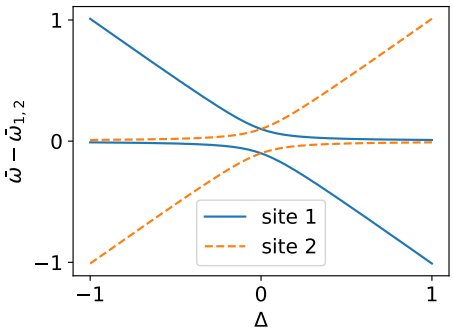

Figure 14: Level repulsion for driven two-level model, centered around undressed site frequencies $\bar{\omega}_{1,2}$.

In the limits of small coupling Ω and small detuning Δ, the frequency components are close together at each site, i. e. $\mu \pm \Delta$ is small compared to $\bar{\omega}_{1,2}$. This results in a beat when plotting the signal over time. A beat is an oscillation of the signal envelope $A = |a|$. So for site x the envelope squared is

$$A^2_x(\tau) = |a_x(\tau)|^2 = |c_{x1}|^2 + |c_{x2}|^2 + 2\,|c^*_{x2}\,c_{x1}|\,\sin(\mu\tau + \alpha_x) \qquad \text{where} \quad \alpha_x = \operatorname{atan2}(\operatorname{Re} c^*_{x2}c_{x1}, -\operatorname{Im} c^*_{x2}c_{x1}). \tag{84}$$

The beat has a frequency of μ, which specifies the distance of the levels. The phase α is specified using the atan2 function for a correct result in the interval $[-\pi, \pi]$ instead of $[-\frac{\pi}{2}, \frac{\pi}{2}]$. The phase has a non-trivial dependence on θ, β and a^{in}, which in the case of $a^{\text{in}}_1 = a^{\text{in}}_2$ simplifies to

$$\begin{aligned} \alpha_1 &= \operatorname{atan2}(-\sin 2\theta\,\cos\theta\,\cos\beta,\ \sin 2\theta\,\sin\beta) \\ \alpha_2 &= \operatorname{atan2}(\sin 2\theta\,\cos\theta\,\cos\beta,\ -\sin 2\theta\,\sin\beta). \end{aligned} \tag{85}$$

The contrast of the signal, which we may define similar to the Michelson contrast using minimal and maximal values of the squared envelope, is

$$K_x = \frac{A^2_{\max} - A^2_{\min}}{A^2_{\max} + A^2_{\min}} = \frac{2|c^*_{x2}\,c_{x1}|}{|c_{x1}|^2 + |c_{x2}|^2}. \tag{86}$$

All of these features and values—level repulsion, beat frequency μ, phase α, and contrast—are used later to compare measurements to expectations.

3.4 PERTURBATIVE APPROACHES

Unlike the two-level system, the full U(1) model is non-linear and a typical approach to gain ground is by perturbation theory, but it turns out that the classical variant is less intuitive for the modern physics student. For this reason, this section is kept short and presents only outlines of approaches.

The first approach is to expand all variables in terms of the coupling Ω and apply perturbation theory here. Let us split the Hamiltonian (68) into

$$H = H_0 + \Omega\, H_{\text{int}} \tag{87}$$

with the simplifying assumption that all Ω_x are the same Ω. Each order n of the perturbation theory is a solution to the linear differential equations

$$\begin{aligned} -i\frac{\mathrm{d}}{\mathrm{d}\tau}a_x^{(n)} &= \left.\frac{\partial H}{\partial a_x^*}\right|_n + \left.\frac{\partial H_{\text{int}}}{\partial a_x^*}\right|_{n-1} \\ -i\frac{\mathrm{d}}{\mathrm{d}\tau}b_x^{(n)} &= \left.\frac{\partial H_{\text{int}}}{\partial b_x^*}\right|_{n-1}. \end{aligned} \tag{88}$$

The zeroth order contains no interaction term and the equations describe independent harmonic oscillators on the sites. In the rotating frame the links are constant at zeroth order! Higher orders are oscillators with the interaction term acting as external force. When looking at the frequency spectrum of the solution, higher orders add side bands to the main peak of the zeroth order solution, but cannot shift it. There are no solutions where modes hybridize like they do for example in the two-level system, but the experiments we will see later show exactly that.

Remembering the SSH model, the measured frequency spectrum reflected the band structure of the Hamiltonian. In the hope of estimating something like a density of states, one might try to formulate propagators from Green's functions for the equations above. Unfortunately their usefulness is limited without a statistical interpretation [31], which is outside the scope of this thesis.

Another approach may be motivated by the quantum version of the U(1) model, where we interpret the variables to be creation and annihilation operators. Each site or link has an occupation number that counts excitations, which can be moved around by the interaction. The total number conservation and local Gauss laws restrict the movement of the excitations. The basis of states (denoted by occupation numbers) has a size depending on the number of excitations in the system, which is bounded by total number conservation. The Hamiltonian can be written as a matrix that is as large as its basis, i. e. scaling with the number of excitations. Standard perturbation theory known from quantum mechanics may be applied to this Hamiltonian.

All of this relies on the fact that the operators and in turn the excitations are quantized, but our classical variables are continuous.

One might hope, that the restrictions imposed by the local Gauss laws are strong enough to make the classical system analytically solvable, but calculations in the context of this thesis do not support that. A chain of l sites has two degrees of freedom per site and two per link, totaling to $4l - 2$. There is one Gauss law per site, fixing l degrees of freedom, plus total number conservation. So for example, this is not enough for the link variables to be completely determined from the configuration of the sites. For some quantum systems with U(1) gauge symmetry it is possible to separate degrees of freedom of the matter and the gauge field [32, 33]. But again, this could not be achieved here.

The last approach we want to consider, is to reformulate the system using a spatial Fourier transformation. For the SSH model this provided the band structure by block diagonalizing the Hamiltonian. We introduce again the indexing notation $(n, A/B)$ with sublattices A and B in $N = l/2$ unit cells, as was used for the SSH model, and impose periodic boundary conditions. The Fourier transformation along unit cells was defined in eq. (33). Simplifying with $\Delta_x = \Delta$ and $\Omega_x = \Omega$ for all x allows us to write the Hamiltonian (68) in spatial modes k:

$$\begin{aligned} H(\tilde{z}, \tilde{z}^*) =& \frac{-\Delta}{2} \sum_k \left(\tilde{a}^*_{kA}\, \tilde{a}_{kA} - \tilde{a}^*_{kB}\, \tilde{a}_{kB}\right) \\ &+ \frac{\Omega}{\sqrt{N}} \sum_k \sum_{k'} \left(\tilde{a}^*_{kA}\, \tilde{\rho}^*_{k'-k}\, \tilde{a}_{k'B} + \tilde{a}^*_{kB}\, \tilde{\rho}_{k-k'}\, \tilde{a}_{k'A}\right) \end{aligned} \tag{89}$$

for N unit cells. The links are encapsulated in

$$\tilde{\rho}^*_{k'-k} = \tilde{b}^*_{k'-k,A} + \tilde{b}^*_{k'-k,B}\, e^{ik}, \tag{90}$$

which resembles the interaction term in eq. (35) but with a dependence on spatial modes. The structure of the Hamiltonian shows, that the zero mode of the links (i. e. $k' - k = 0$) couples the same modes of the sublattices A and B, and higher modes of the links couple different modes of the sublattices. In the case where only the zero mode of the link was significant, the Hamiltonian reduces to the SSH model. This insight may be interesting, but does not help with tangible predictions for measurements.

3.5 NUMERICAL SIMULATIONS

To have any kind of comparison, simulations have to serve for testing the circuit and whether it is matching the desired Hamiltonian. As lined out in the introduction, we want to verify to things: The implementation should meet the idealized equations of motion according to Kirchhoff's current law (KCL).

Secondly we should confirm, that the approximations, which connect the KCL with the U(1) Hamiltonian, are justified, i. e. do not undermine the U(1) symmetry. For this reason we run two different simulations: one for the idealized circuit according to the KCL and the other for the Hamiltonian formulation.

The equations of motion due to Kirchhoff's current law are given in eq. (52). Because the integrators from the SciPy library expect a system of first order differential equations, we rewrite them with the substituting $\dot{\Phi} = V$:

$$\begin{aligned} I_x &= \frac{1}{L_x}\Phi_x + 2C_c\dot{V}_x - C_c\left(k_{x-1}\left(V'_{x-1}\dot{V}_{x-1} + \dot{V}'_{x-1}V_{x-1}\right) + k_x\left(V'_x\dot{V}_{x+1} + \dot{V}'_xV_{x+1}\right)\right) \\ I'_x &= \frac{1}{L'_x}\Phi'_x + 2C_c\dot{V}'_x - C_ck_x\left(V_x\dot{V}_{x+1} + \dot{V}_xV_{x+1}\right). \end{aligned} \tag{91}$$

At the ends of the chain, terms with $x < 1$ or $x > l$ are omitted. Using a matrix $M(V)$ we can write

$$I_x - \Phi_x / L_x = M_{xy}(V)\,\dot{V}_y. \tag{92}$$

Solving numerically for $\dot{V}$ by inverting M yields $\dot{V}(\Phi, V)$, which together with $\dot{\Phi} = V$ forms the full set of differential equations in SI units. Remember that I_x captures external currents / driving.

In accordance with experiments, the external currents I_x are chosen to be non-zero only at the first site, where it is driven by the harmonic signal

$$I_1 = I_{\mathrm{drv}}\cos(2\pi\, f_{\mathrm{drv}}\, t). \tag{93}$$

The parameters of the simulation are C_c, $L_x^{(\prime)}$, k_x, I_{drv} and f_{drv}. Also conforming to the experiment setup, we have $C_c = 10\,\mathrm{nF}$ and $k_x = 1/V_{\mathrm{ref}} = 1/10\,\mathrm{V}$. Using

$$f_x^{(\prime)} = \frac{\omega_x^{(\prime)}}{2\pi} = \frac{1}{2\pi\sqrt{2C_c\,L_x^{(\prime)}}} \tag{94}$$

the remaining parameters can be specified by $f_x^{(\prime)}$, I_{drv} and f_{drv}. Initial conditions are chosen such that all resonators start with an initial amplitude of 1 V at the phase where all energy is stored in the inductors. The numerical integration is carried out using SciPy's *Livermore Solver for Ordinary Differential Equations*, `scipy.integrate.odeint`, whereby we obtain $\Phi(t)$ and $V(t)$.

On the other hand we have the Hamiltonian (68) in the rotating frame. Hamilton's equations evaluate to

$$\begin{aligned}
\dot{a}_x &= i\frac{\partial H}{\partial a^*} = -i\frac{\Delta_x}{2}(-1)^x a_x + i \begin{cases} \Omega_{x-1} b^*_{x-1} a_{x-1} + \Omega_x b^*_x a_{x+1} & \text{for } x \text{ odd,} \\ \Omega_{x-1} b_{x-1} a_{x-1} + \Omega_x b_x a_{x+1} & \text{for } x \text{ even,} \end{cases} \\
\dot{b}_x &= i\frac{\partial H}{\partial a^*} = i\Omega_x \begin{cases} a^*_x a_{x+1} & \text{for } x \text{ odd,} \\ a_x a^*_{x+1} & \text{for } x \text{ even.} \end{cases}
\end{aligned} \tag{95}$$

At the ends of the chain, terms with $x < 1$ or $x > l$ are omitted. Since `scipy.integrate.odeint` supports only real variables, the differential equations are wrapped in a function that splits them into real and imaginary parts.

Hamilton's equations are homogeneous without external currents, but we can introduce them by adding an inhomogeneous term. Given the external current from eq. (93), the dimensionless variant in the rotating frame is

$$\bar{I}_1 = \sqrt{\frac{L_1}{2\bar{\omega}_1 C}}\,\frac{1}{V_0}\, I_{\text{drv}}\, \cos\!\left(\left(f_{\text{drv}}/f_0 - \bar{\omega}_1 + \tfrac{\Delta_1}{2}\right)\tau\right) \tag{96}$$

with $f_0 = \omega_0/2\pi$. To give it the same meaning as the I_x in eq. (91), the term $-i\bar{I}_x$ needs to be added to the right-hand side of eq. (95).

Parameters of this simulation are Δ_x, Ω_x, I_{drv}, and f_{drv}. While results are in dimensionless variables, they are converted to their dimensionful equivalents for better comparison between the two types of simulations and the same initial values are chosen.

In figure 15 the two representative simulations are compared. The parameters are chosen to be $f_1 = 30\,\text{kHz}$, $f_2 = 90\,\text{kHz}$, and $f_3 = 30\,\text{kHz}$ for the sites. The first link is varied between $f_1' = 57\,\text{kHz}$ to $63\,\text{kHz}$. This results in a detuning of $f_{\delta 1}$ between $-3\,\text{kHz}$ to $3\,\text{kHz}$, which is the independent variable on the abscissa of the diagrams. The numerical integration is run for each value of $f_{\delta 1}$. The second link has zero detuning with $f_2' = 60\,\text{kHz}$. Since already a lot of features are present in the result of this setup, the driving is set to zero. In the dimensionless simulation of Hamilton's equations, these configurations corresponds to $\Delta_{1,2}$ having a range of ± 0.05. The coupling strength depends on the resonance frequencies and changes slightly between $\Omega = 0.015$ to 0.016 depending on the detuning. The choice of these parameters is more or less arbitrary but motivated by the setup of the experiment.

The results for the two simulations in figure 15 look very similar, but are not exactly the same. With the same amount of calculations, the Hamiltonian simulation reaches a higher resolution, because it runs in the rotating frame, which allows longer integration times, because fast dynamics are omitted.

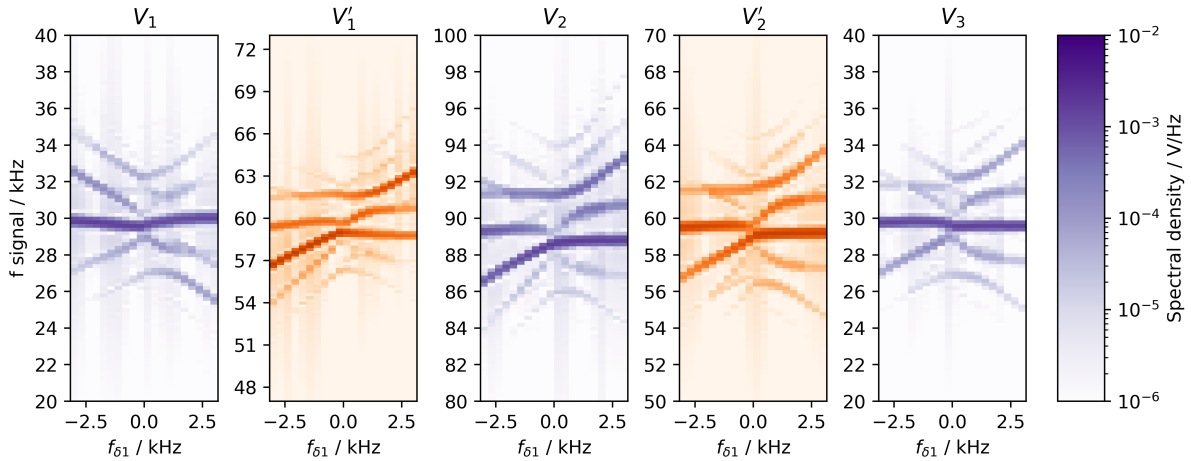

(a) Simulating Kirchhoff's current law.

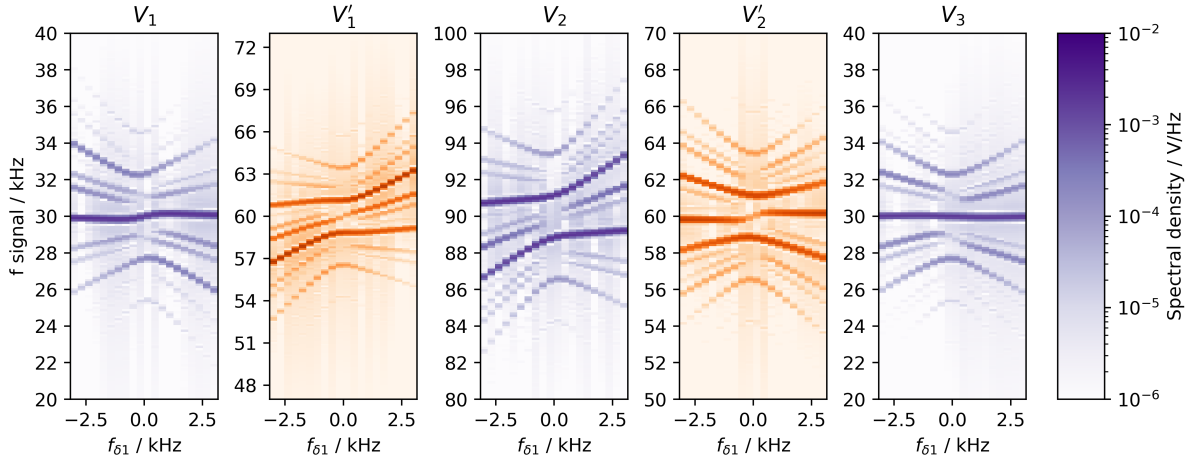

(b) Simulating the Hamiltonian formulation.

Figure 15: Measured and simulated spectra for set (1) with $I_{\mathrm{drv}} = 0.3\,\mathrm{mA}$. Links have an orange color map as opposed to the blue one for the sites. The overall structure of the two types of simulations is similar, but there are significant differences.

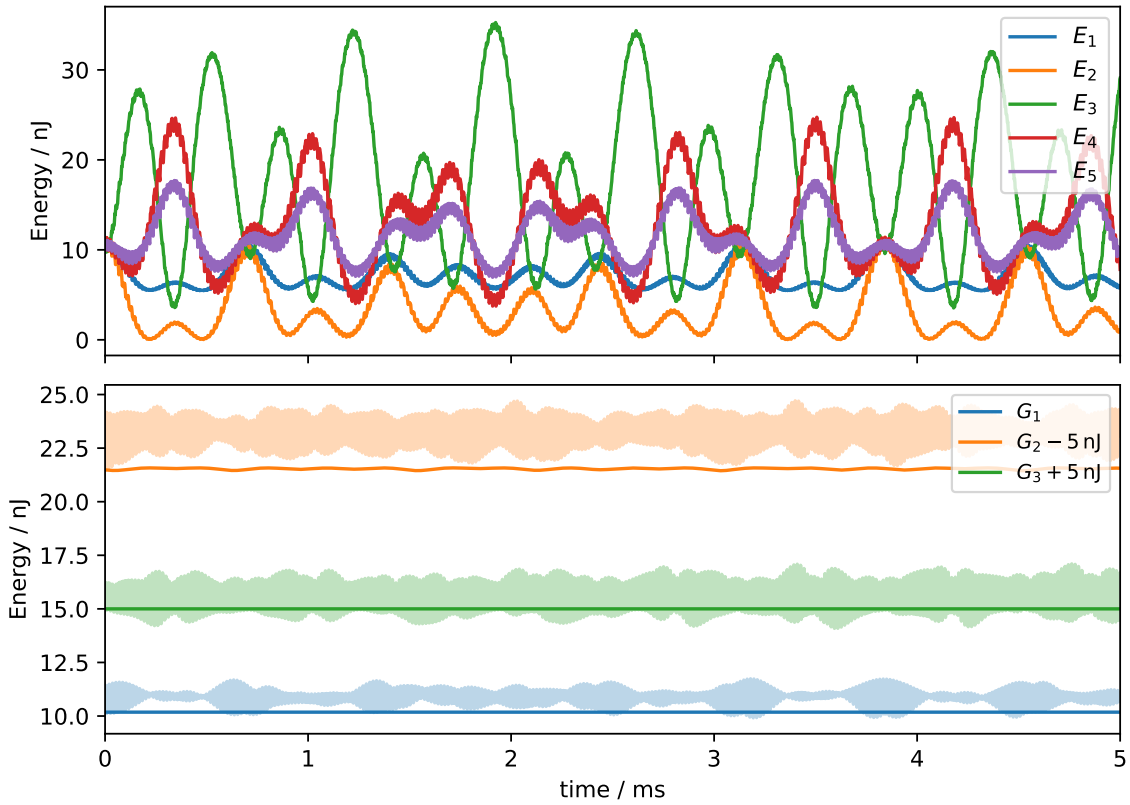

Figure 16: Comparison of conserved quantities in simulations with same setup as in figure 15 at $f_\delta = 1.1\,\mathrm{kHz}$. Top: energies in resonators over time from simulating the KCL; bottom: charges of Gauss's law with drawn through lines for simulation of Hamiltonian and shaded region for simulation of KCL. The simulation of the KCL shows a significant violation, which is related to the small coupling and rotating wave approximations. Arbitrary offsets of $\pm 5\,\mathrm{nJ}$ are added to G_x for optimal presentation.

Apart from the numerical resolution, the difference between the results brings out the effect of approximations done in the derivation of the Hamiltonian. With the U(1) symmetry being the key property of the circuit, the local conservation laws from eqs. (74) and (75) should be compared.

The energies of the resonators and the associated charges G_x—implicitly using $H_0 G_x$ for dimensions—are shown in figure 16. The Hamiltonian simulation obeys Gauss's laws within numerical precision. The simulation of the KCL however shows significant violations. The range of the various G_x is roughly 2 nJ while the dynamics in the energies have a range averaging to about 20 nJ. Loosely speaking, the violation of Gauss's law is one tenth of the range of the dynamics. We will come back to the measure of violation later with measurements at hand.

Note how the fact of the spectra having no other than a few well defined peaks, i. e. the system having a periodic behavior, indicates that there are steady state solutions, even if they could not be identified in the previous section about perturbation theory.

4

U(1) MODEL: EXPERIMENT

In this chapter we discuss the actual circuit implementation and its electrical intricacies. The circuit is broken down into U(1) blocks of which many identical instances can form a chain. Each one of these blocks contains a link and two sites connected by the coupling in between. Sites and links are LC resonators and are equipped with initializers to generate step functions for initial conditions. They are also augmented to oscillators by feedback circuits, which counteract dissipation in the hope to protect the expected conservation laws. Upon connecting blocks to a chain, every two adjacent sites are joined to a single site in the bulk of the chain. Figure 17 illustrates the different parts of the circuit and how two circuit boards, each containing one U(1) block, are connected to form a chain.

The next section contains detailed schematics and explanations for each subcircuit appearing in figure 17. After going through the schematics, the procedure for tuning the circuit is presented. Then follow measurements for the two-level system (two sites connected by an externally driven link) and a full U(1) model with three sites and two links.

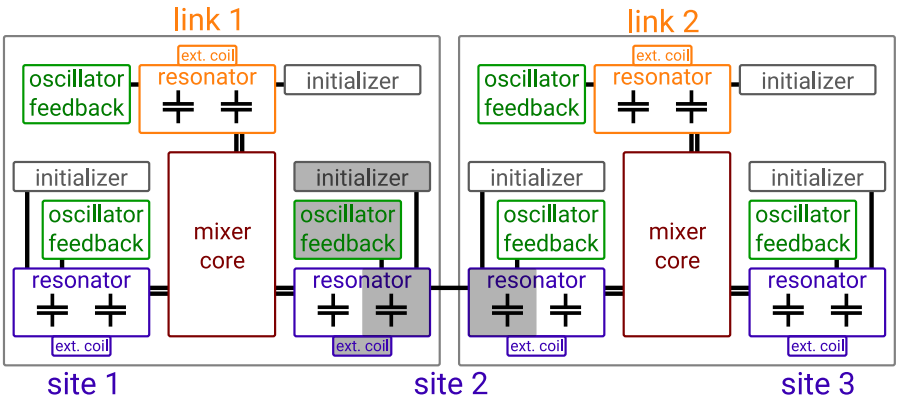

Figure 17: Outline of circuit parts across two boards. When connecting the circuit boards the grayed out parts are disconnected to merge the resonators into one site.

4.1 CIRCUIT DESIGN

4.1.1 *Mixer core*

The mixer core, enabling the U(1) interaction, is at the heart of the circuit. We have seen in eq. (54) that the interaction term ($\dot{\Phi}_x \dot{\Phi}'_x \dot{\Phi}_{x+1}$ in the Lagrange function) is symmetric under exchange of variables, so it needs to be realized by a device with an analogous exchange symmetry of its in- and output ports. In the equations of motion (52) the interaction is formed by the multiplication of two voltages, here implemented via an analog mixer, and a second derivative, which typically enters at capacitive electrical elements.

Voltage multipliers, commonly called mixers, have a multitude of applications in signal processing, i. a. mixers for signal modulation. The AD633 integrated circuit chosen for this design works within a voltage range of $\pm 12\,\mathrm{V}$ for in- and outputs and a bandwidth of 1 MHz [34]. Its transfer function is

$$W = \frac{(X_1 - X_2)(Y_1 - Y_2)}{10\,\mathrm{V}} + Z, \tag{97}$$

where $X_{1,2}$ and $Y_{1,2}$ are high impedance differential inputs, W is the multiplier output, and Z is an optional input to offset W. Following the data sheet, an adjustable voltage divider to control feedback from W to Z can adjust the internal reference voltage of 10 V to any V_{ref} between 10 V to about 1 V. See figure 18 for the schematic of the three multipliers and the feedback network.

For one multiplier, the inputs X_2 and Y_2 are grounded. The inputs X_1 and Y_1 are connected to two resonators (which have voltages V_i and V_j), and the output W connects to the coupling capacitor C_c of another resonator (voltage V_m). Since the inputs have high impedance, there is no contribution to Kirchhoff's current law of the input nodes. Solely the output node has the contribution

$$\dot{I}_m = C_c \frac{\mathrm{d}^2}{\mathrm{d}t^2}(V_m - W) = C_c \ddot{V}_m - \frac{C_c}{V_{\mathrm{ref}}} \frac{\mathrm{d}^2}{\mathrm{d}t^2} V_i V_j, \tag{98}$$

with the capacitance expressed as second derivative on the voltage difference across it. One side is the resonator V_m and the other the multiplier W.

Because the coupling between the resonators has to be symmetric, the same setup is repeated for the other two even permutations of nodes i, j, and m. Therefore one interaction term in the Lagrangian is implemented by three mixers. The proportionality $k = 1/V_{\mathrm{ref}}$ of the equations of motion turns out to be the multiplier's internal voltage reference, or its scaled version respectively.

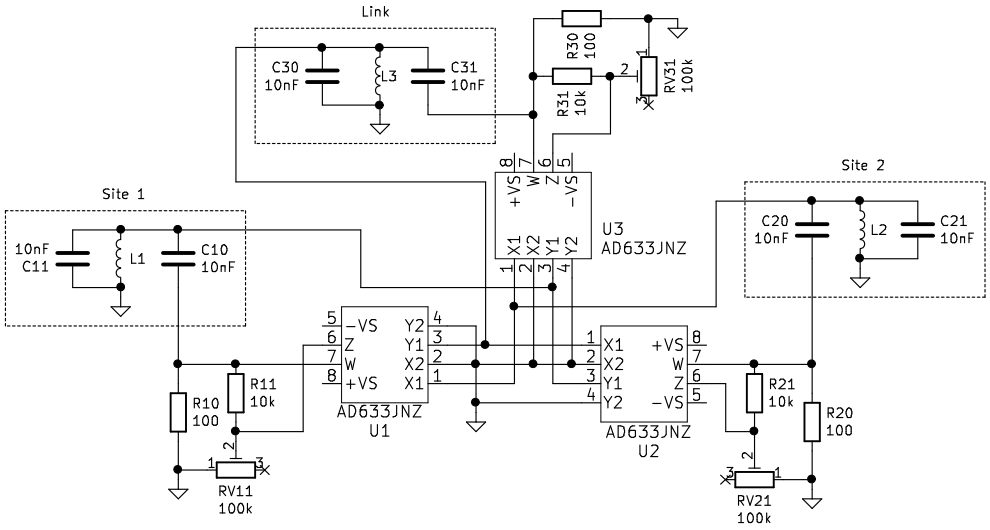

Figure 18: Schematic of one mixer core and the connections to the resonators. Each multiplier $\mathtt{U}_{1,2,3}$ has a feedback network of $\mathtt{R}_{?1}$ and potentiometer $\mathtt{RV}_{?1}$. Power connections $\pm\mathtt{VS}= V_{\pm}$ are omitted. This schematic is simplified, full schematic on page 80.

One important characteristic of the multipliers is their bandwidth,[1] which limits the overall circuit frequency. Capacitive loading of the IC output—as done in this design by the coupling capacitor—reduces the bandwidth and was a major obstacle in the early design stages (see figure 4 in ref. [34] for frequency response with various capacitive loads).

In a nutshell, the AD633 has an output buffer (a unity gain amplifier) to provide a low impedance output. The buffer is using negative feedback to follow it's input voltage but has a non-zero output resistance. When significant currents are drawn, the voltage drop over the output resistance affects the feedback loop. Capacitive loads effectively delay the voltage signal at the output and with it the feedback signal. In the extreme case, if the delay exceeds more than 180° at some frequency, the feedback becomes positive and the circuit begins to oscillate [35, 36]. Already before that happens there is an appreciable phase shift and drop in output amplitude that we also have to avoid to faithfully simulate the theory.

Early designs were running at frequencies between 200 kHz to 600 kHz which was far beyond the bandwidth with the capacitive load presented by the sites. The attempt to isolate the load from the multiplier by a BJT push-pull output stage [37] allowed a stable circuit but couldn't remedy the phase shift. This necessitated moving to frequencies below 100 kHz requiring also non-standard coils.

1 Frequency at which the output amplitude is attenuated to −3 dB compared to its low frequency limit.

A second way to mitigate the effects of the capacitive load, is to shift it away from being purely capacitive by adding a resistive component. For this reason the R?0=100 Ω resistors are included in the schematic.[2]

4.1.2 *Resonators*

Resonators with high quality factors have sharp frequency responses and low dissipation, which is desirable for our circuit. High quality factors for RF resonators are commonly achieved using air coils [38]. For this circuit toilet paper rolls, which lend themselves to tinkering, allowed fast prototyping and customization. Manufactured inductances range from 0.1 mH to 2 mH and could be estimated during design with this approximate formula from ref. [39]:

$$L = 0.001 \frac{N^2 r^2}{288 r + 254 l} \frac{\mathrm{H}}{\mathrm{m}} \tag{99}$$

for single layer coils, where N is the number of windings, r the coil radius and l the coil length. Achieved quality factors are listed in table 5 in appendix B.2.

To run the circuit at various detunings, we wish to tune the resonators. To this end, some inductors are customized to function as *variometers*: Secondary windings are mounted inside the coil on a rotating ring and are connected in series with the primary windings. If the coils are aligned, the inductance is maximal and if they are anti-aligned, the inductance is minimal. The typical variation is in the order of 20 %, corresponding to a range of about 10 kHz. A picture of a coil is shown in figure 19.

In a resonator the counterpart of the inductor is the capacitor. For the SSH circuit polyester film capacitors were used, but for the U(1) circuit capacitors with polypropylene dielectric were chosen. They have significantly lower losses but take up more space [40].

4.1.3 *Oscillators*

By adding feedback, the energy loss of the resonators can be controlled. With strong positive feedback, the resonators even begin to oscillate. Parasitic resistances dissipate energy as quantified by the quality factor

$$Q = \frac{\omega}{2\alpha}, \tag{100}$$

the ratio of the resonator angular frequency ω over its attenuation rate α for some signal modeled proportional to $e^{-\alpha t} e^{\pm i\omega t}$. The quality factor is

2 The question mark in schematic labels is a placeholder for repetitions for each resonator.

(a) Picture of coil with variometer coil visible inside.

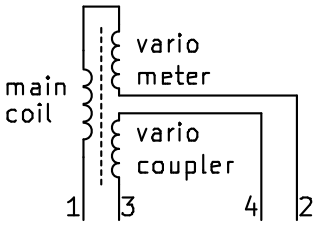

(b) Schematic of coils.

Figure 19: Illustrations for variometers and variocouplers, which allow tuning inductance and oscillator feedback.

interpreted as the ratio of damping time scale over the oscillation time scale. It typically ranges between 20 to 70 for our homemade coils. Using the intuition from the two-level system, we expect the U(1) dynamics to appear on the scale of the coupling strength $\Omega|b| \approx 0.1$ or faster for larger detuning, so we can state the requirement

$$\Omega|b| > \frac{\alpha}{\omega_0} \quad \text{or} \quad Q > \frac{\bar{\omega}}{2\Omega|b|} \tag{101}$$

for the U(1) dynamics to happen faster than the amplitude decay. Also note that the energy, on which hinges our definition of the conserved quantities, dissipates with the square of the amplitude, i. e. twice as fast.

The circuit fulfills this inequality with $\bar{\omega}/2\Omega|b|$ around 10 and Q being typically 50. Unfortunately, for good measurements, the inequality needs a larger margin to have the dynamics clear enough. Additionally, the coupling strength depends on the link amplitude which is also dissipating and thereby diminishing the coupling strength on the dissipation time scale.

As a remedy, the lost energy can be replenished by positive feedback. This concept was already employed in the regenerative receiver by Edwin Armstrong during the early days of radio technology. An amplifier element—tube or transistor—is inductively coupled to the resonator's inductor and its output current is fed back onto the resonator [41, 42]. The inductive coupling may be tuned such that the feedback just about compensates the dissipation, as done for the regenerative receiver, or increased further to obtain a sustained oscillation.

For the active element, a PNP bipolar junction transistor (MJE15035 [43]) is used together with matched NPN transistor (MJE15034) to bias the base to its turn-on voltage (see figure 20). The 10 Ω resistor protects against thermal

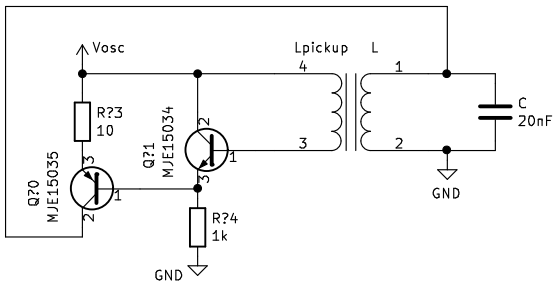

Figure 20: Schematic of Armstrong oscillator including the resonator on the right. The coupling between `L` and `Lpickup` is tunable. V_{osc} is the separate power source for all oscillators and limits the amplitude.

runaway [44]. Given a voltage V of the resonator, the pickup coil has the voltage $a\,V$ like a transformer with some ratio a. The NPN transistor biases this voltage to $V_B = V_{\text{BE,on}} + a\,V$ to the linear operating point $V_{\text{BE,on}}$ of the PNP transistor, which acts as transconductance amplifier. In the ideal setup the collector current driving the resonator is now proportional to the resonator voltage.

The current appears as a phase shifted driving of the resonator. For strong driving this affects the resonator frequency. Additionally, the feedback works only in one half period of the signal, when the pickup voltage is positive. However if the dissipation is small enough, the feedback should be small. In that case, phase shift and missing half should not have a large impact.

To have the pickup tunable, the homemade coils are further customized by mounting the pickup coil inside the primary windings on a rotating frame similar to the variometer setup. This *variocoupler* has three regimes of operation: the pickup coil produces negative feedback and the oscillator circuit increases the dampening, the pickup coil has small positive feedback and the oscillator circuit reduces the dampening, or the positive feedback is strong enough for sustained oscillation.

In the oscillating case, the amplitude is very sensitive to the variocoupler angle and easily latches onto the oscillator's power supply. This voltage limits the amplitude because the feedback circuit cannot drive current into the resonator when its voltage is higher than the supply voltage.

The oscillator has a non-trivial impact on Kirchhoff's current law for the resonators and might deserve to be included in the theoretical description of the circuit. For now we assume that its effect is ideal enough to just cancel some of the dissipation. In parts this is justified by measurements, but cases where it fails are discussed later on.

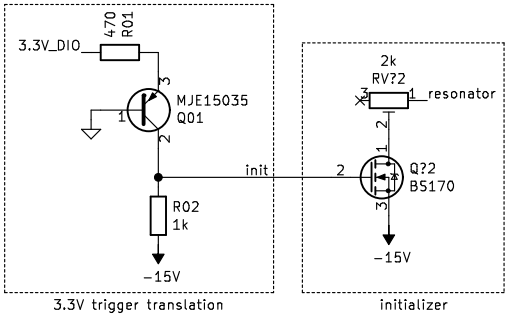

Figure 21: Translation for 3.3 V digital trigger to initializer line `init` on the left and the initializer on the right. The initializer is repeated for every LC resonator and connects to the non-grounded part of the inductor.

4.1.4 *Initializers*

Initializers are needed, because driving the circuit at one node with all others being zero, the signal cannot propagate along the chain. If two resonators connected to a mixer core have zero amplitude, all of its outputs are also zero. To solve this, all resonators have an initializer that generates a step function in the external node currents I_{ext}. As a crucial requirement, the initializer must not dissipate energy from the resonator after the trigger was fired.

The initializer current is switched by a n-channel MOSFET, model BS170, as shown in figure 21. The trigger line shared across all resonators is idle at $-15\,\text{V}$ where the MOSFET is in cutoff mode, i. e. the drain current is zero, independent of the drain voltage. The drain voltage follows the resonator voltage and the energy dissipation is negligible. When pulling the trigger line to GND, current flows and the new operating point is in the linear region of the MOSFET limited by the trimmable series resistance (see figure 4 in ref. [45] for on-region characteristics). The initializer current can be trimmed via $\texttt{RV}_{?2}$, but the actual initializer value is impaired by the fluctuations of the negative power supply rail.

To approximate a step function, the switching time needs to be much faster than one period of the highest frequency resonator. This time depends on the capability of the pull-down resistors to drain the MOSFET's gate capacitance back to $-15\,\text{V}$ and is typically 100 ns to 1 µs, limiting the circuit to 1 MHz.

4.1.5 *Housekeeping*

The board features 2 mm mini banana sockets for $\pm 15\,\text{V}$, V_{osc}, and ground. Boards can be easily connected to a chain via a set of pinhead connectors on each corner providing connections for power, the initializer trigger line and the signal of the chain.

Decoupling capacitors stabilize supply voltages for active elements against the small but non-vanishing resistance of the copper layer and noise from other active elements. There are two sets of decoupling capacitors: one 0.1 µF ceramics capacitor for each supply pin of the multipliers, also placed physically close to it, and one 330 µF electrolytic capacitor per supply voltage and board.

As for the SSH model, Red Pitayas are used for data taking. Additionally, triggering and initialization are performed via the digitial IOs of the FPGA: One digital IO, `DIO0_N`, is set by the measurement script to idle at logic 0 (0 V), then to logic 1 (3.3 V) for the initializers, and back to 0 to start measuring. The external trigger of the fast IO is set to the negative edge of this output. The 3.3 V signal is translated to the initializer line at -15 V using the setup in figure 21. By relaying the trigger output of one Red Pitaya to the external trigger of others, multiple Red Pitayas can be synchronized to increase the number of available channels.

4.1.6 *Dimensioning*

Why are the values of capacitors, inductors and other parts chosen as presented above? While exact values are mostly due to availability of parts, their rough values are a trade-off of the following restrictions:

- Resonator frequencies are limited from above by the multiplier bandwidth around 100 kHz. On the other hand, small frequencies require large inductors and capacitors.
- Currents inside the LC tank circuits have to comply with maximal source / sink currents of 30 mA at multiplier outputs.
- Voltages have to stay well above the noise floor of roughly 10 mV and well below the multiplier maximum ratings of 10 V.
- Capacitor values have to stay above parasitic capacitances, but large capacitors deteriorate the multiplier bandwidth.
- Inductors also should be significantly larger than parasitic inductances, but larger inductors have higher losses. The latter constraint was relaxed by changing to air coils.
- All of the above are related by the resonators following the relationship

$$V_{\mathrm{pp}} = \sqrt{L/C}\, I_{\mathrm{pp}} = L\omega I_{\mathrm{pp}}, \quad \omega = 1/\sqrt{LC}, \tag{102}$$

  where V_{pp} and I_{pp} are peak-to-peak voltage and current inside the LC tank circuits.

These conditions rely heavily on the specifications of the multipliers. Specialized multipliers with higher bandwidth could be used but also are much less robust for our prototyping process, as more high frequency effects would become important.

4.1.7 *Howland current pump*

Measurements for the U(1) chain are done with external currents to find frequency dependent features. A Howland current pump, which is a voltage controlled current source, is used to supply the external currents. This circuit is not part of the U(1) building block and lives on a separate circuit board.

The design with schematic in figure 22 is adapted from refs. [46, 47]. It is based on a general purpose operational amplifier (op amp), the `TL071`, which forms a non-inverting amplifier via R_3 and R_4. If the condition

$$\frac{R_1 + \mathtt{RV}_1}{R_2 + R_5} = \frac{R_3}{R_4} \tag{103}$$

is fulfilled, which can be achieved by tuning the potentiometer $\mathtt{RV}_1$, the current I_{out} through R_{sense} is

$$I_{\text{out}} = \frac{R_4}{R_3}\frac{1}{R_5}V_{\text{in}} = \frac{1}{180\,\Omega}V_{\text{in}}. \tag{104}$$

The resistor R_{sense} allows us to measure the actual output current via the voltage difference as

$$I_{\text{out}} = \frac{V_{\text{circuit}} - V_{\text{sense}}}{R_{\text{sense}}}. \tag{105}$$

In this design, the output current is provided by the op amp output, which can source / sink about $\pm 20\,\text{mA}$ [48]. At the maximum current of 20 mA, the op amp output has to be about 4 V above / below the output voltage. Since the maximum output ratings of the `TL071` are $\pm 12\,\text{V}$, the compliance range of this Howland current pump is limited to a range of $\pm 6\,\text{V}$ in V_{circuit}. The compliance range increases with lower currents.

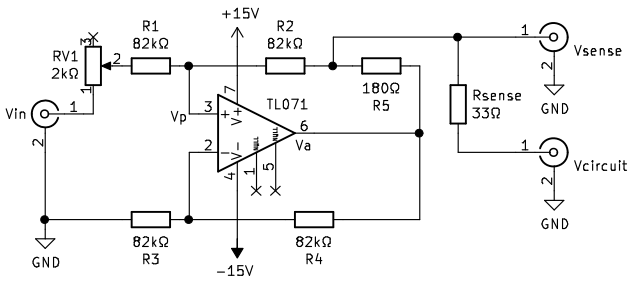

Figure 22: Schematic of Howland current pump. Full parts list in appendix B.3.

4.2 TUNING THE CIRCUIT

Before taking measurements, there are a number of parameters that need to be set or determined:

- Initializer current / initial resonator energy,
- Resonator frequency (feedback turned off),
- Resonator quality (feedback turned off),
- Oscillator frequency (feedback turned on),
- Oscillator amplitude (feedback turned on), and
- Reference voltage of multipliers.

In the following text, when talking about 'signals,' the voltage of sites or links is meant. It is measured as the voltage across the inductors of the site, of which one side is ground.

The initializer current is not determined directly, but inferred from the first peak of the resonator oscillations. Before time $t = 0$, the energy of all resonators is stored in the magnetic field of the coil as supplied by the initializer current. After turning of this external current, the energy oscillates into the capacitor where the first voltage peak is measured. Assuming negligible losses during that quarter period, the initial peak V^{in} allows the estimation of the initial energy $E^{\text{in}} = C(V^{\text{in}})^2/2$.

4.2.1 *Resonators*

The resonator frequency and quality are measured with the feedback turned off. The multipliers are connected to the resonator, because their output resistance has a non-negligible impact on frequency and quality. To avoid any coupling, other sites are turned off by disconnecting their initializers and feedback.

From the resulting signal, the peaks $(V_i)_{i=1\ldots n}$ at times $(t_i)_{i=1\ldots n}$ are extracted. They allow the estimation of the frequency

$$f_{\text{free}} = \frac{n-1}{t_n - t_1} \tag{106}$$

and by fitting an exponential proportional to $e^{-\alpha t}$, the dissipation timescale α is determined. Together with f_{free} it allows the calculation of the dimensionless quality factor Q. Figure 23 shows a resonator signal and illustrates the exponential fit.

The precision of f_{free} is better then one per thousand, but is limited by the peak detection, which causes an error of up to 0.5 kHz for frequencies

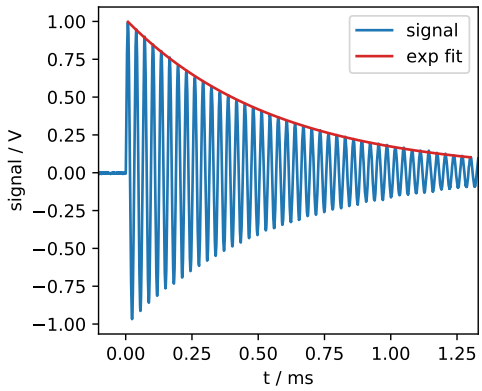

Figure 23: Resonator signal for site 1 without feedback. See table 1 for f_{free} and Q.

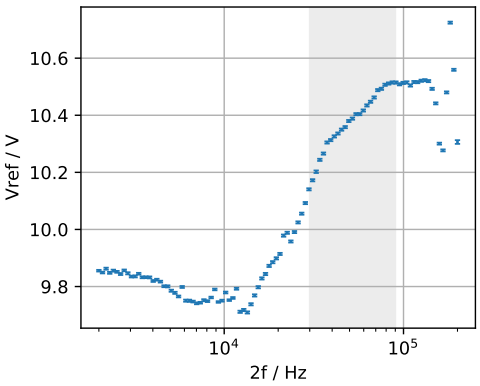

Figure 24: Frequency dependence of the reference voltage V_{ref}. The shaded region highlights the region relevant for the U(1) model.

between 30 kHz to 90 kHz. The quality factor has an additional error due to the precision of the exponential fit for α. The quality factors of the resonators in our circuit have uncertainties of about 5 at typical values of around $Q = 50$.

The digitization of the signal to 14 bits over a possible input range of $\pm 20\,\text{V}$ results in a resolution of 2.9 mV. The noise of a resonator at rest, connected to the multiplier, has a root mean square (RMS) noise of about 3.5 mV. However, upon connecting the oscillator feedback, high frequency oscillations appear with an amplitude of about 16 mV.

To remedy some of the noise, the signal is smoothed with a third order Savitzky-Golay filter before peak detection, which is possible because the signal is well sampled. The remaining noise in the peaks is estimated from the RMS of consecutive peak heights:

$$\sigma_V = \frac{1}{\sqrt{2}} \,\text{RMS}\,(V_{i+1} - Vi)\,. \tag{107}$$

For site 1 at 31 kHz this amounts to roughly 10 mV. Additionally, the filter improves the precision of peak positions t_i from about 0.5 µs to 0.3 µs.

These uncertainties are also valid for the frequency and amplitude measurements for oscillators, which have active feedback. The amplitude is determined by the average peak height after the oscillator reached its equilibrium amplitude.

4.2.2 *Reference voltage*

The reference voltage of the multipliers directly affects the coupling strength of our model. It is tunable and needs to be set consistently among the multipliers in one multiplier core. To measure it, one multiplier is singled

out and fed the harmonic signal $V_{\text{in}} \cdot \cos(2\pi f t)$ to both of its inputs. Its output signal should then be

$$V_{\text{out}} = \frac{1}{2} \frac{V_{\text{in}}^2}{V_{\text{ref}}} \left(1 - \cos(2\pi\, 2f\, t)\right), \tag{108}$$

which can be inverted to give V_{ref}. From measured signals, the amplitudes V_{in} and V_{out} are determined by quadrature amplitude demodulation at frequency f and $2f$.

For these measurements, the inductors are disconnected from the circuit board to reduce loading of the Red Pitaya outputs. See figure 24 for results for the largest V_{ref}, i. e. smallest coupling, that can be realized with this circuit. The output signal has twice the input frequency, therefore the data is plotted over $2f$. Uncertainties are estimated from the demodulation error. Over the range of $2f = 30\,\text{kHz}$ to $90\,\text{kHz}$, which is the range of resonance frequencies of sites and links, the reference voltage falls between $10.1\,\text{V}$ to $10.4\,\text{V}$.

4.3 TWO-LEVEL SYSTEM

As introduced in section 3.3, the circuit becomes equivalent to the two-level system in the configuration with two sites with an externally driven link. After determining the effect of oscillator feedback strength, we take a look at the level repulsion and beat phase and contrast.

The two-level system is a subset of the circuit model depicted in figure 31. One U(1) block is used with two coils connected to `J1` and `J2` (see full schematic in figure 35 on page 80 for schematic labels). Jumper `J33` is opened, which disconnects the link resonator from the rest of the circuit. Then `BNC3` drives the multiplier inputs directly without being loaded by the resonator. The driving input is a voltage, so the Howland current pump is not needed for the following measurements.

The supply voltage for multipliers and initializers is set to $V_{\pm} = \pm 13.0\,\text{V}$ stable to $0.5\,\text{V}$. The supply voltage is chosen lower than the originally intended $\pm 15\,\text{V}$, because the power supply is more stable around $\pm 13\,\text{V}$ and the lower voltages are still acceptable for the multipliers. The oscillator control voltage, which is also the voltage scale for dimensionless quantities, is set to $V_0 = 1.00\,\text{V}$ with a residual ripple of $5\,\text{mV}$ according to the power supply manual. The initializers are tuned to an initial amplitude of $V^{\text{in}} = 1.00(6)\,\text{V}$, equal to the oscillator control voltage V_0, but remember that the initializer amplitude fluctuates proportional to V_-.

Before turning on the interaction, some properties of the sites are determined. Table 1 lists the resonance frequency and quality of the sites without any feedback. It also lists oscillator frequency & amplitude with the feedback

Quantity	Symbol	Site 1	Site 2
Coil code name		Janus	Mintaka
Quality (no feedback)	Q	54	60
Resonance (no feedback)	f_{free}	30.8(5) kHz	80.3(5) kHz
Oscillator frequency	f_{osc}	31.0(5) kHz	85.0(5) kHz
Oscillator amplitude	V_{osc}	1.00(1) V	1.01(1) V
Dim.less f_{osc}	$\bar{\omega}$	0.517(8)	1.417(8)
Initial variables	a^{in}	$i\,0.98(6)$	$i\,0.59(4)$

Table 1: Tuning of resonators without feedback and with oscillator feedback. Measurements and uncertainties as described in section 4.2. Additionally the dimensionless quantities $\bar{\omega}$ and a^{in} are listed.

tuned to a sustained 1 V oscillation. Note the large impact of the feedback on the frequency of site 2. With the frequencies around 31 kHz and 85 kHz, the (arbitrary) frequency scale $f_0 = \omega_0/2\pi = 60\,\text{kHz}$ is chosen for dimensionless units.

For orientation, the table also lists the dimensionless frequencies $\bar{\omega} = f_{\text{osc}}/f_0$ and the initial complex variables a^{in}. They are purely imaginary since the initializer energy is stored as flux in the inductors. But since the voltage of the capacitor is more directly accessible than the current through the coils, the initial conditions are inferred from the first peak V^{in} of the voltage signal. The first peak *approximately* corresponds to all energy stored in the capacitor and allows calculating a^{in} as

$$a_x^{\text{in}} = i\frac{1}{\sqrt{2\bar{\omega}_x}}\frac{V^{\text{in}}}{V_0} \tag{109}$$

according to equation (60).

The reference voltage of the multipliers is adopted from section 4.2.2, where it was set to its maximum. As determined it is $V_{\text{ref}} = 10.3\,\text{V}$ with a systematic error of 0.2 V due to its frequency dependence.

4.3.1 *Oscillator feedback*

All of the parameters above stay the same for all measurements of the two-level system. The parameters that are changed are: the link frequency f_{link}, phase β, and amplitude V_{link} and also the oscillator feedback. The latter parameter is the hardest to set and quantify, as the angle of the vario-couplers is not very precise and the resulting feedback current has a non-trivial dependence on site amplitude. There seem to be three regimes and we take three sets of measurements at various settings of the oscillator feedback.

For these measurements the link is set to an amplitude of 0.5 V and its frequency is scanned over the region of small detuning around 54 kHz. One

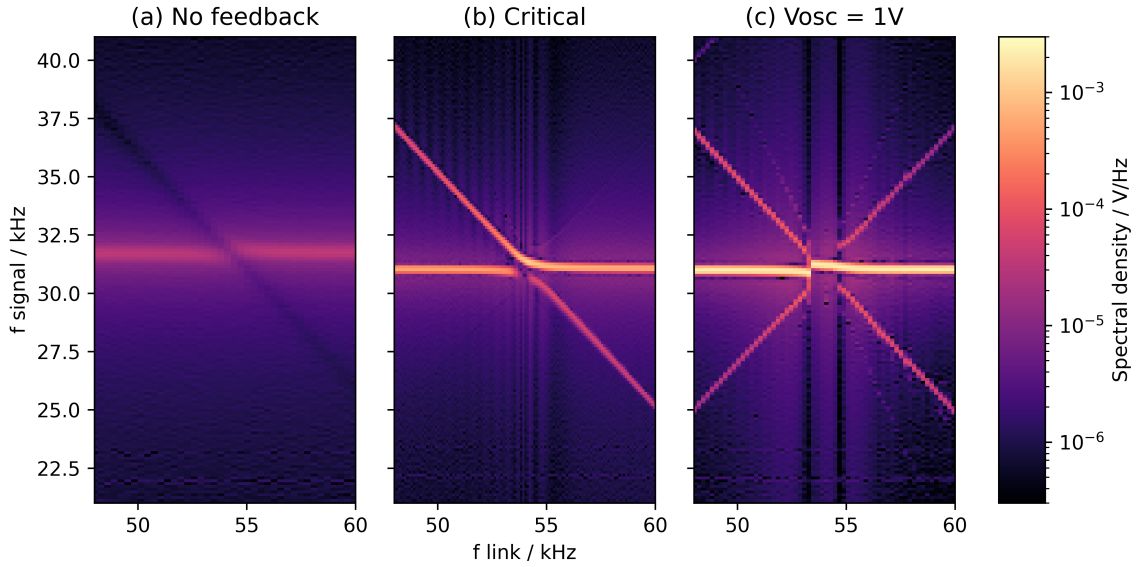

Figure 25: Spectrum of site 1 in 2-site configuration with driven link at $V_{\text{link}} = 0.5\,\text{V}$. (a) In resonators without oscillator feedback, the signal drops fast producing a washed out peak at the resonance. (b) Close to critical feedback there is a clear avoided crossing of two levels. (c) With the oscillators set to an amplitude of 1 V, the feedback overpowers the beat close to resonance.

set of measurements is done with the feedback circuit disconnected from the site and the pickup coil orthogonal to the main inductor (to reduce losses). As a result the amplitude of the signal decays with a quality Q roughly similar to the one measured before (see table 1). The fast decay smears out the peak in the spectrum.

Only when turning on the feedback, the interaction between the sites becomes clearly visible, including the expected two-level structure. See figures 25 and 26 for spectra (discrete Fourier transformation of voltage signal) and representative voltage signals.

However if the feedback is too strong, the two-level structure is again lost (spectrum on the right side of figure 25). In this regime are two distinct behaviors:

- For large detuning a third frequency component shows up to the two-level structure and the spectrum becomes symmetric around the resonance frequency of site 1. The symmetric counterpart affects contrast and phase of the beat. To understand this, imagine shifting the resonance frequency to zero. Then the two other peaks become positive and negative opposites of the same frequency. That strong feedback affects the contrast of the beat is not unexpected, since it tries to force the signal amplitude to the oscillator control voltage.
- Close to zero detuning only one frequency component is left. Here the beat seems slow enough so that the feedback can suppress the beat completely and only one frequency component remains.

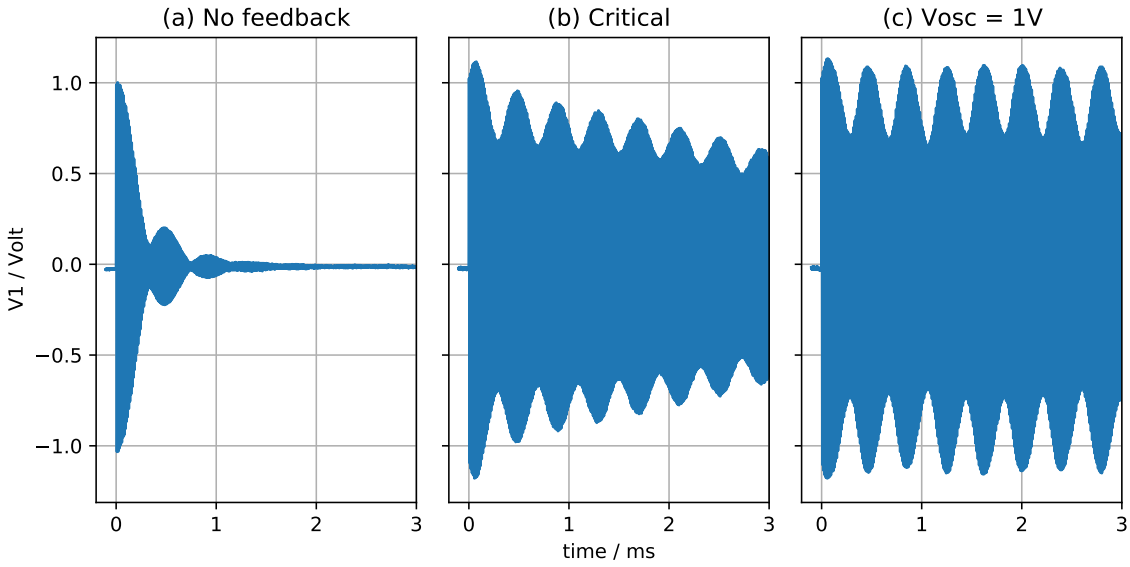

Figure 26: Snippet of voltage signal corresponding to vertical line in figure 25 at a link driving frequency of $f_{\text{link}} = 56.5\,\text{kHz}$. The full recording is 8.4 ms long at a sample rate of 1.95 Msps. The trigger is located here at $t = 0$. The beat is clearly visible, but also the strong dissipation without any feedback.

When looking at figure 26 the beat is well defined for (near) *critical* feedback and *stable* oscillation around 1 V. In the following sections, measurements with critical feedback are used for investigating the beat properties.

4.3.2 *Driving amplitude*

We have seen that two-level structure appears upon scanning the detuning in the case of critical feedback. Before the quantitative analysis of that structure, we take a look at the qualitative effect of scanning the link amplitude. The link amplitude appears in the equations of the two-level system together with the coupling strength Ω and can therefore be used to control it.

Figure 27 shows a measurement of doing exactly that at a detuning of about 1 kHz. Additional side frequencies appear already at very low driving amplitude and at a distance of roughly 1 kHz, i. e. the detuning, from the main peak. From eq. (83), we expect the distance between the peaks to depend on detuning and driving like $\sqrt{\Delta^2 + 4\Omega^2|b|^2}$. When the coupling strength becomes large enough relative to the detuning, it should increase the peak distance. This effect is realized in the measurements and evident in figure 27.

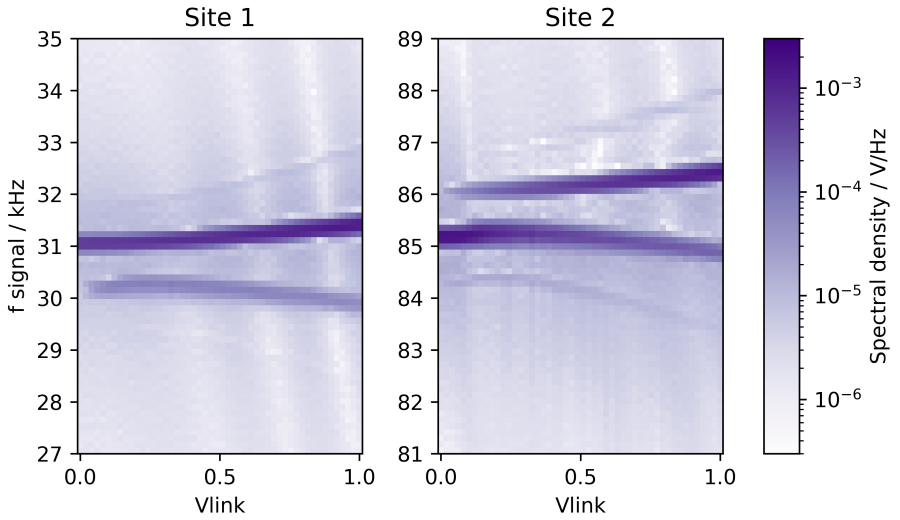

Figure 27: Effect of increasing the coupling by raising the link amplitude V_{link} at constant link frequency $f_{\text{link}} = 55\,\text{kHz}$. Side frequencies appear at the detuning 1 kHz and move apart for stronger coupling.

4.3.3 *Avoided crossing*

At critical feedback conditions, the spectrum looks similar enough to the two-level structure, that the peak positions may be fitted to the theoretical model in eq. (83). The fit is done on a spectrum taken with varying detuning at a driving amplitude of $V_{\text{link}} = 0.8\,\text{V}$. See appendix A.1 for the calculation and normalization of spectra.

For the fit, the two largest peaks of the spectrum are assigned to the appropriate level of the two-level structure. As uncertainties the half width at half height is taken, which is close to the spectral resolution of 0.1 kHz. The fit model for the lower and upper levels at site 1 and 2 is based on eq. (83):

$$\begin{aligned} f_{1,2;\text{lo,up}}(f_\delta) &= f_{1,2} \pm \frac{1}{2}\left(\sqrt{f_\delta^2 + 4f_{\Omega b}^2} \pm f_\delta\right) \\ f_\delta &= f_1 + f_{\text{link}} - f_2 \end{aligned} \tag{110}$$

with the link frequency f_{link} being the independent variable. $f_{1,2} = \bar{\omega}_{1,2}\, f_0$ are dimensionful resonance frequencies and $f_{\Omega b} = \Omega|b|\, f_0$ captures interaction and driving strength.

Figure 28 shows the spectrum, peaks and the best fit. Results for the fit parameters are listed in table 2, including the reduced χ^2, which indicates that the uncertainties are larger than the actual scatter of the data around the model. While the fit is run separately for each line, the results are compatible within uncertainties and table 2 lists the combined result reached by averaging over all four fits. The resonance frequencies found in the fit also agree with the uncoupled oscillator frequencies in table 1.

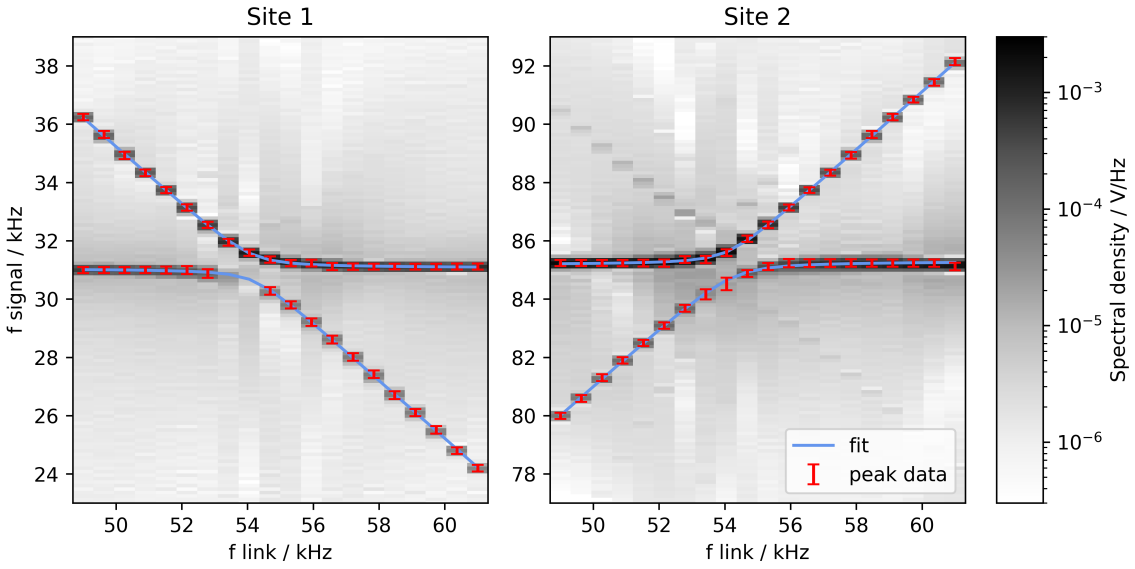

Figure 28: Spectrum and fit of avoided crossing in 2-site configuration with driven link at $V_{\text{link}} = 0.8\,\text{V}$ and oscillator feedback near critical.

The third fit parameter $f_{\Omega|b|}$ determines the gap in the two-level structure. It allows the calculation of the interaction strength

$$\Omega_a = \frac{f_{\Omega b}}{f_0\,|b|}, \quad |b| = \frac{1}{\sqrt{2 f_{\text{link}}/f_0}} \frac{V_{\text{link}}}{V_0} \tag{111}$$

where $V_{\text{link}} = 0.8\,\text{V}$ and $f_{\text{link}} = f_2 - f_1$ for the gap at zero detuning. The result should be compared to the interaction strength calculated according to its definition in eq. (62):

$$\Omega_b = \sqrt{\frac{f_1\, f_{\text{link}}\, f_2}{2^5\, f_0^3}}\, \frac{V_0}{V_{\text{ref}}} \tag{112}$$

with frequencies $f_{\text{osc},1}$ and $f_{\text{osc},2}$ determined from the uncoupled oscillators (table 3). The two variants of Ω evaluate to

$$\begin{aligned} \Omega_a &= 0.0134(16), \\ \Omega_b &= 0.0139(03). \end{aligned} \tag{113}$$

They are consistent, even when considering that the uncertainty for Ω_a is overestimated, as it is calculated from the fit result with $\chi^2_{\text{red}} < 1$. These results show that the Hamiltonian description works well for the frequency components of this circuit configuration.

	Site 1 lower	Site 1 upper	Site 2 lower	Site 2 upper	combined
f_1/kHz	31.04(6)	31.07(5)	31.06(7)	31.08(5)	31.06(2)
f_2/kHz	85.25(6)	85.18(6)	85.30(6)	85.17(6)	85.22(3)
$f_{\Omega b}$/kHz	0.43(16)	0.47(10)	0.55(12)	0.46(10)	0.48(6)
χ^2_{red}	0.07	0.06	0.18	0.08	

Table 2: Best fit parameters for the two-level spectrum.

4.3.4 *Beat phase*

The next feature we look at, is the phase of the beat. Its dependence on the link phase is an result of the U(1) gauge symmetry. For the setup with critical feedback, a set of measurements is taken at $f_{\text{link}} = 56\,\text{kHz}$, $V_{\text{link}} = 0.80\,\text{V}$ and a link phase between $-180°$ to $180°$.

In section 4.2 about tuning the circuit, the envelope of the signal was used including a description on how to obtain it. Here we use the positions $(t_i)_{i=1\ldots n}$ of the envelope's peaks with their uncertainty estimated from the standard deviation of their distance:

$$\sigma_t = \frac{1}{\sqrt{2}} \operatorname{std}(t_{i+1} - t_i). \tag{114}$$

Together with the beat frequency f_μ, each peak gives one estimate for the phase:

$$\alpha_i = \frac{\pi}{2} - 2\pi f_\mu t_i, \quad f_\mu = \frac{n-1}{t_n - t_1}. \tag{115}$$

Their mean is used as best estimate for the beat's phase. See appendix A.2 for how to calculate the mean of a set of angles. The uncertainties of the peak positions are assumed to propagate almost linearly through the circular mean of the angles like they do for the Euclidean mean.

Only the first 4 ms of the signal are used, because after that the low contrast makes the peak detection too unreliable. Figure 29 shows the beat phase calculated in this way and the first thing to notice is the much larger uncertainties for site 1 than for site 2. This is caused by lower contrast and a more irregularly shaped beat of site 1, possibly caused by a slightly weaker feedback, i. e. stronger dissipation. The scatter of data for site 1 appears together with outliers of f_μ, indicating that this is limiting the precision.

Additionally the plot contains the modeled beat phase based on eq. (85) with values from the fit results in table 2. It is mostly consistent with site 1, but the more precise data of site 2 reveals a systematic deviation, which does not correspond to a trend in the frequency estimation. The deviation goes to smaller phases than the model, meaning that the measured signal is delayed compared to the expected signal. It appears for α around $-270°$

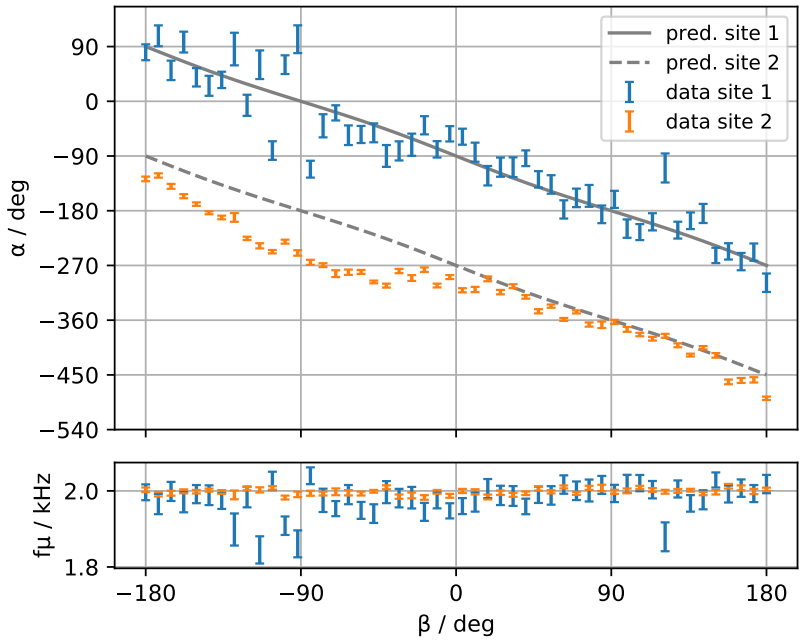

Figure 29: Phase α of beat depending on the phase β of the link. Grey lines show predicted values based on fit data in table 2. For reference the estimated beat frequency f_μ is shown in the lower diagram.

(corresponding to 90°), where the envelope has maximal amplitude. This might be an error due to the phase estimation algorithm. It typically uses the third to eighth peak of the signal and does not include the first peak for the estimation, even though there the beat phase is defined. Judged by its shape, the first peak is affected most by dissipation, which could also cause a phase shift in the following beat. In the end this systematic deviation remains without a conclusive explanation.

4.3.5 *Conserved quantities*

The Hamiltonian for the two-level system has global U(1) symmetry and therefore the total number

$$G_{\text{tot}} = a_1^* a_1 + a_2^* a_2 \tag{116}$$

from eq. (77) should be conserved. In dimensionful quantities it reads

$$H_0 G_{\text{tot}} = \frac{\omega_0}{\omega_1} E_1 + \frac{\omega_0}{\omega_2} E_2 \tag{117}$$

with E_1 and E_2 being the energies in the resonators. Figure 30 shows the behavior of the energies and the total number. In the following text, G_{tot} is also used to denote its dimensionful value.

The most important effect is the remaining dissipation in the critical regime, which causes a near exponential decay of G_{tot} towards some constant value.

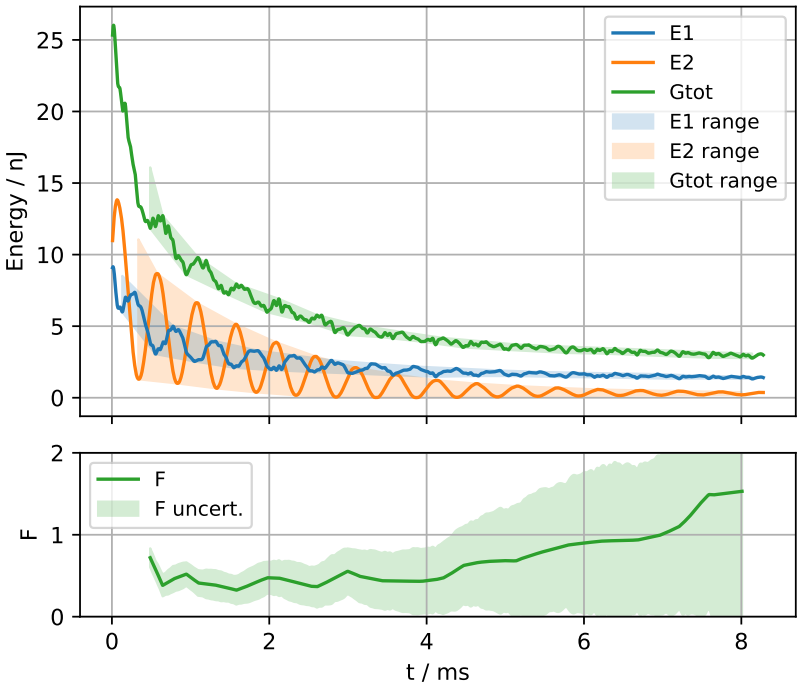

Figure 30: Violation of total number conservation in data taken at critical feedback, $f_{\text{link}} = 56\,\text{kHz}$, and $V_{\text{link}} = 0.8\,\text{V}$. Shaded regions in the upper plot indicate ranges of the beat, which are used to calculate the violation F introduced in the text. $F = 0$ corresponds to perfect conservation. Values above one indicate strong violation.

The second important characteristic is the beat with opposite phases in site 1 and 2. In the beginning with high contrast, the total number shows significant violations related to the beat.

With the measurement at hand, we may try to find a quantitative measure for the violation. In ref. [49] Yang et al. quantify violation in a statistical context for a quantum simulator. They sum over the measured probabilities of all allowed states and subtract it from unity. Without statistical framework we have to find another definition.

There are multiple options for disentangling the features present in figure 30. We could for example divide out the exponential decay, remove constant offsets, or smooth out fast components, but in the end the measure of violation needs to be simple enough to provide a reliable interpretation. We are looking for a dimensionless quantity that ranges between one value meaning perfect conservation and another value indicating maximal violation.

By looking at peaks and troughs in the energies E_1 and E_2, we can define the ranges ΔE_1 and ΔE_2 between peaks and troughs. These ranges capture the variation of the energy, esp. the beat, which seems to be the important feature related to our gauge theory. The same can be done to get the range ΔG_{tot} of G_{tot}. Between peaks, the range is interpolated linearly.

Perfect conservation is realized when G_{tot} is constant, i. e. its range vanishes. Maximal violation means that the variations in E_1 and E_2 are independent, which is not directly related to a specific behavior of G_{tot}, but the variation of G_{tot} should then be of similar size as the variations of E_1 and E_2. This motivates the definition of

$$F = \frac{2\,\Delta G_{\text{tot}}}{\frac{\omega_0}{\omega_1}\,\Delta E_1 + \frac{\omega_0}{\omega_2}\,\Delta E_2} \;\in\; [0, 2]. \tag{118}$$

It is zero for perfect conservation. A value of one indicates maximal violation. F can become larger than one, if either ΔE_1 or ΔE_2 vanish, or in case their dynamics are 'synchronized' instead of opposites and add up instead of cancel out.

Note how the definition of the range via peaks and troughs implicitly defines a scale. Decreasing the minimum distance between peaks picks up more higher frequency components while increasing the minimum distance would increase the impact of the exponential decay.

Figure 30 shows the violation F calculated for G_{tot}. In the beginning it is roughly 0.5, but deteriorates with diminishing energies. At later times the violation becomes worse, because the range of the E_1 vanishes and the uncertainty increases due to stronger impact of the scatter in the voltage measurements compared to the smaller ranges of the beat. We will come back to this measure of violation in the context of Gauss's law for the full U(1) model.

4.4 THREE SITE U(1) MODEL

During the time of this project, a chain of three sites and two links for the full U(1) model could be realized. The circuit is distributed across two boards with the layout already presented in figure 17 in the introduction of this section and the full setup is pictured in figure 31. This section presents first measurements with this chain and comparisons to simulations.

Since the parameter space is quite large, two setups are presented here as examples. They differ in the tuning of the resonators, the feedback strength and the setting of the initializers. The tuning is listed in table 3. The initializers are turned on and set to a voltage of $V^{\text{in}} = 1.00(6)\,\text{V}$, but for set (2) the initializer of the driven site 1 is disconnected. The Howland current pump is connected to site (1) and its control voltage has an amplitude of 0.05 V which corresponds to $I_{\text{drv}} = 0.28\,\text{mA}$. The voltage drop across R_{sense} at the output of the current pump confirms the order of magnitude, but also shows that I_{drv} varies from 0.25 mA up to 0.43 mA depending on the behavior of the circuit. In figures 32 and 33 sets (1) and (2) are shown. In both cases the independent variable is the driving frequency f_{drv}.

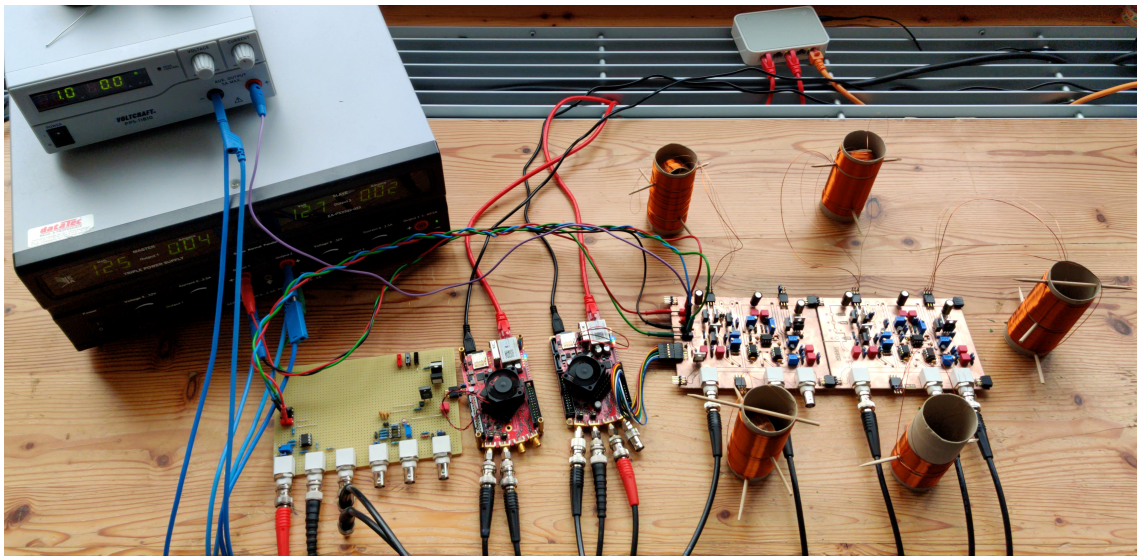

Figure 31: Photograph of the setup for measuring the U(1) model. Power supplies in the top left corner; circuit boards from left to right are the Howland current pump, two Red Pitayas, and two connected U(1) boards with five inductors.

	Site 1	Link 1	Site 2	Link 2	Site 3
Coil	Janus	Nepenthe	Mintaka	Ogat	Preenos
$f_{\text{osc}}^{(1)}$/kHz	31.05	55.31	85.03	56.48	30.88
$f_{\delta}^{(1)}$/kHz		+1.33		+2.33	
$f_{\text{osc}}^{(2)}$/kHz	31.78	56.59	84.39	56.57	30.84
$f_{\delta}^{(2)}$/kHz		+3.98		+3.02	

Table 3: Tuning of resonators and the resulting detuning for the two sets of measurements. Measurements and uncertainties as described in section 4.2. Additionally the dimensionless quantities $\bar{\omega}$ and a^{in} are listed.

While the two-point impedance was a good way to identify edge modes in the SSH model, dividing out the driving current is not sensible for the U(1) model. Due to the non-linearity, the full temporal spectrum has to be taken into account, not only the response at the same frequency of the driving. The spectra should contain two components: the response to the step function of the initializers and the effect from driving. They do not form a linear superposition due to the non-linearity of the model, but should be affected by interactions between them. The initial step function was not part of the measurements of the SSH model, where the time evolution consisted of the driven part only, but here the initialization is needed to allow propagation along the chain.

Indeed these two components seem to be present in the spectra and may be told apart by their dependence on f_{drv}. Frequency components from the initializer response should be independent of the driving frequency—as long as they don't interact with it—and appear as mostly horizontal lines in the

diagrams. In the same vein, diagonal lines with a slope of unity are directly related to the driving frequency f_{drv}.

Similar to the two-level structure at strong driving, the data for three sites has a systematically different region at driving close to zero detuning. Apart from these regions, the interaction between initializer response and driving seems to be in parts similar to the avoided crossing in the two-level system. This suggests that perturbative solutions to the system should seek to reproduce these avoided crossings.

Figures 32 and 33 also include simulations run with parameters matching the tuning of the measurement sets. While we can say that the measurement and simulation match at least qualitatively for f_{drv} far away from the first site's resonance f_1, they differ systematically for the region close to resonance. There the energies in the simulated resonators tend to diverge, which shows up in the spectra as strong noise over a broad region around the resonance. It is not unexpected that energy is pumped into the system close to resonances, but due to dissipation the same does not happen in the real circuit.

Note that, depending on the feedback, the equilibrium amplitudes of the oscillators differ from the initializer amplitude. For a near linear system, changing the initial amplitudes affects the prefactors of the eigenstates / modes of the system. Modes are directly detected as peaks in the spectra. With the actual oscillator amplitude different from the initial values of the simulation, the relative peak heights in the spectra are expected to be different, which matches observations.

For a quantitative statement about the circuit we turn again to conservation laws. The circuit has total number conservation due to its global U(1) symmetry, but we will skip this quantity in favor of the local charges G_x of Gauss's law. The same mechanism that was developed for the total number of the two-level system is applied here.

With the same configuration as for set (2), a measurement is taken but without external driving. Figure 34 shows the energies in the oscillators and the associated dimensionful charges calculated according to eq. (75):

$$\begin{aligned} G_1 &= \tfrac{\omega_0}{\omega_1} E_1 - \tfrac{\omega_0}{\omega_1'} E_1', \\ G_2 &= \tfrac{\omega_0}{\omega_2} E_2 + \tfrac{\omega_0}{\omega_1'} E_1' + \tfrac{\omega_0}{\omega_2'} E_2', \\ G_3 &= \tfrac{\omega_0}{\omega_3} E_3 - \tfrac{\omega_0}{\omega_2'} E_2'. \end{aligned} \tag{119}$$

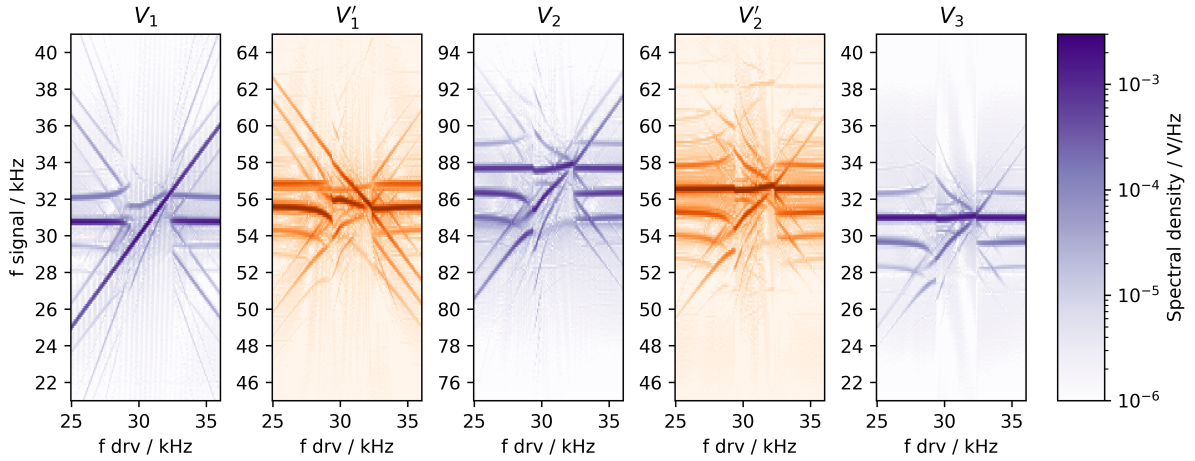

(a) Measurements showing two regions of systematically different behavior.

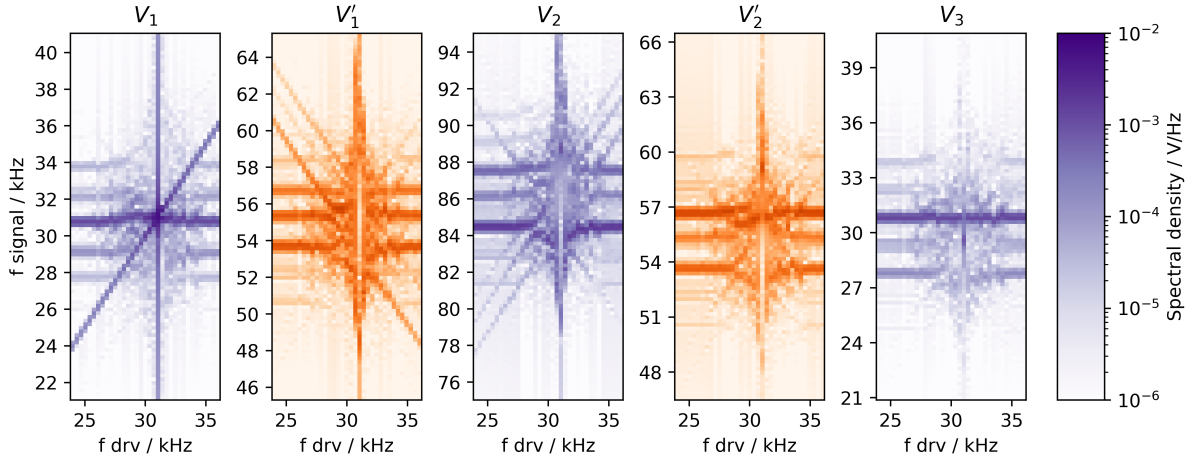

(b) Simulation corresponding to measurements with tuning according to table 3.

Figure 32: Measured and simulated spectra for set (1) with $I_{\mathrm{drv}} = 0.3\,\mathrm{mA}$. Links have an orange color map as opposed to the blue one for the sites.

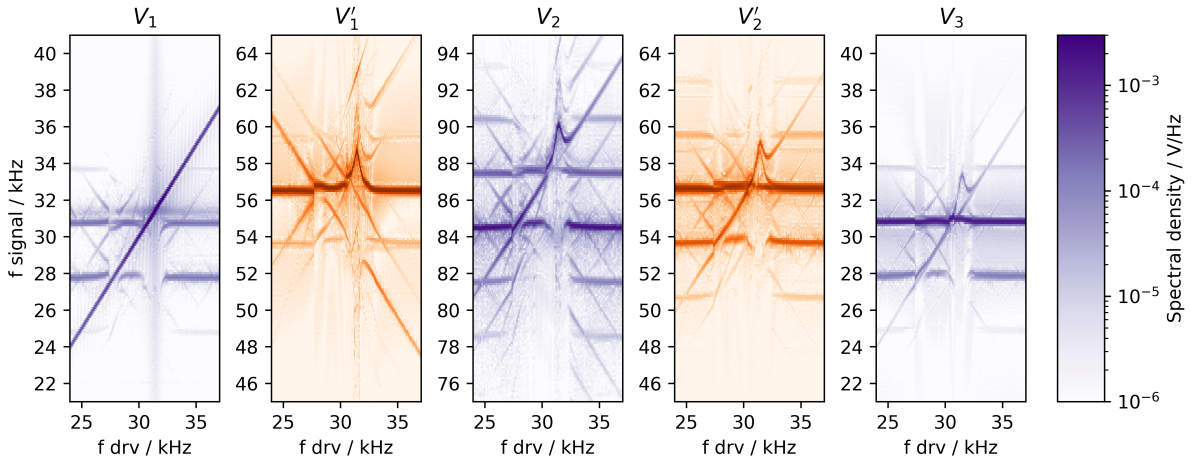

(a) Measurements. Site 1 fainter for not being initialized.

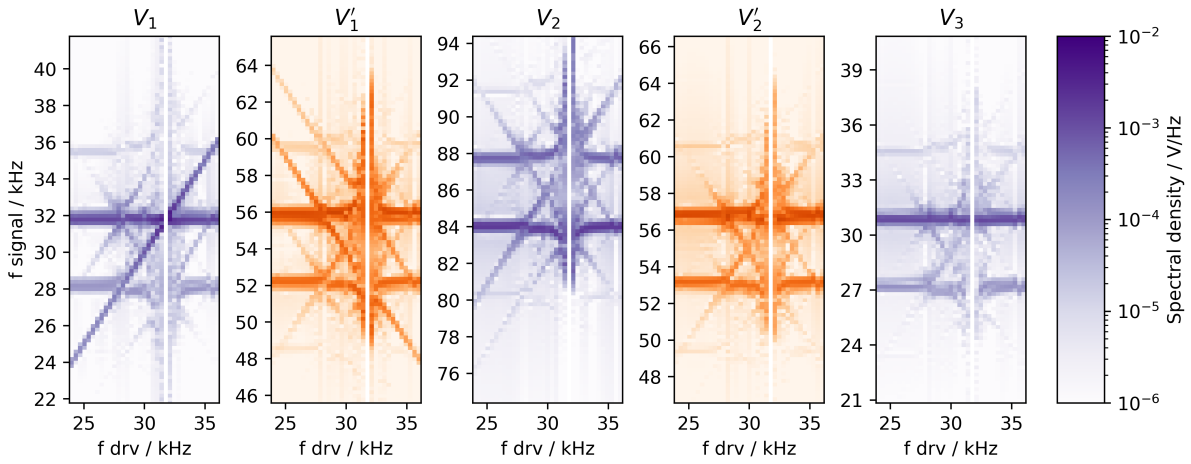

(b) Simulation corresponding to measurements with tuning according to table 3.

Figure 33: Measured and simulated spectra for set (2) with $I_{\mathrm{drv}} = 0.3\,\mathrm{mA}$. For set (2), site 1 was not initialized, which changed the behavior close to resonance significantly compared to set (1).

With the same algorithm as described in section 4.3.5 we determine the ranges $\Delta E_x^{(\prime)}$ of the energies and the charges ΔG_x. This allows the definition of the violations

$$\begin{aligned} F_1 &= \frac{2\,\Delta G_1}{\frac{\omega_0}{\omega_1}\,\Delta E_1 + \frac{\omega_0}{\omega_1'}\,\Delta E_1'} \\ F_2 &= \frac{3\,\Delta G_2}{\frac{\omega_0}{\omega_2}\,\Delta E_2 + \frac{\omega_0}{\omega_1'}\,\Delta E_1' + \frac{\omega_0}{\omega_2'}\,\Delta E_2'} \\ F_3 &= \frac{2\,\Delta G_3}{\frac{\omega_0}{\omega_3}\,\Delta E_3 + \frac{\omega_0}{\omega_2'}\,\Delta E_2'} \end{aligned} \tag{120}$$

which is the range of the charge over the average range of its contributions. Similar to before, the interpretation is as follows: The closer F is to zero, the smaller is the violation of the conservation law. At $F \gtrsim 1$ we say the energies of the oscillators are independent, though there is no rigorous notion of statistical independence involved. F_1 and F_3 have maximal values of 2, while F_2 has the maximal value of 3. The maximal values correspond to the resonator energies being exact opposites in the way, that they add up to the maximal range ΔG_x, in which case speaking of 'independence' does not seem justified. The term *maximal violation* seems to be appropriate for any $F \gtrsim 1$.

Figure 34 shows the results with uncertainties calculated from the scatter of the voltage measurements (see section 4.1.2). The uncertainties are propagated assuming Gaussian statistics and independent scatter on ΔE_x and ΔG_x, which is only justified at peak positions, not for the interpolation in between, where this overestimates the uncertainty.

Keeping in mind the limitations of the uncertainty estimate, both F_2 and F_3 stay below unity, indicating that the energy of the site and the links is not completely independent. F_1 shows maximal violation for site 1, which is explained by the fact that it is the only site that is not initialized and runs at much lower amplitude than the other oscillators.

The third charge with $F_3 \approx 0.5$ has the best behavior. From simulations in section 3.5 we have seen a typical violation of one tenth due to the small coupling and rotating wave approximations. Compared to this, the violation of F_3 is still substantial. Some violation is due to the rotating wave approximation and may be discarded by careful averaging, but figure 34 shows that the main contribution to the deviations appears on the longer timescale of the beat. All in all, the circuit observes conserved quantities only partially, possibly posing problems for theoretical approaches requiring close compliance with conservation laws.

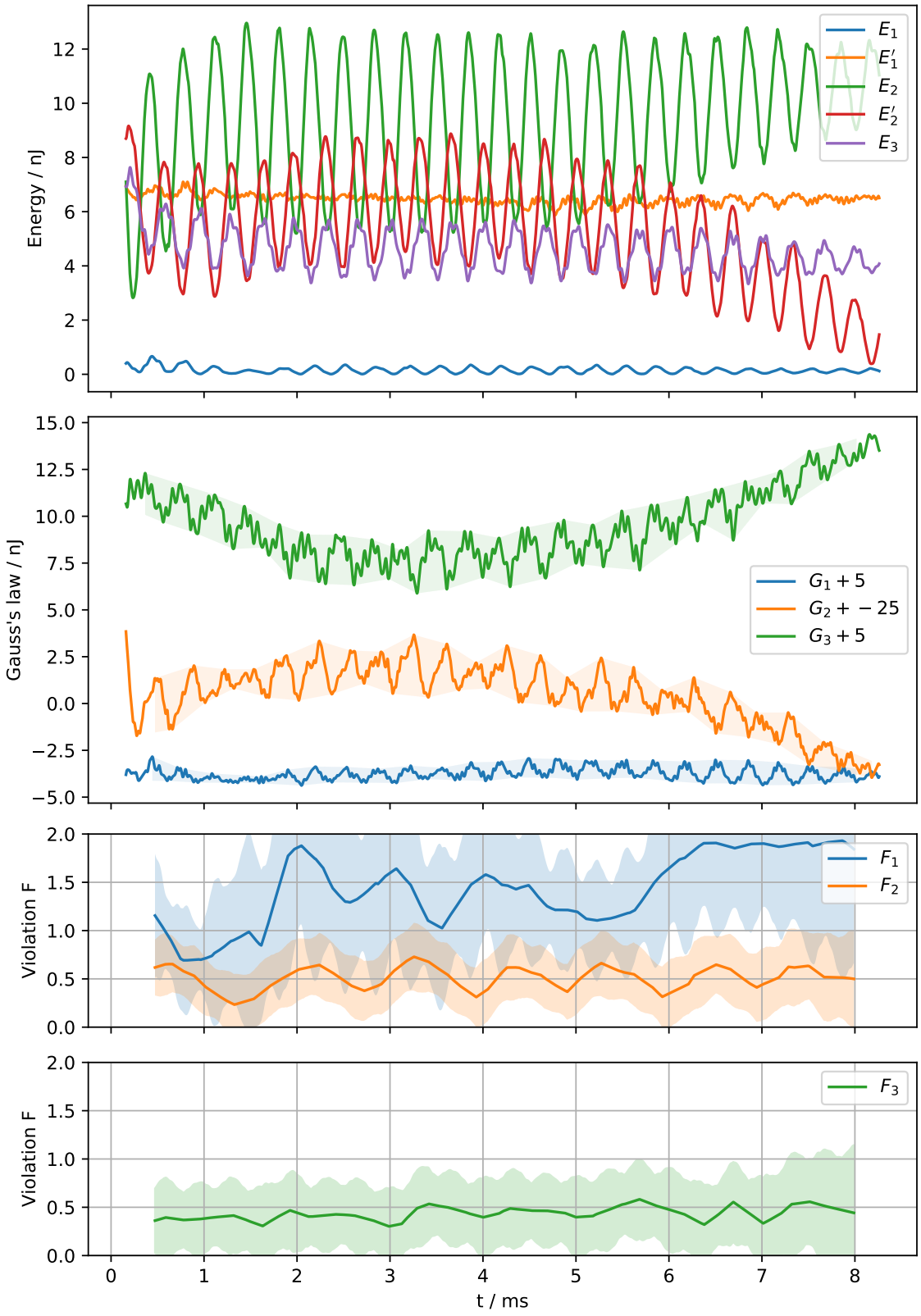

Figure 34: Violation of Gauss's law in measurement set (2) without driving, i. e. $I_{\text{drv}} = 0$. Top: energy of oscillators; middle: charges of Gauss's law with shaded regions indicating ΔG_x; bottom two: violation F_x with shaded regions showing the scatter due to uncertainties in the voltage measurement. $F_x = 0$ means perfect conservation and values larger one indicate strong violation.

5

CONCLUSION

To summarize, we have had a look at the SSH model and with a simple circuit reproduced results from Lee et al. [13]. More importantly, we could learn about how to use circuits for modeling Hamiltonians. By introducing complex variables, the Hamiltonian took on a form recognizable from quantum mechanics. The similar formulation facilitates drawing analogies between calculations for classical or quantum effects.

By introducing a variant of minimal coupling into the SSH model, it becomes a U(1) gauge theory. This U(1) model describes an non-linear system with dynamic gauge variables. The gauge transformation is a local phase transformation that is associated to local conservation laws, which mimic Gauss's law in our case. An electronic circuit was derived that matches the Hamiltonian in the rotating wave approximation and limit of small coupling. While approximate analytical solutions for the full system could not be found in this thesis, numerical simulations provided predictions for the measurements and estimates for the impact of the approximations in the derivation.

A smaller version of the Hamiltonian with external links is formally equivalent to the two-level system of quantum mechanics and its analytical solutions. Though it is linear, it still relies on the interaction term, thereby allowing benchmarks of the corresponding circuit implementation.

The circuit was realized consisting of robust & non-specialized standard electronic components, except for the handmade coils. With the configuration of the two-level system, the behavior of the interaction could be verified: the frequency components of the voltage signal, which correspond to the eigenvalues of the Hamiltonian, match the avoided crossing of the two-level system particularly well. We have developed a measure for the violation of conserved quantities by comparison of their range during time evolution versus the range of the system. It shows that the total number with a violation of roughly 0.5 is halfway between perfect conservation and independence.

The circuit for the full dynamic U(1) model could be implemented with three sites and two links in between. For spectra depending on external driving, only a qualitative comparison to the simulation could be drawn, but a quantitative analysis was done for the local conservation laws. Of the three local charges, one was maximally violated due to a small amplitude of one oscillator. The other two had violations of roughly 0.5 like the total number in the two-level system.

Conserved quantities are commonly used to facilitate theoretical calculations. Violations stem from the approximations in the derivation of the circuit and the imperfect implementation. While the measured spectra look promising, the significant violation of conserved quantities may forbid some theoretical approaches, which rely on strict separation of sectors of different charges. Handling broken gauge invariance in perturbation theory is subject to current research [50]. Imperfect simulators, be they classical or quantum, still allow qualitative statements that are more fault-tolerant, such as the presence or absence of phenomena [2].

The circuit includes oscillator feedback to remedy dissipation. We have seen that this feedback has significant impact on the behavior of the circuit. Only with great care in the tuning of the oscillators, the clean two-level spectrum emerged, because the crude feedback mechanism is linear only for a small operating region. It directly affects the energy stored in the resonators and therefore is important for the conserved quantities. Especially where numerical solutions predict diverging / non-periodic solutions, the feedback forcibly stabilizes the circuit to periodic behavior. For these reasons, improving the feedback mechanism could very well improve the conservation laws of the circuit. On the other hand, the feedback could be incorporated into the theoretical description of the circuit, where—given better control—it might be used, for example, to implement terms like a quadratic number operator causing confinement.

A promising approach for further work on this circuit is to increase the length of the U(1) model such that it develops a bulk with accompanying band structure. Simulations show that the well separated peaks in the spectrum join to smeared out bands for as low as five sites. The classical electronics allow a scaling linear in time and cost with the system size. Since special cases of the U(1) model mimic the SSH model, longer chains could also show joint effects of topology and interactions. If links are driven externally, the U(1) model is simplified back to the SSH model but with 'programmable,' even time dependent, coupling strengths.

Another option for further developments is, as mentioned in the introduction, the step to non-abelian gauge theories. If we want to apply the methods developed in this work, an object is needed that allows the desired group operation. For U(1) it was a complex variable describing one oscillator. The Lie algebra for the non-abelian group SU(2), commonplace as spin in quantum mechanics, is isomorphic to the Lie algebra SO(3) of rotations in three-dimensional space [21]. This makes it plausible that suitable classical objects can be found to build the simulator from.

The circuit developed here potentially allows a rather direct translation to superconducting quantum devices. For example recently a superconducting circuit—based on a design strikingly similar to the circuit schematic of our U(1) model—was realized for simulating molecular vibronic spectra [51].

Simply cooling down our circuit to make quantum effects noticeable is not practicable, because i. a. semiconductor technology does not work as intended when cooled close to absolute zero. This can be solved by replacing parts of the circuit with specialized superconducting devices. While LC resonators appear routinely in superconducting circuits, a suitable alternative also exists for the mixer core: the Josephson mixer [52]. It implements an interaction term coupling three fluxes, which means that the interaction moves to the potential term of the Hamiltonian (our U(1) interaction couples three charges Q, which are momentum variables of the system). This makes the weak coupling approximation needed for our U(1) circuit superfluous. With all basic ingredients already available, the translation to superconducting devices seems natural.

The main purpose of this project was to evaluate the feasibility of classical electronic circuits as fast prototyping platform for gauge theory simulation, especially towards non-abelian gauge theories. In the long run, non-abelian *quantum* simulators are supposed to advance calculations of high energy physics intractable with classical computers [10]. The classical platform developed in this thesis should allow the exploration of questions arising for implementations of non-abelian gauge theories, complementing advances in quantum experiments [5].

BIBLIOGRAPHY

[1] I. M. Georgescu, S. Ashhab, and F. Nori. "Quantum simulation." In: *Reviews of Modern Physics* 86.1 (Mar. 10, 2014), pp. 153–185. DOI: 10.1103/RevModPhys.86.153.

[2] U.-J. Wiese. "Ultracold quantum gases and lattice systems: quantum simulation of lattice gauge theories." In: *Annalen der Physik* 525.10 (2013), pp. 777–796. ISSN: 1521-3889. DOI: 10.1002/andp.201300104.

[3] V. Kasper, F. Hebenstreit, F. Jendrzejewski, M. K. Oberthaler, and J. Berges. "Implementing quantum electrodynamics with ultracold atomic systems." In: *New Journal of Physics* 19.2 (Feb. 2017), p. 023030. ISSN: 1367-2630. DOI: 10.1088/1367-2630/aa54e0.

[4] T. V. Zache, F. Hebenstreit, F. Jendrzejewski, M. K. Oberthaler, J. Berges, and P. Hauke. "Quantum simulation of lattice gauge theories using Wilson fermions." In: *Quantum Science and Technology* 3.3 (June 2018), p. 034010. ISSN: 2058-9565. DOI: 10.1088/2058-9565/aac33b.

[5] A. Mil, T. V. Zache, A. Hegde, A. Xia, R. P. Bhatt, M. K. Oberthaler, P. Hauke, J. Berges, and F. Jendrzejewski. "A scalable realization of local U(1) gauge invariance in cold atomic mixtures." In: *Science* 367.6482 (Mar. 6, 2020), pp. 1128–1130. ISSN: 0036-8075, 1095-9203. DOI: 10.1126/science.aaz5312.

[6] F. Görg, K. Sandholzer, J. Minguzzi, R. Desbuquois, M. Messer, and T. Esslinger. "Realization of density-dependent Peierls phases to engineer quantized gauge fields coupled to ultracold matter." In: *Nature Physics* 15.11 (Nov. 2019), pp. 1161–1167. ISSN: 1745-2481. DOI: 10.1038/s41567-019-0615-4.

[7] C. Schweizer, F. Grusdt, M. Berngruber, L. Barbiero, E. Demler, N. Goldman, I. Bloch, and M. Aidelsburger. "Floquet approach to $\mathbb{Z}_2$ lattice gauge theories with ultracold atoms in optical lattices." In: *Nature Physics* 15.11 (Nov. 2019), pp. 1168–1173. ISSN: 1745-2481. DOI: 10.1038/s41567-019-0649-7.

[8] E. A. Martinez, C. A. Muschik, P. Schindler, D. Nigg, A. Erhard, M. Heyl, P. Hauke, M. Dalmonte, T. Monz, P. Zoller, and R. Blatt. "Real-time dynamics of lattice gauge theories with a few-qubit quantum computer." In: *Nature* 534.7608 (June 2016), pp. 516–519. ISSN: 1476-4687. DOI: 10.1038/nature18318.

[9] C. Kokail, C. Maier, R. van Bijnen, T. Brydges, M. K. Joshi, P. Jurcevic, C. A. Muschik, P. Silvi, R. Blatt, C. F. Roos, and P. Zoller. "Self-verifying variational quantum simulation of lattice models." In: *Nature* 569.7756 (May 2019), pp. 355–360. ISSN: 1476-4687. DOI: 10.1038/s41586-019-1177-4.

[10] V. Kasper, G. Juzeliūnas, M. Lewenstein, F. Jendrzejewski, and E. Zohar. "From the Jaynes–Cummings model to non-abelian gauge theories: a guided tour for the quantum engineer." In: *New Journal of Physics* 22.10 (Oct. 2020), p. 103027. ISSN: 1367-2630. DOI: 10.1088/1367-2630/abb961.

[11] J. Ningyuan, C. Owens, A. Sommer, D. Schuster, and J. Simon. "Time- and Site-Resolved Dynamics in a Topological Circuit." In: *Physical Review X* 5.2 (June 22, 2015), p. 021031. DOI: 10.1103/PhysRevX.5.021031.

[12] S. Imhof, C. Berger, F. Bayer, J. Brehm, L. W. Molenkamp, T. Kiessling, F. Schindler, C. H. Lee, M. Greiter, T. Neupert, and R. Thomale. "Topolectrical-circuit realization of topological corner modes." In: *Nature Physics* 14.9 (Sept. 2018), pp. 925–929. ISSN: 1745-2481. DOI: 10.1038/s41567-018-0246-1.

[13] C. H. Lee, S. Imhof, C. Berger, F. Bayer, J. Brehm, L. W. Molenkamp, T. Kiessling, and R. Thomale. "Topolectrical Circuits." In: *Communications Physics* 1.1 (July 23, 2018), pp. 1–9. ISSN: 2399-3650. DOI: 10.1038/s42005-018-0035-2.

[14] W. P. Su, J. R. Schrieffer, and A. J. Heeger. "Solitons in Polyacetylene." In: *Physical Review Letters* 42.25 (June 18, 1979). Publisher: American Physical Society, pp. 1698–1701. DOI: 10.1103/PhysRevLett.42.1698.

[15] M. Atala, M. Aidelsburger, J. T. Barreiro, D. Abanin, T. Kitagawa, E. Demler, and I. Bloch. "Direct measurement of the Zak phase in topological Bloch bands." In: *Nature Physics* 9.12 (Dec. 2013), pp. 795–800. DOI: 10.1038/nphys2790.

[16] T. Kotwal, H. Ronellenfitsch, F. Moseley, A. Stegmaier, R. Thomale, and J. Dunkel. "Active topolectrical circuits." In: *arXiv:1903.10130* (Aug. 12, 2019). URL: http://arxiv.org/abs/1903.10130.

[17] N. Batra and G. Sheet. "Understanding Basic Concepts of Topological Insulators Through Su-Schrieffer-Heeger (SSH) Model." In: *arXiv: 1906.08435 [cond-mat]* (June 20, 2019). DOI: 10.1007/s12045-020-0995-x. URL: http://arxiv.org/abs/1906.08435 (visited on 2020-07-03).

[18] C. K. Alexander and M. N. O. Sadiku. *Fundamentals of electric circuits*. 5th ed. New York: McGraw-Hill, 2013. ISBN: 978-0-07-338057-5.

[19] U. Vool and M. Devoret. "Introduction to quantum electromagnetic circuits." In: *International Journal of Circuit Theory and Applications* 45.7 (2017), pp. 897–934. ISSN: 1097-007X. DOI: 10.1002/cta.2359.

[20] B. Svistunov. "Complex Variables in Classical Hamiltonian Mechanics." Lecture notes, University of Massachusetts. URL: http://web.physics.ucsb.edu/~fratus/Phys100A/Boris/605_ham_(11).pdf (visited on 2020-10-12).

[21] H. Goldstein, P. Poole, and J. Safko. *Classical Mechanics*. 3rd ed. Addison-Wesley, 2001.

[22] P. A. M. Dirac and R. H. Fowler. "The fundamental equations of quantum mechanics." In: *Proceedings of the Royal Society of London* 109.752 (Dec. 1, 1925), pp. 642–653. DOI: 10.1098/rspa.1925.0150.

[23] J. K. Asbóth, L. Oroszlány, and A. Pályi. *A Short Course on Topological Insulators*. Vol. 919. Lecture Notes in Physics. Cham: Springer International Publishing, 2016. DOI: 10.1007/978-3-319-25607-8.

[24] F. Jendrzejewski, T. Zache, and P. Hauke. *What are dynamical gauge fields? A simplistic introduction by an AMO experimentalist*. Authorea, Inc. DOI: 10.22541/au.150663310.07882650. URL: https://www.authorea.com/users/143341/articles/193740 (visited on 2020-11-05).

[25] N. Goldman, G. Juzeliūnas, P. Öhberg, and I. B. Spielman. "Light-induced gauge fields for ultracold atoms." In: *Reports on Progress in Physics* 77.12 (Nov. 2014), p. 126401. ISSN: 0034-4885. DOI: 10.1088/0034-4885/77/12/126401.

[26] C. Torre. "Scalar Electrodynamics." Lecture Notes. Utah State University. URL: http://www.physics.usu.edu/torre/Classical_Field_Theory/Lectures/05_SED.pdf (visited on 2020-11-05).

[27] D. Tong. "Quantum Field Theory." Lecture notes. University of Cambridge. URL: http://www.physics.usu.edu/torre/Classical_Field_Theory/Lectures/05_SED.pdf (visited on 2020-11-05).

[28] J. C. P. Barros, M. Dalmonte, and A. Trombettoni. "String tension and robustness of confinement properties in the Schwinger-Thirring model." In: *Physical Review D* 100.3 (Aug. 21, 2019), p. 036009. DOI: 10.1103/PhysRevD.100.036009.

[29] C. Schweizer, F. Grusdt, M. Berngruber, L. Barbiero, E. Demler, N. Goldman, I. Bloch, and M. Aidelsburger. "Floquet approach to $\mathbb{Z}_2$ lattice gauge theories with ultracold atoms in optical lattices." In: *Nature Physics* 15.11 (Nov. 2019), pp. 1168–1173. ISSN: 1745-2481. DOI: 10.1038/s41567-019-0649-7.

[30] M. Lutzky. "Conservation laws and discrete symmetries in classical mechanics." In: *Journal of Mathematical Physics* 22.8 (Aug. 1, 1981), pp. 1626–1627. ISSN: 0022-2488. DOI: 10.1063/1.525103.

[31] J. Rammer and D. Pines. *Quantum Transport Theory*. Frontiers in physics. Avalon Publishing, 1998. ISBN: 978-0-7382-0048-4.

[32] P. Sala, T. Shi, S. Kühn, M. C. Bañuls, E. Demler, and J. I. Cirac. "Variational study of U(1) and SU(2) lattice gauge theories with Gaussian states in 1+1 dimensions." In: *Physical Review D* 98.3 (Aug. 27, 2018), p. 034505. DOI: 10.1103/PhysRevD.98.034505.

[33] J. Bender and E. Zohar. "A gauge redundancy-free formulation of compact QED with dynamical matter for quantum and classical computations." In: *arXiv:2008.01349 [hep-lat, physics:quant-ph]* (Aug. 4, 2020). URL: http://arxiv.org/abs/2008.01349.

[34] *Low Cost Analog Multiplier*. AD633. Rev. K. Analog Devices. 2015. URL: https://www.analog.com/media/en/technical-documentation/data-sheets/AD633.pdf (visited on 2020-09-12).

[35] S. Franco. *How to Drive Large Capacitive Loads with an Op-Amp Circuit*. All About Circuits. 2019. URL: https://www.allaboutcircuits.com/technical-articles/how-to-drive-large-capacitive-loads-op-amp-circuit/ (visited on 2020-09-14).

[36] R. Keim. *Negative Feedback Parts 1 – 6*. All About Circuits. 2015. URL: https://www.allaboutcircuits.com/technical-articles/negative-feedback-part-1-general-structure-and-essential-concepts/ (visited on 2020-09-14).

[37] *Activity: Amplifier Output Stages*. Analog Digital. 2019. URL: https://wiki.analog.com/university/courses/electronics/electronics-lab-13a%5C?rev=1566559073 (visited on 2020-09-14).

[38] *An introduction to the air cored coil*. University of Surrey. 2010. URL: http://info.ee.surrey.ac.uk/Workshop/advice/coils/air_coils.html (visited on 2020-04-02).

[39] H. A. Wheeler. "Simple Inductance Formulas for Radio Coils." In: *Proceedings of the Institute of Radio Engineers* 16.10 (1928), pp. 1398–1400.

[40] *WIMA: The Capacitor for High End Audio Applications*. WIMA GmbH & Co. KG. URL: https://www.wima.de/wp-content/uploads/media/WIMA-Audio.pdf (visited on 2020-02-19).

[41] W. Storr. ElectronicsTutorials. 2009. URL: https://www.electronics-tutorials.ws/oscillator/oscillators.html (visited on 2020-09-15).

[42] C. Laboratory. *Electronic Circuits and Tubes*. New York: McGraw-Hill Book Company Inc, 1947, pp. 741–744.

[43] *Complementary Silicon Plastic Power Transistors*. MJE15034,MJE15035. Rev. 6. ON Semiconductor. 2015. URL: https://www.onsemi.com/pub/Collateral/MJE15034-D.PDF (visited on 2020-09-15).

[44] *Feedback | Bipolar Junction Transistors | Electronics Textbook*. All About Circuits. 2020. URL: https://www.allaboutcircuits.com/textbook/semiconductors/chpt-4/feedback/ (visited on 2020-11-15).

[45] *Small Signal MOSFET 500 mA, 60 Volts*. BS170. Rev. 7. ON Semiconductor. 2017. URL: https://www.onsemi.com/pub/Collateral/BS170-D.PDF (visited on 2020-09-12).

[46] *A Comprehensive Study of the Howland Current Pump*. Texas Instruments. 2013. URL: https://www.ti.com/lit/an/snoa474a/snoa474a.pdf (visited on 2020-10-29).

[47] S. Franco. *The Howland Current Pump*. All About Circuits. 2019. URL: https://www.allaboutcircuits.com/technical-articles/the-howland-current-pump/ (visited on 2020-10-29).

[48] *TL07xx Low-Noise JFET-Input Operational Amplifiers*. TL071. Rev. P. Texas Instruments. 2020. URL: https://www.ti.com/lit/ds/symlink/tl072.pdf (visited on 2020-12-01).

[49] B. Yang, H. Sun, R. Ott, H.-Y. Wang, T. V. Zache, J. C. Halimeh, Z.-S. Yuan, P. Hauke, and J.-W. Pan. "Observation of gauge invariance in a 71-site Bose-Hubbard quantum simulator." In: *arXiv:2003.08945* (Aug. 30, 2020). URL: http://arxiv.org/abs/2003.08945.

[50] J. C. Halimeh and P. Hauke. "Reliability of Lattice Gauge Theories." In: *Physical Review Letters* 125.3 (July 15, 2020), p. 030503. DOI: 10.1103/PhysRevLett.125.030503.

[51] C. S. Wang, J. C. Curtis, B. J. Lester, Y. Zhang, Y. Y. Gao, J. Freeze, V. S. Batista, P. H. Vaccaro, I. L. Chuang, L. Frunzio, L. Jiang, S. M. Girvin, and R. J. Schoelkopf. "Efficient Multiphoton Sampling of Molecular Vibronic Spectra on a Superconducting Bosonic Processor." In: *Physical Review X* 10.2 (June 17, 2020), p. 021060. DOI: 10.1103/PhysRevX.10.021060.

[52] J.-D. Pillet, E. Flurin, F. Mallet, and B. Huard. "A compact design for the Josephson mixer: The lumped element circuit." In: *Applied Physics Letters* 106.22 (June 1, 2015), p. 222603. ISSN: 0003-6951. DOI: 10.1063/1.4922188.

[53] M. Moakher. "Means and Averaging in the Group of Rotations." In: *SIAM Journal on Matrix Analysis and Applications* 24.1 (Jan. 2002), pp. 1–16. DOI: 10.1137/S0895479801383877.

A

ALGORITHM DETAILS

A.1 SPECTRUM NORMALIZATION

For the spectrum / discrete Fourier transformation, various normalizations are possible. We choose one with an intuitive meaning close to the common continuous Fourier transformation. A continuous signal $V(t)$ would have the spectrum

$$\tilde{V}(f) = \int_0^T V(t)\, e^{-2\pi i t f} \mathrm{d}t \tag{121}$$

in units of V/Hz. For discrete samples V_n of $V(t)$ at N evenly spaced times with a sample spacing of δt the integral corresponds to

$$\tilde{V}(k) = \delta t \sum_{n=0}^{N-1} V_j\, e^{-2\pi i n k/N}, \quad k = 0 \ldots \left(\left\lfloor \tfrac{N}{2} \right\rfloor + 1\right) \tag{122}$$

where k counts the frequencies $f = k/\delta t$ up to the Nyquist frequency. Negative frequencies are symmetric to their positive counterparts, because all V_n are real. The last sum equals the discrete Fourier transformation implemented by `rfft` of the NumPy library. To attenuate side lobes in the spectrum, a Hamming window function is applied before the discrete Fourier transformation. All spectra plotted in this thesis are computed this way.

A.2 MEAN OF ANGLES

This following considerations are based on ref. [53], esp. section 3.2.2 therein. The arithmetic mean μ of a set of quantities $(\alpha_i)_{i=1\ldots n}$ minimizes the squared distance $d(\cdot,\cdot)$ to all elements in that set:

$$\mu = \min_{\alpha} \sum_{i=1}^{n} d^2(\alpha, \alpha_i). \tag{123}$$

The meaning of this is intuitive and well known in Euclidean spaces with Euclidean distance measure. Angles, however, live in the cyclic unitary group U(1). We use the Riemannian distance, which is the length of the shortest curve on the unit circle connecting the two angles:

$$d(\alpha_1, \alpha_2) = \left|(\alpha_1 - \alpha_2 + \pi) \bmod 2\pi \; - \; \pi\right| \; \in \; [0,\, \pi]. \tag{124}$$

Using $z_i = e^{i\,\alpha_i}$ the sum over all angles can be written in the product $\Pi\, z_i$, and according to ref. [53] the solution to the minimization problem is the argument of one of the roots $(\Pi\, z_i)^{1/n}$. There are n roots and one at the global minimum can be found by explicitly calculating the squared distances for each of them. Note that the result is not necessarily unique, as one can see when considering the mean of the two angles 0° and 180°. In that case, one may take great care in selecting one of them, but for this thesis choosing one arbitrarily is sufficient.

B

PARTS LISTS & FULL SCHEMATIC

B.1 SSH MODEL

Full schematic was already shown on in figure 6 on page 17.

	Component	Manufacturer reference	Details
20×	Inductor $L = 10\,\mu H$	FASTRON 11P-100K-50	$R_{DC} = 35\,m\Omega$, ±10%
10×	Capacitor $C_1 = 100\,nF$	WIMA MKS-2 63 V 0.1 µF	Polyester film, ±5%
11×	Capacitor $C_2 = 220\,nF$	EPCOS B32529 63 V 0.22 µF	Polyester film, ±5%
21×	Single pin headers		
2×	Pinheader jumpers		
	Prototyping board		2.54 mm grid
	Copper wire		Tinned, 0.6 mm

Table 4: Parts list for SSH model.

B.2 U(1) MODEL

Details for all manufactured coils in table 5. Full schematic of one U(1) block in figure 35 with parts listed in table 6.

Code name	Primary windings	Variometer windings	Variocoupler windings	f_{free}/kHz	Q
Janus	250	37	-	31.8	45
Nepenthe	128	42	30	46.9 to 63.3	36 to 53
Mintaka	80.5	18.5	-	88.4	59
Ogat	130	42	25	51.2 to 69.3	36 to 43
Preenos	263	25	-	31.1	60

Table 5: Coils used for U(1) model and two-level system. Winding numbers have errors up to 2%. Measurement incl. uncertainties of f_{free} and Q described in section 4.2 in LC tank circuit with 20 nF.

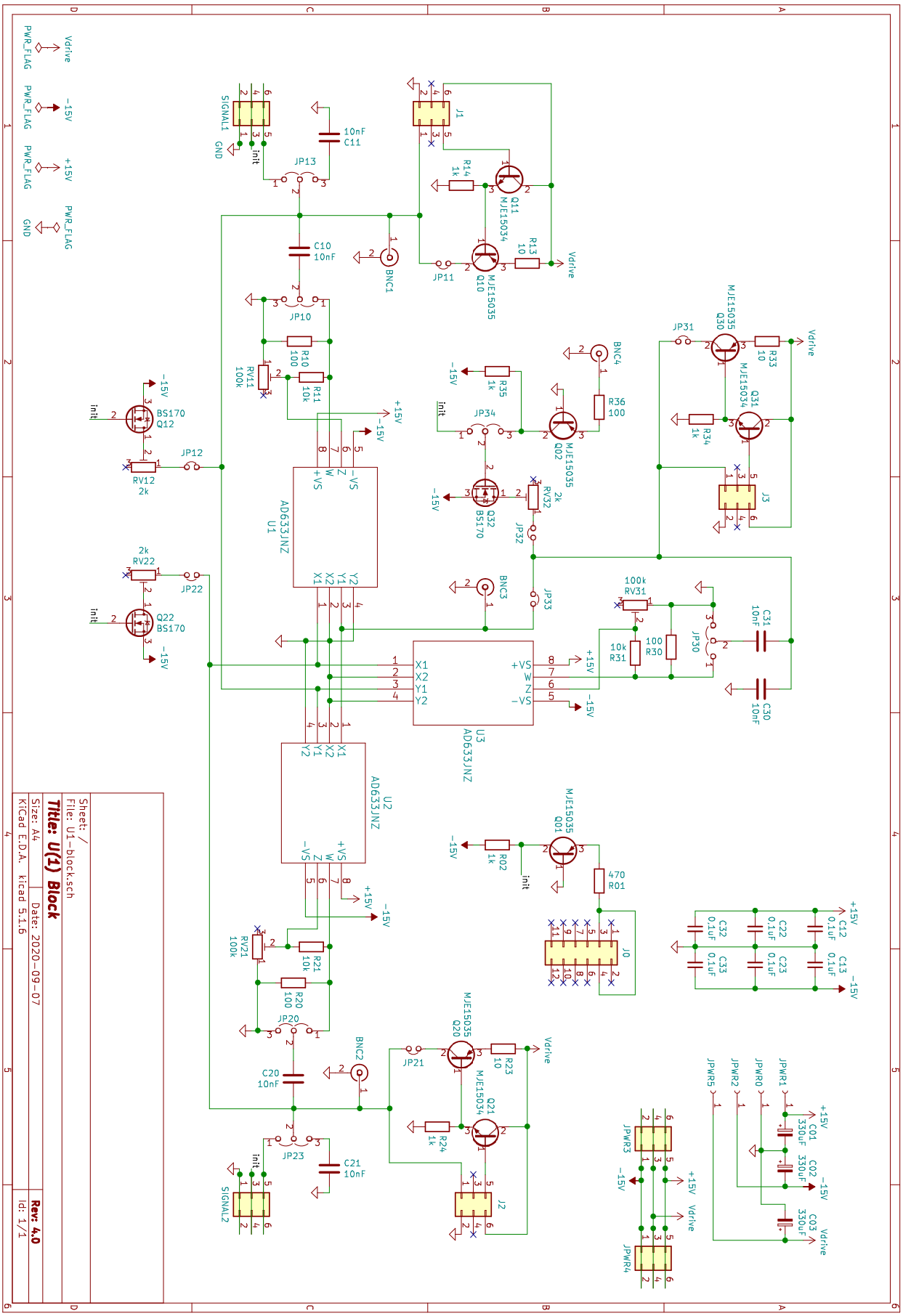

Figure 35: Full schematic of one U(1) block. Contains one muliplier core with link oscillator and two sites.

		Name	Value	Details
3×	Decoupling C	$C_{0?}$	330 µF	Electrolytic
6×	Decoupling C	$C_{?2}$, $C_{?3}$	0.1 µF	Ceramic
6×	Capacitor	$C_{?0}$, $C_{?1}$	10 nF	WIMA FKP2 100 V
3×	BNC connector			Amphenol RF, 50 Ω
	Trigger connector	J_0		2 × 6 pin socket
3×	Coil connector	$J_{1,2,3}$		2 × 3 pin socket
7×	Jumpers	$JP_{?1}$, $JP_{?2}$, JP_{33}		1 × 2 pin header
6×	2-way jumpers	$JP_{?0}$, $JP_{?3}$		1 × 3 pin header
2×	Board connector	$JPWR_3$, $SIGNAL_1$		2 × 3 pin header
2×	Board connector	$JPWR_4$, $SIGNAL_2$		2 × 3 pin socket
4×	Power connector	$JPWR_{0,1,2,5}$		Banana mini jack
5×	PNP power BJT	$Q_{0?}$, $Q_{?0}$	MJE15035	ON Semiconductor
3×	NPN power BJT	$Q_{?1}$	MJE15034	ON Semiconductor
3×	Small signal MOSFET	$Q_{?2}$	BS107	
	Resistor	R_{01}	470 Ω	$\frac{1}{4}$W, metal film, ±1%
5×	Resistor	R_{02}, $R_{?4}$, R_{35}	1 kΩ	$\frac{1}{4}$W, metal film, ±1%
4×	Resistor	$R_{?0}$, R_{36}	100 Ω	$\frac{1}{4}$W, carbon, ±5%
3×	Resistor	$R_{?1}$	10 kΩ	$\frac{1}{4}$W, metal film, ±1%
3×	Resistor	$R_{?3}$	10 Ω	$\frac{1}{4}$W, coal, ±5%
3×	Potentiometer	$RV_{?1}$	100 kΩ	Bourns
3×	Potentiometer	$RV_{?2}$	2 kΩ	Bourns
3×	Analog multiplier	$U_?$	AD633JNZ	Analog Devices
3×	IC socket			
	Circuit board			1.5 mm thick, 2-sided
				35 µm copper
	Copper wire			Tinned, 0.6 mm

Table 6: Parts list for Howland current pump.

B.3 HOWLAND CURRENT PUMP

Full schematic was already shown on in figure 22 on page 49.

		Name	Value	Details
4×	Resistor	$R_{1,2,3,4}$	82 kΩ	$\frac{1}{4}$W, metal film, ±1%
	Resistor	R_5	180 Ω	$\frac{1}{4}$W, metal film, ±1%
	Resistor	R_{sense}	33 Ω	$\frac{1}{4}$W,metal film, ±1%
	Potentiometer	RV_1	2 kΩ	Bourns
	Op amp		`TL071`	Texas Instruments
3×	BNC connector			Amphenol RF, 50 Ω
	Prototyping board			Grid spacing 2.54 mm
	Copper wire			Tinned, 0.6 mm

Table 7: Parts list for Howland current pump.

ACKNOWLEDGMENTS

I would like to thank Fred Jendrzejewski for providing the opportunity of working on this project and the supportive & engaging supervision. I would like to thank Jürgen Berges for being the second examiner of this thesis. Erez Zohar and Robert Ott have contributed with valuable discussions about theory questions and Landry Bretheau with first-hand advice on superconducting quantum devices. Many thanks go to the SynQS group and especially the NaLi and SoPa teams for the good time and splendid food. I am grateful for Jonas and Melanie spending time on proofreading this thesis. Shout-out to my φseekers for sticking together 'til the end!

ERKLÄRUNG

Ich versichere, dass ich diese Arbeit selbstständig verfasst und keine anderen als die angegebenen Quellen und Hilfsmittel benutzt habe.

Heidelberg, den 15. Dezember 2020

Hannes Riechert